# Flow-dependant forecast uncertainty of summer time precipitation

Florian Heinlein
Matrikel-Nr. 4039970

Masterarbeit

eingereicht im Studiengang
Master Meteorologie
der Ludwig-Maximilians Universität München

Dezember 2011

Wintersemester 2010/2011

Betreuer:
Dr. Christian Keil
Prof. Dr. George Craig

**Abstract**

In general, all scales influence the predictability of convective precipitation. However, this influence depends on the meteorological situation. The high resolution convection permitting ensemble prediction system COSMO-DE-EPS of the Deutsche Wetterdienst (DWD) has been used to forecast convective precipitation in the period from May to August 2009. Various verification methods employing radar observations allowed the detection of major sources of uncertainties in the prediction of convective precipitation. Traditional and spatial verification methods identified differences in the performance of precipiation forecasts during different weather regimes. If small-scale processes are responsible for uncertainties, the EPS will be governed by members with the same variation of model physics but different driving global models. If the large-scale flow dominates the forecast precipiation, members with the same lateral boundary conditions will behave similarly. In this case all members will perform superior in comparison to the periods when local processes are important. The time scale of convective adjustment which correlates with the relative spread within different groups of members confirms this separation and shows a flow-dependant forecast uncertainty of convective precipitation.

## Zusammenfassung

Generell beeinflussen alle Skalen die Vorhersagbarkeit konvektiven Niederschlags. Jedoch hängt dieser Einfluss von der meteorologischen Strömungssituation ab. Das hochaufgelöste Ensemble Vorhersage System COSMO-DE-EPS des Deutschen Wetterdienstes (DWD), welches Konvektion explizit behandelt, wurde benutzt um konvektiven Niederschlag in der Periode von Mai bis August 2009 vorherzusagen. Durch den Vergleich mit Radarbeobachtungen konnten verschiedene Verifikationsmethoden, die Hauptunsicherheiten bei der Vorhersage konvektiven Niederschlags erkennen. Durch traditionelle und räumliche Qualitätsmaße wurden Unterschiede in der Güte von Niederschlagsvorhersagen während verschiedener Strömungssituationen identifiziert. Falls kleinskalige Prozesse für Unsicherheiten verantwortlich sind, so zeigen Mitglieder des EPS, die durch die Variation eines gleichen physikalischen Parameters generiert wurden, eine ähliche Vorhersagequalität, während die antreibenden globalen Modelle eine untergeordnete Rolle spielen. Wenn die synoptisch-skalige Strömungssituation den vorhergesagten Niederschlag dominiert, errechnen Mitglieder des EPS mit gleichen seitlichen Randbedingungen ähnliche Niederschlagswerte. In diesem Fall erfüllen alle Mitglieder eine höhere Vorhersagequalität im Vergleich zu Zeitabschnitten in denen nur lokale Prozesse wichtig sind. Die konvektive Zeitskala, die mit dem relativen Spread innerhalb verschiedener Gruppen von Ensemble-Mitgliedern korreliert, bestätigt diese Unterteilung und macht die Bedeutung strömungsabhängiger Vorhersagbarkeit von konvektivem Niederschlag deutlich.

# Contents

# Chapter 1

# Introduction

For thousands of years mankind has been interested in the weather and its prediction. Even the ancient Greeks tried to describe the weather, as ARISTOTLE did in his book *Meteorologica*. He mentioned four main elements (earth, water, air, fire) which are arranged around the earth in different layers but can interact with each other and thus cause weather phenomena. ARISTOTLE's follower, THEOPHRASTUS, took another step forward and tried to relate observations with upcoming weather events, for example shooting stars were a sign of imminent wind and rain for him.

In Germany weather lore, and particularly the "Hundertjährige Kalender" (from the 17th century on) played a big role in helping the farmers to cope with fertile and infertile years even though its usefulness is questionable today (BINDER 2000).

In the 19th century significant progress was made due to the beginning of global observation systems. The Norwegian BJERKNES (1904) was one of the first to think about mathematical forecasting and suggested two steps: a diagnostic step to get initial conditions of the forecast employing observations and subsequent a prognostic step to evolve the initial conditions in time. He formed seven independent equations containing seven basic variables. But neither an analytical solution nor a numerical solution was possible. So he solved the equations graphically.

A next important step was taken by Richardson who had no formal training in weather prediction. He tried to solve the differential equations describing the changes in the atmosphere numerically. But his results were frustrating: he calculated surface pressure changes of about 145hPa in 6h which is unrealistic. His problem was not initialising the data he used. Nowadays a similar model without initialisation run on a computer obtains almost the same unrealistic results as Richardson, but realistic ones if the data was initialised by a digital filter (LYNCH 2008).

In the first half of the 20th century modern numerical weather prediction (NWP) could be developed due to deeper understanding in theoretical meteorology, development of stable algorithms in numerics, the invention of the radiosonde as well as the invention of the digital computer (LYNCH 2008).

At the same time as Eady criticised the deterministic approaches to weather forecasting, these started to succeed at the beginning of the 1950s. Eady argued that small perturbations could exist that are lower than a given limit of error. These perturba-

tions can grow exponentially and therefore result in exponential growth of the limit of error. That is the reason why many evolutions of different initial conditions are to be considered in NWP to finally obtain a probability distribution of answers (LEWIS 2005).

Later, LORENZ (1962) used linear regression to make some predictions. As expected he obtained good results for 1-day forecasts but unsatisfying results for 3- to 4-day forecasts. He furthermore demonstrated that even very small disturbances in the initial conditions of one parameter (lower than the observation error) lead to large error growths and completely different long-time forecasts (six months). Lorenz furthermore developed the notion that rounding of intermediate output from six to three digits produced completely different results than without intermediate rounding. This again favoured the importance of small errors and showed that long-range forecasts were out of the question since observation errors are generally even bigger than those roundings Lorenz did (LEWIS 2005).

Hence, as a result of the fast growth of errors in the initial state as well as the atmosphere's chaotic behaviour and its poor understanding, predictability is limited to a few days. Therefore, ensemble prediction systems (EPS) which use a probabilistic approach were introduced to examine predictability (LYNCH 2008). They became operational at ECMWF (European Centre for Medium-Range Weather Forecasts), NMC (National Meteorological Center, today NCEP: National Centers for Environmental Prediction) and MSC (Meteorological Service of Canada) in the early 1990s. Operational EPS rely on enhancements in data assimilation and in model physics but also on more affordable parallel-processing machines (LEWIS 2005). EPS make a certain number of forecasts while each member of the EPS starts with slightly different initial conditions, boundary conditions and/or variations of physical parameters.

For synoptic scales the usefulness of EPS has already been proven many times (see e.g. LEUTBECHER and PALMER 2008). Already in 1996 MOLTENI et al. achieve good performance of the ECMWF EPS especially in summer and autumn while in winter some cases of poor performance were observed. By contrast, high resolution, i.e. cloud-resolving, models are more difficult to construct. KONG et al. (2006) generated 3 ensemble systems with 5 members each and with grid sizes of 24km, 6km and 3km to forecast a tornadic thunderstorm complex. In general the ensembles show better results than the deterministic forecasts. At the highest resolution of 3km all ensemble members predicted the structure of the storm system and its movement quite well even though convection is only poorly resolved (but nevertheless better than in the larger grid cases).

Another high-resolution ensemble is presented by HOHENEGGER and SCHÄR (2007). They compare the ECMWF EPS with an ensemble of the Lokal-Modell (LM; nowadays COSMO, COnsortium for Small-Scale MOdelling) for small scales. Both EPS show predictable and unpredictable periods of precipitation. In the LM error growth rates are ten times larger than in the ECMWF EPS, but the lead times are ten times shorter which makes the two EPS comparable. But at cloud-resolving scale the tangent linear approximation fails after a very short integration period. Taking this issue into account

a 10-day forecast in synoptic scales corresponds to 7h of cloud-resolving simulation. Therefore, one has to make adaptions while constructing cloud-resolving ensembles.

This points to the relation of time-scale and spatial scales of instabilities in the atmosphere. Instabilities of small-scale phenomena grow much faster than large-scale instabilities. Convection is such a small-scale phenomenon. Cumulus clouds grow with an exponential time-scale of about 10 minutes. So the precipitation of individual thunderstorms is only predictable for less than roughly an hour. But if convection is forced by larger scales, e.g. by fronts, then the convective precipitation can be predicted much longer than precipitation of individual thunderstorms (Kalnay 2003).

An EPS based on the COSMO-DE model in which convection is not parameterised has been developed at the Deutsche Wetterdienst (DWD; German Meteorological Service). 15 days in summer 2007 have been examined by Gebhard et al. (2010) with three different ensemble setups: perturbation of lateral boundary conditions (BC), changing of model physics (PHY) and a combination of both. Precipitation forecasts were verified and the probabilistic forecasts showed better results than the single deterministic forecast. It is expected that this approach leads to an amelioration of quantitative precipitation forecasts (QPF) which is one of the main challenges in NWP. Hopefully improvement can also be rendered by models with higher resolution and, thus, explicit treatment of convection (Ebert 2003)

However, the difficulty of QPF comprises managing the eventual short duration of convective precipitation events and their spatial extension which is sometimes small. The diameter of precipitation features can be around a few kilometers only and are therefore difficult to resolve. Nowadays numerical models are able to predict intensive precipitation events realistically, but they sometimes fail in predicting these events at the right time. Such temporal errors are very important for the verification of QPF and can lead to a misinterpretation of the verification results (Zimmer and Wernli 2011). QPF are especially important for the prediction of severe weather events associated with heavy precipitation like flash floods, ice storms or heavy snowfall. Even though it is challenging, QPF can also be integrated into hydrologic models, for example into flood forecasting operations (Cuo et al. 2011).

All different scales have an impact on forecast uncertainty of convective precipitation but this depends on the meteorological situation. Stensrud et al. (2000) examined two meso-scale short-range EPS: one with perturbations of model physics (PHY) and one created using different initial conditions (IC). In periods where large scale forcing for convection was weak, the PHY EPS had better results, while in periods with strong large scale forcing, the IC EPS was superior to the PHY EPS. Additionally, the variance between the PHY members becomes very high very rapidly compared to the IC members. This result suggests that varying model physics is a powerful method of creating ensembles. The first result of Stensrud et al. was confirmed by Jones et al. (2007) who evaluated a meso-scale short-range EPS over the North East of the USA with 12km of horizontal resolution and 18 members. The members were generated by different initial

conditions or by variations of the model physics. During the warm season (large-scale forcing weak) the PHY members performed better than the IC members when 24-hour precipitation was examined. By contrast, in the cool season, when large-scale forcing was strong, the IC members had a much higher probabilistic skill for precipitation than the PHY members had.

DONE et al. (2006) studied how the mesoscale environment controls convective precipitation and suggested two different regimes to distinguish between the different kinds of convection. When Convective Available Potential Energy (CAPE) is generated by large-scale forcing, the convection is free to act. The convection stabilises the atmosphere and thus balances the destabilisation of the large-scale forcing. In this regime which is called forced-frontal or equilibrium regime, it is possible to predict the location and overall intensity of precipitation areas while the local variations are unpredictable (cp. ARAKAWA and SCHUBERT 1974). By contrast, in the local-forced or non-equilibrium regime CAPE is present even if the large-scale forcing is weak but the convective inhibition energy (CIN) prevents the air from rising unless there are enough triggers to overcome the CIN. Trigger mechanisms are e.g. orographic lifting, warming of certain areas or maxima of moisture. Even though the large-scale situation is known, these phenomena may hardly be predicted due to their small-scales.

DONE et al. (2006) furthermore proposed that it is possible to differentiate between those two regimes using $\tau_c$, the time scale of convective adjustment. This time scale is an estimate for the time until convective heating removes instability (CAPE) and will be presented in detail in chapter 2. If the convective time scale is short (only a few hours), CAPE will be removed immediately. The more CAPE is created, the more convection occurs. This is the case during the equilibrium regime. On the other hand, if the time scale of convective adjustment is long (about half a day or more) convection does not remove CAPE rapidly. Then the large scale-forcing must be weak, so convection is controlled by local factors only. This represents the non-equilibrium or local-forced regime. In a climatological study ZIMMER et al. (2011) showed that more than one half of the summer time convective events belongs to the equilibrium regime.

Recently KEIL and CRAIG (2011) examined regime-dependant forecast uncertainty of convective precipitation. Nine days during the COPS field campaign in summer 2007 (Convective and Orographically induced precipitation Study, WULFMEYER et al. 2008) were analysed using the COSMO-DE-EPS and radar observations (detailed description in section 3). The convective time scale was employed to distinguish between the two meteorological regimes introduced before. In the first days the convective time scale was long, so convection was triggered. In this period the COSMO-DE-EPS was very sensible to changes in the model physics, however the forecast uncertainty was large because of the importance of local processes like orography and boundary layer phenomena. In the second part of the days the time scale of convective adjustment was short, so the synoptic-forcing controlled the precipitation. In this period all members had a similar quality.

This thesis extends the work of Keil and Craig (2011) examining a longer period of about 100 days in summer 2009 and enlarges the study using two different regions and three different statistical quality measures. Basically two questions can be posed:

- Can the time scale of convective adjustment be used to distinguish between forced-frontal and local-forced convection?
- Are these different regimes rather governed by perturbations of the model physics or by lateral boundary conditions of different global models?

The structure of this thesis is the following: Chapter 2 will take a closer at the convective time scale. Chapter 3 will contain several parts describing the COSMO-DE-EPS, the data which was used, the regions examined and the statistical analysis. In chapter 4 the results will be presented, starting with case studies of the forced-frontal and the local-forced regime. Then the results for the entire period will be shown in detail. Afterwards the similarities and differences to the smaller region will be carved out. Chapter 4 will finish with a short sensitivity study of the convective time scale. The conclusions (chapter 5) will tie together all the results.

# Chapter 2

# The time scale of convective adjustment

## 2.1 The convective time scale in general

Done et al. (2006) suggest two environmental regimes: the equilibrium and the non-equilibrium regime. In the equilibrium regime the generation of CAPE is balanced by instantaneous convection. Thus, during this regime CAPE obtains low values. During the non-equilibrium regime CAPE exhibits large values since it is generated without being consumed until some trigger mechanisms force the air to rise. Although a definitive test to identify the different regimes is infeasible, it is useful to have a quantitative measure to distinguish between them: the timescale of convective adjustment ($\tau_c$). It is an estimate for the rate at which CAPE, i.e. instability, is removed by convective heating.

Emanuel (1994) explains $CAPE_i$ as the total amount of potential energy of a parcel lifted along the parcel trajectory from level i to the level of neutral buoyancy (LNB). This is the level at which the parcel stops rising. If only the vertical component of the lifting force is considered, the potential energy (PE) of a lifted parcel can be expressed by the following equation:

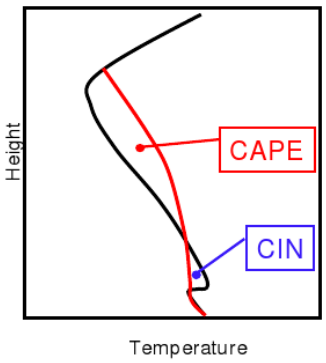


**Figure 1:** Schematic height profile of parcel (red line) and environmental (black line) temperature. CAPE and CIN are defined by the area between the two curves.

$$PE_i = \int_i^{LNB} B\,dz = g \int_i^{LNB} \frac{T_v^p - T_v^e}{T_v^e} dz \tag{1}$$

where B stands for the buoyancy, and z for a unit vector in the vertical direction. $T_v = T(1 + \alpha q_v)$ are the virtual temperatures of the parcel (superscript p) and of the environment (superscript e), g is the acceleration due to gravity. $q_v$ is the specific humidity and $\alpha = \frac{R_v - R_d}{R_d} \approx 0.608$. $R_v$ and $R_d$ denote the gas constants of water and dry air. The ascent of the parcel in the COSMO-DE-EPS is calculated dry adiabatically if the parcel is unsaturated and pseudo-adiabatically if the parcel is saturated.

PE usually consists of a negative (CIN) and a positive (CAPE) part:

$$PE_i = CAPE_i - CIN_i = g \int_{LFC}^{LNB} \frac{T_v^p - T_v^e}{T_v^e} dz + g \int_i^{LFC} \frac{T_v^p - T_v^e}{T_v^e} dz. \tag{2}$$

A schematic illustration of both parameters is displayed in Figure 1. The LFC denotes the level of free convection. At this level a lifted parcel gets positively buoyant, i.e. the parcel rises but does no longer need to be forced. CIN describes this energy which forces the parcel to rise up to the LFC (LEUENBERGER et al. 2010).

The time scale of convective adjustment used in this thesis was defined by DONE et al. (2006) as:

$$\tau_c \sim \frac{\overline{CAPE}}{\frac{\partial}{\partial t}\overline{CAPE}} \tag{3}$$

where $\overline{CAPE}$ is the mean layer-CAPE from the COSMO-DE-EPS (as from now called CAPE). The simulated air parcel starts rising with the mean temperature and humidity of a shallow surface layer, the lowest 50hPa of the atmosphere. This leads to robust calculations as the dependency on the exact structure of the modelled surface layer, which might not be representative for the real atmosphere, will be avoided. For each grid point only one ascent has to be calculated (LEUENBERGER et al. 2010).

As a next step the temporal derivative of CAPE has to be evaluated. CAPE will be removed if there is enough latent heat available through the column to adjust the environmental temperature T with the temperature of a parcel from the surface mixed layer which is pseudo-adibatically lifted. The precipitation rate $\overline{P}^*$ determines the latent heat release:

$$L_v\,\overline{P}^* = \iint \rho\, c_p \frac{dT}{dt} dz\, dA = \frac{\rho\, c_p\, T_0}{g} \frac{\partial}{\partial t} \overline{CAPE} \tag{4}$$

where $L_v$ is the latent heat of vaporisation, $\rho$ is the density of air and $c_p$ is the specific heat of air at constant pressure. A simple manipulation renders the rate of change of CAPE to:

$$\frac{\partial}{\partial t}\overline{CAPE} = \frac{L_v\, g}{\rho\, c_p\, T_0}\overline{P}^* = a\,\overline{P}^* \tag{5}$$

where all the values involved in the term a are assumed as constants. These constants are placed into the following equation in order of appearance:

$$a = \frac{L_v\, g}{\rho\, c_p\, T_0} = \frac{2.5 \cdot 10^6 \frac{J}{kg}\ 9.8\frac{m}{s^2}}{1.2\frac{kg}{m^3}\ 1005\frac{J}{kg\,K}\ 280K} = 72.55\frac{m^4}{kg\,s^2} \tag{6}$$

While equation (5) requires the unit of the precipitation rate $\overline{P}^*$ to be $\frac{kg}{s\,m^2}$, the unit of the input precipitation rate $\overline{P}$ in this study is $\frac{mm}{h}$. Therefore, it is necessary to express the rate $\overline{P}^*$ in terms of $\overline{P}$:

$$\overline{P}^* = \frac{\overline{P}\frac{mm}{h}\ 1000\frac{kg}{m^3}}{1000\frac{mm}{m}\ 3600\frac{s}{h}} = \overline{P}\,(2.78 \cdot 10^{-4}\frac{kg\,hr}{m^2\,mm\,s}) \tag{7}$$

Using equations (5), (6) and (7) $\tau_c$ can be calculated:

$$\tau_c = \frac{1}{2}\frac{\overline{CAPE}}{\overline{P}}\frac{1}{72.55\frac{m^4}{kg\,s^2}\ 2.78 \cdot 10^{-4}\frac{kg\,hr}{m^2\,mm\,s}} = \frac{1}{2}\frac{\overline{CAPE}}{\overline{P}} \cdot 49.58\frac{mm\,s^3}{m^2\,hr} \tag{8}$$

with units:

$$[\tau_c] = \frac{\frac{J}{kg}}{\frac{mm}{h}}\frac{mm\,s^3}{m^2\,hr} = \frac{J\,hr\,mm\,s^3}{kg\,mm\,m^2\,hr} = \frac{s^3\,J}{m^2\,kg} = \frac{s^3\,N\,m}{m^2\,kg} = \frac{s^3\,m}{m\,s^2} = s \tag{9}$$

The scaling factor of $\frac{1}{2}$ in equation (8) is noticeable. This factor results from the pseudo-adiabatic CAPE calculation utilised here. The calculation ignores water loading, entrainment and feedbacks on the layer below the clouds by convective downdrafts. Hence, the convective time scale would be overestimated not introducing this scaling factor (Keil and Craig 2011).

The convective time scale $\tau_c$ has been used to distinguish between the equilibrium and the non-equilibrium regime. Thus, a threshold value of $\tau_c$ has to be defined. According to Done (2006) a typical synoptic time scale would be around a day. But over land the diurnal cycle causes changes in forcing. Therefore, a shorter threshold value of six hours for the distinction between the two regimes is employed in this study. This threshold of six hours has already been used before by Molini et al. (2011) and Keil and Craig (2011). A lower value of $\tau_c$ than this threshold suggests forced-frontal convection. $\tau_c$ exhibiting a higher value than six hours is an indication for local-forced convection.

The calculation of $\tau_c$ and the employment of a threshold value cannot guarantee the correct distinction in all the cases. Low values of CAPE and precipitation rate or high values of both quantities could result in the same values of $\tau_c$. However it is questionable if this would occur in many cases: according to ZIMMER et al. (2011) $\tau_c$ correlates with the precipitation rate and with CAPE, but the precipitation rate and CAPE do not correlate with each other.

The classification with a threshold value of six hours is arbitrary within certain limits: a threshold of three hours for $\tau_c$ would classify 48.5% of the warm-season precipitation events to be in the equilibrium regime whereas 62.5% of the precipitation events would be in equilibrium if a threshold value of twelve hours was employed (see Table 1, ZIMMER et al. 2011). This suggests a well-defined classification of most of the precipitation events for any threshold between three and twelve hours.

## 2.2 Implementation using COSMO-DE data

The convective timescale represents a meteorological environment in which convection occurs, and is highly variable in space and time. Therefore, precipitation and CAPE (TOT_PREC and CAPE_ML 2D surface field from the COSMO-DE-EPS output) are smoothed by a Gaussian kernel before $\tau_c$ is calculated:

$$ke = \frac{1}{\sigma\sqrt{2\pi}} e^{-\frac{x^2}{2\sigma^2}} \tag{10}$$

The values of 61 grid points, i.e. 30 in each direction, contribute to the smoothed values. The standard deviation $\sigma$ equals $\frac{61}{3}$.

Since $\tau_c \sim \frac{\overline{CAPE}}{\overline{P}}$ there is a singularity if $\overline{P}$ approaches zero. Therefore, a threshold value for $\overline{P}$ is introduced: the time scale of convective adjustment is generally only computed on grid points with a precipitation rate of $0.001 \frac{mm}{h}$ or higher.

The calculation of the area-averaged convective time scale takes only grid points into account at which the total precipitation exceeds $1 \frac{mm}{h}$. A threshold of 0.1 $\frac{mm}{h}$ for the area-averaged calculation was also tried. A comparison of the different threshold values of $\overline{P}$ will be presented in section 4.4.2.

# Chapter 3

# Data and methods

## 3.1 Data sources

### 3.1.1 The COSMO-DE-EPS

Model output from the COSMO-DE-EPS is employed in this study. It is an EPS based on the COSMO-DE model (Baldauf et al. 2010, 2011), which is operational at DWD since April 2007. Its model area covers Germany and the Alpine states (Austria and Switzerland) but also includes some parts of the other neighbouring states (see Figure 2).

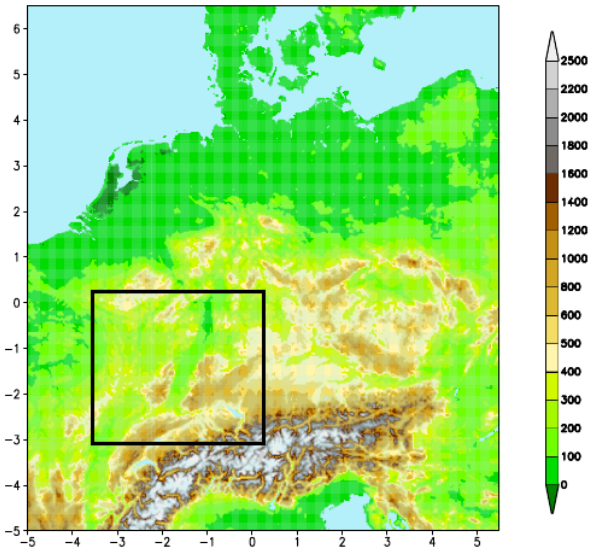


**Figure 2:** Integration area of the COSMO-DE and COPS domain (black bold line) including topographic heights.

The COSMO-DE with its horizontal resolution of 2.8km was designed to achieve a better forecast quality of severe weather conditions due to deep moist convection (e.g. supercell or multicell thunderstorms, shelf clouds or roll clouds) and due to interaction with small-scale topography (e.g. ground fog, Föhn winds or flash floods). In the vertical, the model consists of 50 layers from the ground up to approximately 30hPa.

Because of the high horizontal resolution deep convection is explicitly resolved. However, shallow convection is a subscale process and must be parameterised. But the parameterisation does not contribute to the formation of precipitation. A simple stationary cloud model is used to calculate the vertical redistribution of heat and moisture.

The treatment of precipitation is based on a broad classification of water into its different forms of appearance in the atmosphere. At the moment this principle considers the specific water contents of water vapour, cloud water, cloud ice, rain water, snow and

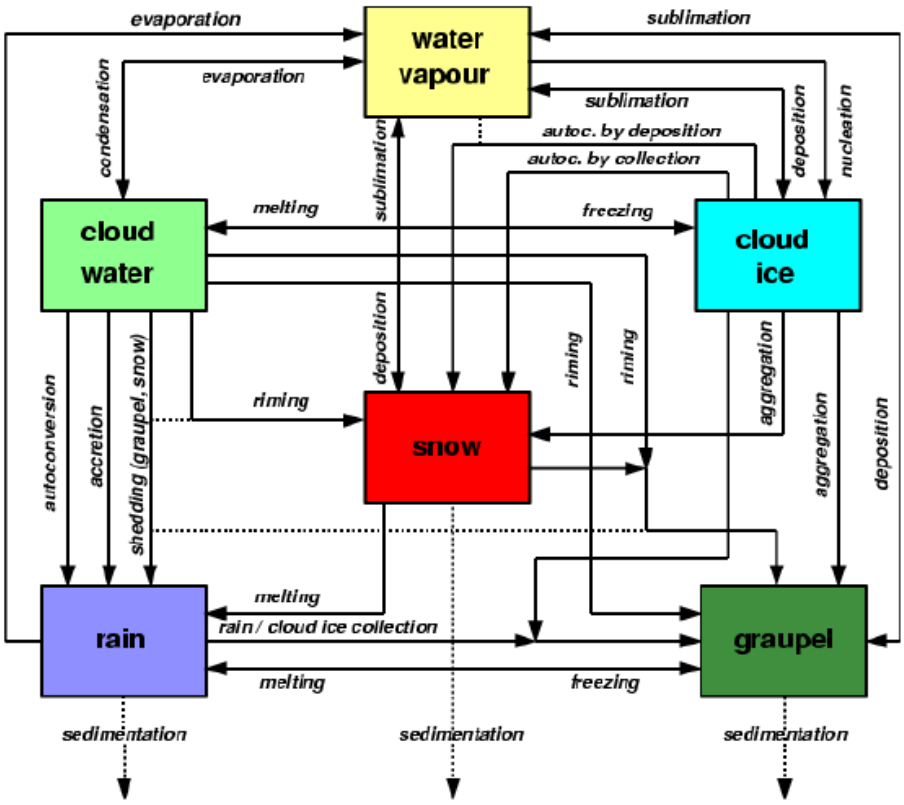


**Figure 3:** Scheme of the microphysical processes in the COSMO-DE, which form clouds and precipitation (BALDAUF 2010).

graupel as prognostic model variables. The particles in these different categories interact in many different ways. The balance equations of these variables describe advective and turbulent transport as well as many processes which characterise the formation of clouds and precipitation. In Figure 3 a schematic diagram of the microphysical processes considered is shown.

To provide suitable initial conditions for the high-resolution model, an assimilation of high-resolution data is required. Currently high-resolution data of the DWD-radar network provides quality-tested radar observations with a horizontal resolution of 1km×1km and a temporal resolution of 5min. This data is interpolated to the COSMO-DE grid and assimilated via Latent Heat Nudging. This is a special nudging technique which determines temperature increments from the ratio between observed and modelled precipitation as well as from the latent heat of the model. By changing the temperature the specific moisture is modified whereas the relative moisture remains constant. These increments influence the dynamics of the model to adjust the model precipitation with the observation (Stephan et al. 2008).

The COSMO-DE uses finite differences to display the spatial differential operators. Most of the prognostic variables are defined on the grid points. The velocity components and the turbulent kinetic energy constitute an exception since they are defined in the middle of the respective cross-section area. This so-called Arakawa-C/Lorenz-grid is employed because it allows a more accurate calculation of the differential quotients. The temporal integration uses a constant timestep $\Delta$t. The COSMO-DE applies the Runge-Kutta-method operationally. In combination with fifth-order horizontal advection this method is very stable and allows a timestep of $\Delta t = 30s$ which is in use at present.

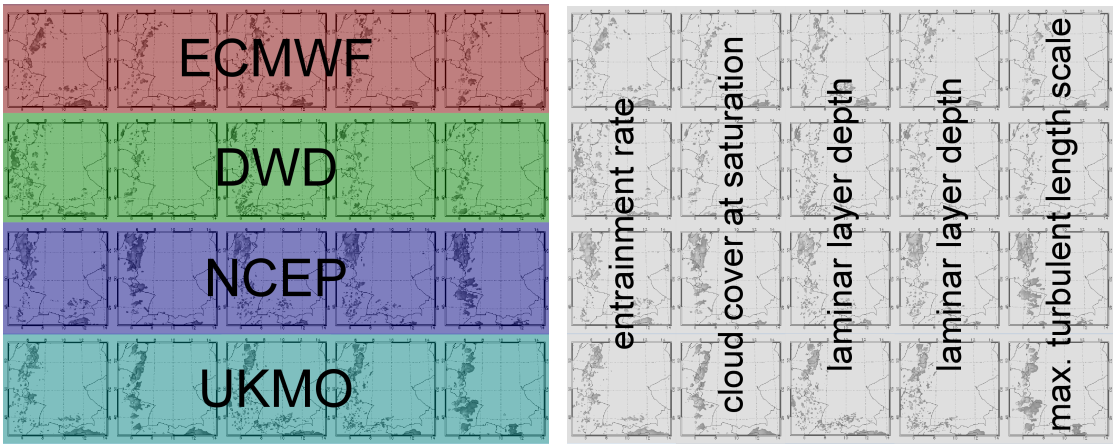


**(a)** Different lateral boundary conditions **(b)** Different model physics

**Figure 4:** Illustration of the COSMO-DE-EPS composition.

| parameter | description | perturbed | default |
|---|---|---|---|
| entr | entrainment rate of shallow convection | 0.002 | 0.0003 |
| ccs | subscale cloud cover given grid-scale saturation in the turbulence scheme | 4 | 0.75 |
| lld01 | scaling factor of the laminar sublayers for scalars | 0.1 | 1.0 |
| lld10 | scaling factor of the laminar sublayers for scalars | 10 | 1.0 |
| turl | asymptotic mixing length of turbulence scheme | 500 | 150 |

**Table 1:** List of perturbed parameters to construct the COSMO-DE-EPS in 2009. The first column displays colours and abbreviations used in the following scatter plots for the averages over the referring groups.

The COSMO-DE-EPS delivers 24-hour-forecasts with hourly model output and is started at 00 UTC from the operational COSMO-DE analysis in that LHN is "on". A 20-members EPS is pre-operational at DWD since December 2010. The COSMO-DE-EPS is to become operational in 2012, after an upgrade to 40 members adding initial condition perturbations (PERALTA and BUCHHOLD 2011). The EPS used in this study consists of 20 ensemble members. They are constructed through combinations of lateral boundary conditions from four different global models with five different perturbations of physical parameters. The lateral boundary conditions stem from nesting the COSMO-DE-EPS into the COSMO-SREPS (Short-Range Ensemble Prediction System). The COSMO-SREPS with its horizontal resolution of 10km is itself a nested EPS driven by four global models. Thus, large-scale uncertainty is transferred down to the convective scale (PAULAT et al. 2009). The lateral boundary conditions of the COSMO-DE-EPS stem from the following global models (MARSIGLI et al. 2008):

- Integrated Forecast System (IFS) of ECMWF (members 1-5)
- Global-Modell (GME) of DWD (members 6-10)
- Global Forecast System (GFS) of NCEP (members 11-15)
- Unified Model (UM) of UKMO (United Kingdom Met Office; members 16-20)

The abbreviations which are used for the different boundary conditions and the referring colours used in some time series are illustrated in Figure 4a.

The perturbations of the model physics which are chosen to achieve a maximum variability of convective precipitation can be seen in Figure 4b. For each perturbation just one physical parameter is varied. The perturbed and the default values of the different parameters are displayed in Table 1. The entrainment rate is responsible for the lateral transport across cloud boundaries through turbulent exchange of mass. It has an impact on the moisture in the boundary layer. The subscale cloud cover affects the vertical

transport via production of turbulent kinetic energy and probably changes the triggering of convection. The scaling factor of the laminar sublayers influences the coupling of the atmosphere with the ground and hence controls the surface fluxes of moisture and temperature. Dissipation, vertical transport, vertical gradients and the stability of the atmosphere are governed by the asymptotic mixing length of the turbulence scheme (Keil and Craig 2011).

### 3.1.2 Radar observations

Instantaneous radar observations from the European Radar Composite are used to validate the model output. These observations which cover an area of 1800km x 1800km over Europe are made available by DWD. The horizontal grid size of the provided radar observations is 2km x 2km (Keil and Craig 2011). The instantaneous radar data uses six reflectivity classes: 7, 19, 28, 37, 46 and 55 dBZ. The treshold for the calculation of the verification scores in this study is 19 dBZ. This corresponds to a rain rate of 1 $\frac{mm}{h}$ (Hagen 2000, 2010), which is the threshold value used in the calculation of the area-averaged convective time scale.

## 3.2 Data availability

The DE region and the COPS region which are analysed in this study are illustrated in Figure 2. The COPS region is especially interesting due to its orography: the Vosges mountains (highest peak 1424m) in northeastern France and the Blackforest (highest peak 1493m) in southwestern Germany. The Upper Rhine Rift with a geographic height that is lower than 200m separates those low mountain ranges. It is known as Germany's warmest area. Due to its orography and its high temperatures local-forced convection is likely to occur in the COPS region.

The bars in Figure 5 show how many ensemble members are available on each day. The model data is not available for all days, so this study cannot be a complete analysis of the summer 2009. However, the dataset is quite large. First the total precipitation was averaged over all grid points. Therefore, the values of the total precipitation are rather small. Due to the smaller number of grid points in the COPS region, these values are sometimes even higher in this region than in the whole model area.

An average of all available ensemble members was computed. Following this step the daily sum of precipitation was calculated. Hence, one can get a rough idea of which days could be forced-frontal (much rain) and which days not. The convective time scale is displayed through daily maxima. Here again, at all given points in time an average of all ensemble members was calculated. Then its maximum values were selected.

In both regions the contrary behaviour of $\tau_c$ and $\overline{P}$ is noticeable: Most of the days exhibiting high precipitation sums are characterised by low values of the convective timescale and vice versa. The percentage of days and points in time, where $\tau_c$ is lower than a certain threshold value, is shown in Table 2. The threshold of 6h which is employed in this study to differentiate between the equilibrium and the non-equilibrium regime assigns around 70% (daily averaged) and 77% (hourly) of the precipitation events to the equilibrium regime. The other threshold values of 3h and 12h assign up to 68% and 85%, respectively, to the forced-frontal regime. The lower the threshold of $\tau_c$ the larger the difference between the two regions. If the daily-averaged $\tau_c$ is taken into consideration, the percentage of forced-frontal precipitation decreases: if the largest part of a day is characterised by low values of $\tau_c$, but a few of the hourly values are high, a high daily-averaged value of $\tau_c$ can be obtained.

| | DE region | | | COPS region | | |
|---|---|---|---|---|---|---|
| | $< 3$h | $< 6$h | $< 12$h | $< 3$h | $< 6$h | $< 12$h |
| daily averaged [%] | 52.9 | 67.8 | 79.3 | 48.3 | 70.1 | 80.5 |
| hourly [%] | 64.9 | 77.2 | 85.2 | 67.8 | 77.2 | 85.1 |

**Table 2:** Percentage, where $\tau_c$ is below a certain threshold value (daily-averaged and for every given point in time), for different threshold values of $\tau_c$ and for the two analysed regions.

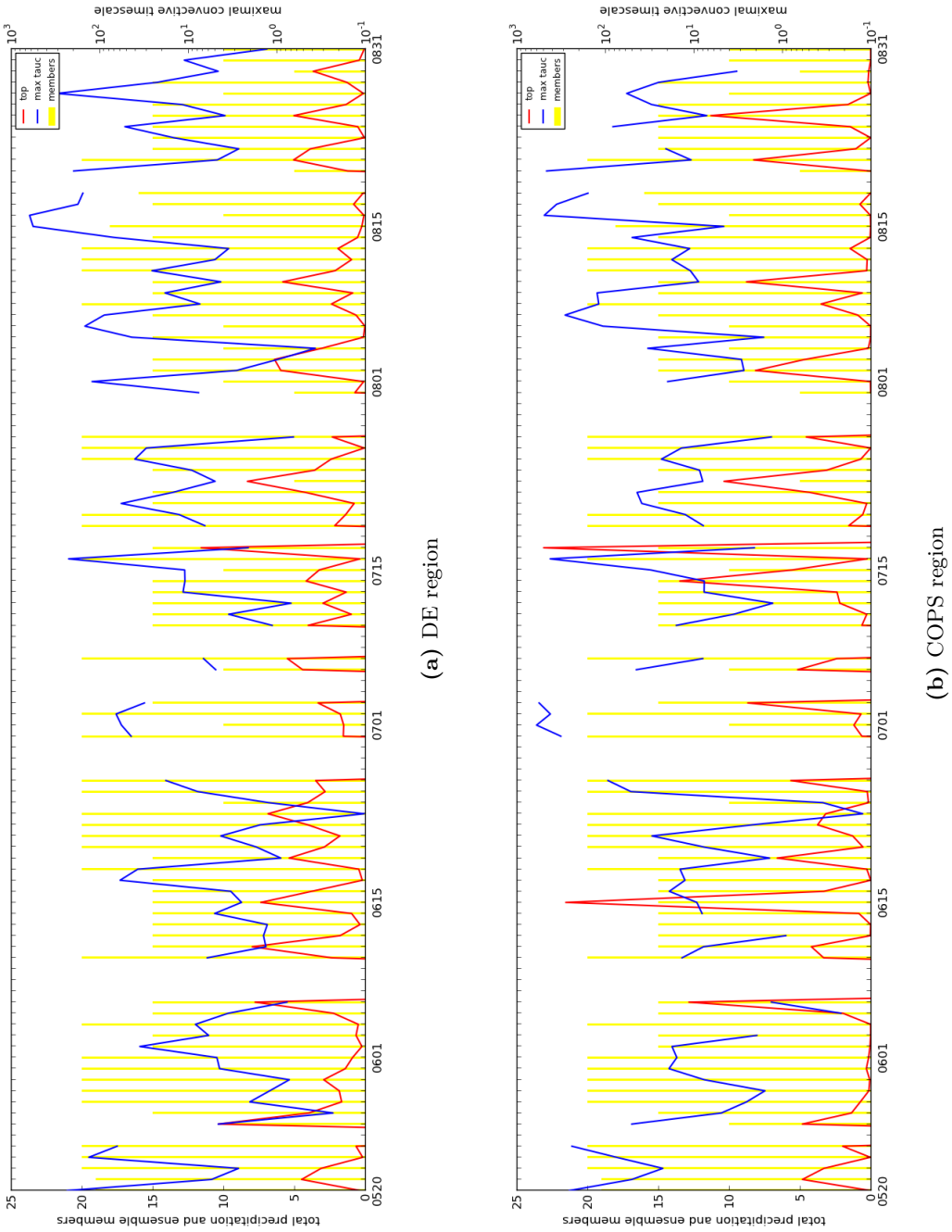


**(a)** DE region

**(b)** COPS region

**Figure 5:** Number of available ensemble members (yellow bars), member-averaged daily precipitation sum (red line) and daily maximum of the convective time scale (blue line).

## 3.3 Verification scores, spread and statistics

### 3.3.1 Traditional verification scores

The conventional scores frequency bias (FBI) and equitable threat score (ETS) have been used to evaluate the skill of the model predictions (cp. WILKS 2005). These scores are calculated with the help of grid point-based contingency tables. A scheme of such a table is shown in Table 3. A hit is an event forecast occuring, which was observed at the time. A miss is an event forecast not occuring, but the event was observed. A false alarm is an event forecast occuring, but which could not be observed. A correct negative is an event forecast occuring, which was also not observed. A perfect forecast system would only consist of hits and correct negatives.

| | | Observed | | |
|---|---|---|---|---|
| | | yes | no | Total |
| Forecast | yes | hits | false alarms | forecast yes |
| | no | misses | correct negatives | forecast no |
| | Total | observed yes | observed no | total |

**Table 3:** Scheme of a contingency table

Then the frequency bias can be calculated:

$$FBI = \frac{hits + false\ alarms}{hits + misses} \tag{11}$$

The FBI ranges from 0 to $\infty$ with a perfect value of 1. This would imply no false alarms and no misses, only hits. The FBI describes the relation of forecast yes events to observed yes events while the correct negatives are ignored. FBI smaller than 1 means that the system has a tendency to underforecast events. If the FBI is higher than 1, the system tends to overforecast precipitation events.

The calculation of the ETS uses all the values from the contingency table:

$$ETS = \frac{hits - hits_{random}}{hits + misses + false\ alarms - hits_{random}} \tag{12}$$

where

$$hits_{random} = \frac{(hits + misses)(hits + false\ alarms)}{total} \tag{13}$$

The ETS ranges between -$\frac{1}{3}$ and 1 as a perfect score, which again implies no misses and no false alarms. A value of 0 means no skill. The ETS measures the fraction of correctly predicted observed and forecast events, as does the FBI. But an adjustment

linked with random chance is additionally considered. Due to its "equitability" the ETS is often used to verify rainfall in NWP models as it allows a better comparison of the scores during different regimes. But the ETS does not distinguish between the source of forecast error because misses and false alarms are treated similarly.

### 3.3.2 The displacement and amplitude score

The displacement and amplitude score (DAS, Keil and Craig 2007, 2009) is a newly developed score applying an optical flow technique which produces a vector field to morph and/or to deform one image to match another image. This is an advantage especially for the verification of QPF from high-resolution models. A precipitation feature which is correct in intensity, size and timing, but on a wrong location would result in very poor traditional error scores due to many false alarms and misses ("double penalty problem"). However, such a forecast would achieve some skill if "eyeball-verified" by a forecaster. In this work precipitation from the model output is displayed on a map. This map is morphed and/or deformed to match another map on which the radar observation is shown and vice versa. The magnitude of the morphing vectors describes the displacement error. The remaining amplitude error is calculated using the differences between the two images after morphing.

In observation space a possible question would be how well a feature is forecast taking the amplitude and the location into consideration. So the image matching algorithm tries to morph the forecast field onto the observation by constructing two fields: the amplitude error field $AMP_{obs}(x, y)$ which is the root-mean-square (RMS) difference between the morphed forecast field and the observation field, and the displacement error field $DIS_{obs}(x, y)$ which is equal to the magnitude of the displacing vector. If there is no feature present in observation space, both fields are set to zero. A zero value of $DIS_{obs}(x, y)$ means either a perfect location forecast or that no other feature was found in the forecast field within the maximum search distance. The second case which can be described as a miss in a contingency table would be balanced by a large amplitude error. $DIS_{obs}(x, y)$ is not equal to zero if a forecast feature was found within the maximum search distance, but on a wrong location.

The same question as above could be asked for the forecast space: how well does it match the location and amplitude of the observation? In this case the observation field is morphed onto the forecast field. A zero displacement error $DIS_{fct}(x, y)$ and a large amplitude error $AMP_{fct}(x, y)$ can be compared to a false alarm, i.e. something was forecast which could not be found within the maximum search distance.

The scalar amplitude score in observation space is defined as the RMS average of the amplitude errors over the verification domain:

$$\overline{AMP_{obs}} = \frac{1}{n_{obs}} \left[ \sum_{A} AMP_{obs}(x, y)^2 \right]^{\frac{1}{2}}, \tag{14}$$

where $n_{obs}$ is the number of nonzero points in the observation field. Similarly an amplitude error $\overline{AMP_{fct}}$ can be defined in the forecast space which uses $n_{fct}$ instead of $n_{obs}$.

In observation space the mean displacement error is

$$\overline{DIS_{obs}} = \frac{1}{n_{obs}} \sum_{A} DIS_{obs}(x, y), \tag{15}$$

while the mean displacement error in the forecast space $\overline{DIS_{fct}}$ is defined in the same manner. All these averages are normalised with $n_{obs}$ and $n_{fct}$ respectively. This makes the values non-sensitive to the area where no events take place and to the size of the analysed domain. Weighted averages are used to define the total amplitude error

$$AMP = \frac{1}{n_{obs} + n_{fct}} (n_{obs}\overline{AMP_{obs}} + n_{fct}\overline{AMP_{fct}}) \tag{16}$$

and the total displacement error

$$DIS = \frac{1}{n_{obs} + n_{fct}} (n_{obs}\overline{DIS_{obs}} + n_{fct}\overline{DIS_{fct}}). \tag{17}$$

But most of the times it is not sufficient to analyse displacement and amplitude error separately. Therefore, the displacement and amplitude error is defined as:

$$DAS = \frac{DIS}{D_{max}} + \frac{AMP}{I_0} \tag{18}$$

Before the two scores are combined, they are normalised. $D_{max}$ is the maximum search distance which normalises the displacement error field. $I_0$ is a typical amplitude of the observed features to normalise the amplitude error field. For small datasets the characteristic intensity $I_0$ is the RMS amplitude of the observed field. For large datasets $I_0$ can be a value from climatology, e.g. a climatological rain rate. This normalisation is designed in such a way that a forecast feature which is displaced with the maximum search distance $D_{max}$ obtains the same error as a miss and a false alarm.

The DAS is negatively orientated and ranges between 0 as best value and theoretically $\infty$. Typical values lie between 0.3 and 1.2. 1 exactly would be obtained if there was a forecast with a correct amplitude and an average displacement error of $D_{max}$ or if there was a forecast at the correct position with an amplitude error of $I_0$, or like in most of the real cases if there was a combination of both errors.

### 3.3.3 Spread and correlations

Precipitation and CAPE from the model output were Gaussian averaged and then averaged over all grid points. These values of precipitation, CAPE and the time scale of convective adjustment were averaged over all available members and the respective standard deviations were calculated. The averaging and the calculation of the standard deviation were also rendered employing the different groups illustrated in Figure 4. The precipitation P will serve as an example for these calculations:

$$\overline{P(t)} = \frac{1}{N_{mem}} \sum_{mem} P_{mem}(t) \tag{19}$$

while $N_{mem}$ denotes the number of available members, mem denotes a certain member and t a certain point in time. The summation takes place across all available members. This is also valid for the estimation of the standard deviation with the sample standard deviation (the dependendy on the point in time is no longer displayed):

$$s_P = \sqrt{\frac{1}{N_{mem} - 1} \sum_{mem} (P_{mem} - \overline{P})^2} \tag{20}$$

The FBI, ETS and DAS were as well averaged over the available group members. Then the relative spread (in the graphs called "normalized spread"), which is the spread within the group devided by the group mean, was calculated separately for each group. The relative spread is employed since it makes the different groups of members comparable: otherwise high mean values would automatically cause high spread values. Then spread-skill relationships for each day and for the entire period were obtained. The latter were separated by the different groups of members and additionally by a threshold value of the convective time scale (6h) to distinguish between the two different regimes.

Finally, plots of $\tau_c$ versus the relative spread of each score within the different groups were created in order to identify a possible connection between these quantities. Correlation coefficients r were calculated to examine a possible connection between the two variables. In the following equations the FBI will be used to demonstrate these calculations:

$$r_{\tau FBI} = \frac{s_{\tau FBI}}{s_\tau s_{FBI}} \tag{21}$$

while $s_\tau$ and $s_{FBI}$ are the standard deviations of the parameters analysed, and $s_{\tau FBI}$ is the common covariance of the FBI and $\tau_c$:

$$s_{\tau FBI} = \frac{1}{N-1} \sum_{i=1}^{N} (\tau_i - \overline{\tau})(FBI_i - \overline{FBI}) \tag{22}$$

A subsequent t-test was applied to verify statistical significance. The null hypothesis "$r_{\tau FBI} = 0$" can be refused if the critical t-value is lower than the test function t:

$$t = \frac{r_{\tau FBI}\sqrt{N-2}}{\sqrt{1-r_{\tau FBI}^2}}. \tag{23}$$

The critical t-value depends on the desired confidence level and the proper number of data pairs N. Using these two values the critical t-value can be obtained from statistical tables (BOSCH 2005).

# Chapter 4

# Results

## 4.1 Forced-frontal convection over the DE region

### 4.1.1 Case study: 07 July 2009

#### Synoptics and the convective time scale

First a classical weather analysis is considered. In the weather chart a large cold front is shown in the east of Germany which has passed the model area during the course of the day. A warm front from the south and an occlusion from the north influenced Germany as well. During the last hours of the day the model area was influenced by an occlusion

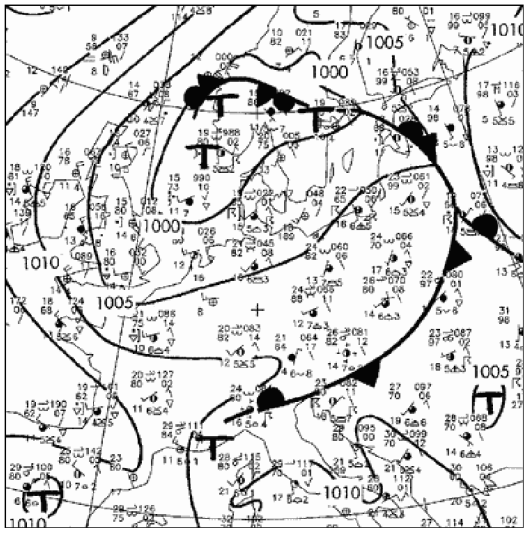


**(a)** Weather chart from 07 July 2009 12 UTC

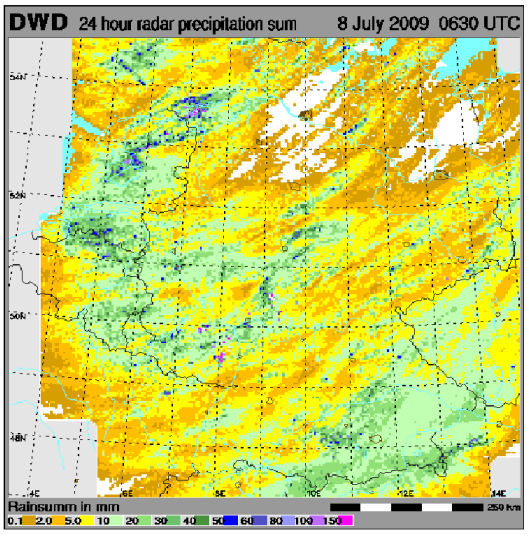


**(b)** 24 hour radar precipitation sum until 08 July 2009 06:30 UTC

**Figure 6:** DWD weather charts and DWD 24 hour precipitation (sum from 6:30 UTC of the previous day to 06:15 UTC of the actual day) from 07 July 2009.

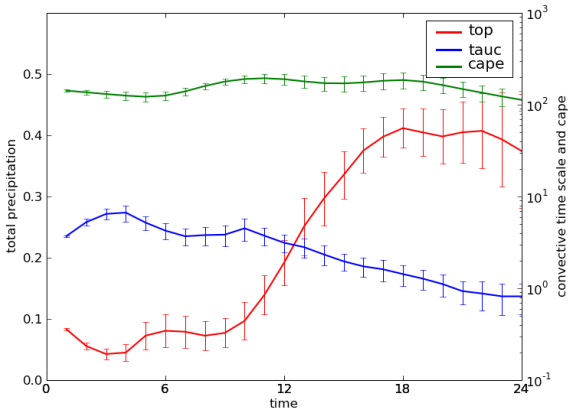


**(a)** All members

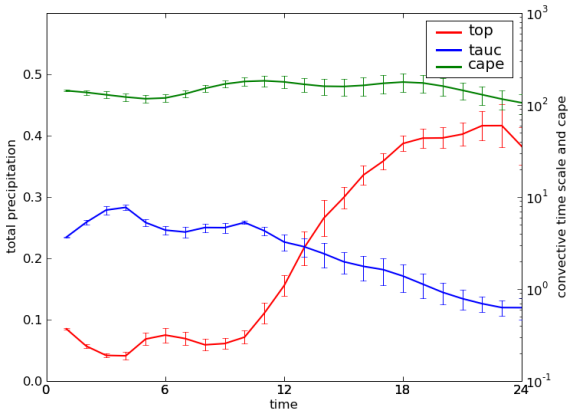


**(b)** ECMWF members

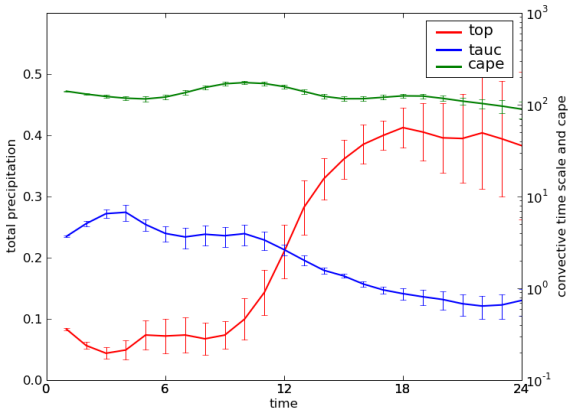


**(c)** Entrainment rate members

**Figure 7:** Time series for the DE region on 7 July 2009 with precipitation (red) on the left y-axis, CAPE (green) and $\tau_c$ (blue) on the right y-axis. Errorbars display standard deviations.

from the west. In Figure 6b continuous precipitation over almost the whole of Germany can be noticed. Sustained areas with the same amount of precipitation propagating can be identified. The chart indicates the movement of a front from southwest to northeast, since precipitation features are generally pushed along with the front. That means that larger areas with the same amount of precipitation are created in direction of the frontal movement. The radar chart is also consistent with the position of the front in Figure 6b. An "eyeball" verification by a forecaster would assign this day to the forced-frontal regime.

Figure 7 displays three time series of the total precipitation, the CAPE and $\tau_c$. Averaged over all members (Figure 7a), the CAPE ranges between $110\frac{J}{kg}$ and $195\frac{J}{kg}$. The precipitation is in the range between $0.04\frac{mm}{h}$ and $0.41\frac{mm}{h}$. This quantity is characterised

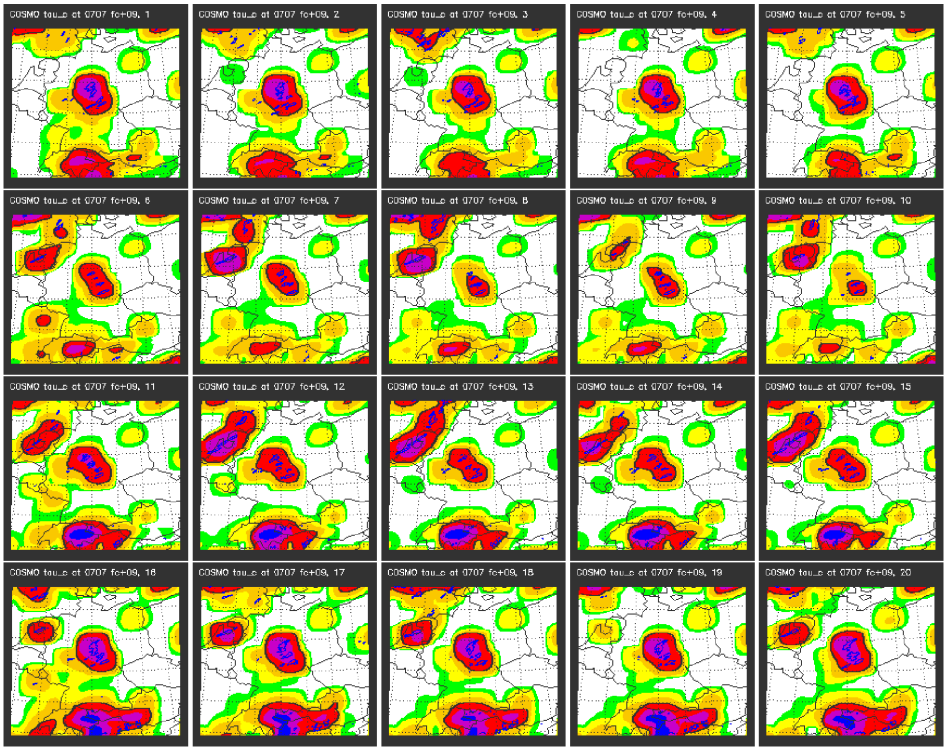

**Figure 8:** Stamp maps of the DE region displaying $\tau_c$ on 07 July 2009 09 UTC. The different maps are arranged as displayed in Figure 4. On the maps the following intervals of $\tau_c$ are illustrated with different colours: greater or equal than 300h (green), 100h - 300h (yellow), 3h - 100h (orange), 10h - 30h (red), 3h - 10h (violet), 1h - 3h (dark blue), 0.3h - 1h (light blue), 0.1h - 0.3h (black). White areas are either areas with no precipitation or if surrounded by black areas $\tau_c$ is in the range between 0.0001h and 0.1h. Blue contours show precipitation with an hourly precipitation exceeding $1\frac{mm}{h}$.

by high standard deviations. $\tau_c$ exhibits a minimum value of 0.8h and a maximum value of 6.7h with low standard deviations.

The other two time series in Figure 7 illustrate the differences if averaged over a certain subgroup of members only. In Figure 7b averages of the ECMWF members are displayed. In Figure 7c the time series with the averaging over the members with varied entrainment rate are shown.

All three lines in the different plots of Figure 7 are quite similar. But the standard deviations are striking: The standard deviation of precipitation, especially at the end of the day, is larger in Figure 7c (same model physics with different boundary conditions) than in Figure 7a. The standard deviation in Figure 7b (same boundary conditions with different model physics) is lower than in Figure 7a. Hence, these standard deviations suggest a sensitivity of the EPS for different lateral boundary conditions.

But this cannot be shown for $\tau_c$ since the CAPE, which is characterised by low standard deviations (considering the entrainment rate members), also plays a role for the computation of $\tau_c$. However, the standard deviations of $\tau_c$ in all three graphs are low and do not differ significantly.

Figure 8 allows "eyeball" verification. The general structure and the minimum values of $\tau_c$ are controlled by the different lateral boundary conditions. At this point in time minimum values of $\tau_c$ can be found over Switzerland (in the interval between 1h - 3h), the Netherlands and central Germany (both between 3h - 10h). Members 1, 6, 11 and 16 show some deviation from the rest of their related BC group members over northeastern France.

Figures 7 and 8 are a first indication that the COSMO-DE-EPS is sensitive to different lateral boundary conditions on a day with forced-frontal convection.

#### Verification scores: Time series and spread-skill relationships

The quality of the performance of the COSMO-DE-EPS forecasts is verified by different quality measures. Time series and scatter plots of FBI, ETS and DAS will be presented in this section.

In the time series the same colour (cp. Figure 4a) represents one certain boundary condition, while the different line styles express the perturbations of the model physics.

The scatter plots display the average score of a certain group (BC and PHY) on the x-axis versus the associated relative spread of the score on the y-axis. The different black symbols represent averages of the BC groups while the different colours show averages of the PHY groups.

In Figure 9a the time series of the FBI is shown. Between 01 UTC and 18 UTC almost all members slightly underestimate the observed precipitation. The UKMO members (16 - 20) show an overestimation for some points in time in the first half of the day (until 10 UTC). In this period the BC members behave similarly. By contrast, the members

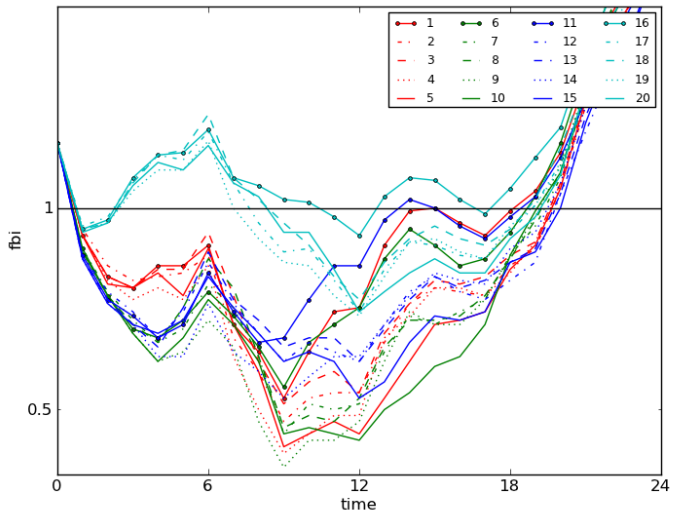


**(a)** Time series of the FBI. The colours denote the different lateral boundary conditions: ECMWF (red), DWD (green), NCEP (dark blue), UKMO (light blue). The line styles represent the perturbations of the model physics: entrainment rate (continuous line with dots), cloud cover at saturation (dashed - dotted), low laminar layer depth (dashed), high laminar layer depth (dotted), turbulent length scale (continuous line). The black horizontal line represents the perfect score of 1.

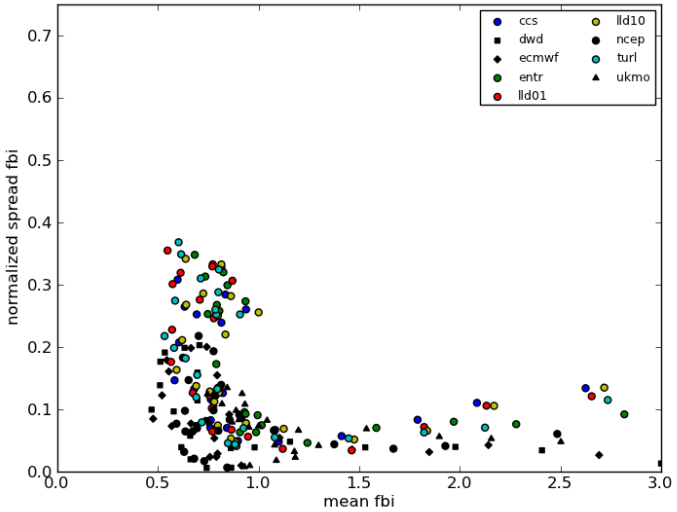


**(b)** Spread-skill relationship of the FBI. The black symbols represent averages over the same lateral boundary conditions: ECMWF (diamonds), DWD (squares), NCEP (circles), UKMO (upward triangles). The colours denote averages over the same physical perturbations: entrainment rate (green), cloud cover at saturation (dark blue), low laminar layer depth (red), high laminar layer depth (yellow), turbulent length scale (light blue).

**Figure 9:** Time series and spread-skill relationship of the frequency bias.

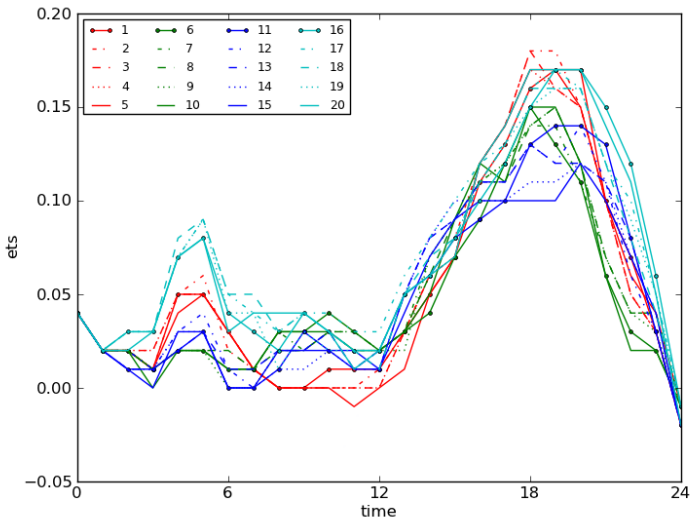


**(a)** Time series of the ETS.

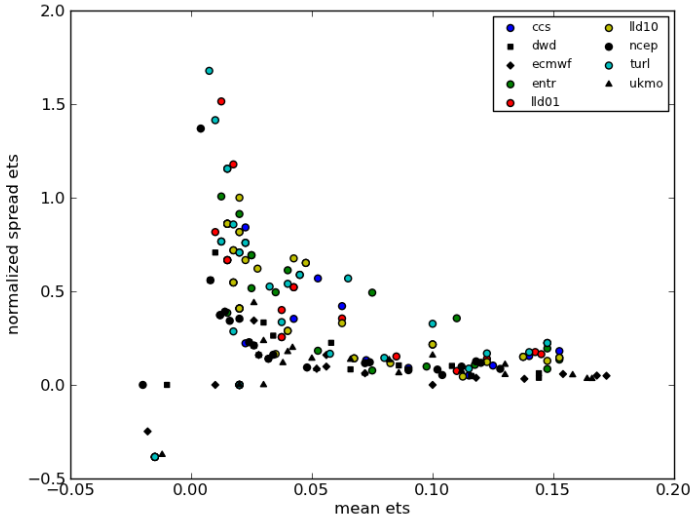


**(b)** Spread-skill relationship of the ETS.

**Figure 10:** As Figure 9 but for the equitable threat score.

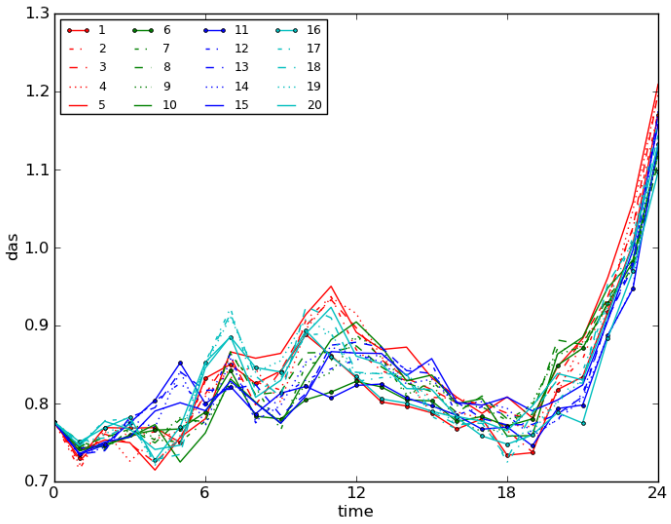


**(a)** Time series of the DAS.

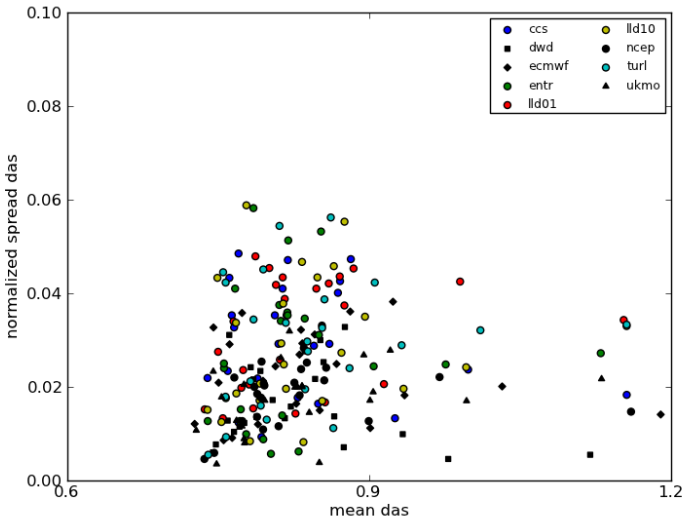


**(b)** Spread-skill relationship of the DAS.

**Figure 11:** As Figure 9 but for the displacement and amplitude score.

of a certain PHY group exhibit big differences. Hence, the lateral boundary conditions control the EPS more than the model physics.

Figure 9b displays the spread-skill relationship of the FBI. It is characterised by group means of the FBI between 0.5 and 3. Most of the group means are located between 0.5 and 1. In general, the BC members exhibit a lower spread than the PHY members. Thus, the performance of the EPS is governed by the lateral boundary conditions.

Figure 10a shows ETS values of up to 0.18. Most of these values are positive. The members of the different BC groups do not deviate much from each other. By contrast, the members of each PHY group behave differently. During the largest part of the day the ECMWF members (1 - 5) and the UKMO members (16 - 20) perform better than the rest of the BC groups.

The spread-skill relationship (Figure 10b) confirms the importance of the lateral boundary conditions : the relative spread of the BC groups is basically lower than the spread of the PHY groups. Hence, the ETS shows the controlling of the EPS by the boundary conditions, just like the FBI did.

Figure 11a displays the time series of the DAS. The DAS values are between 0.7 and 1.2; the highest values are obtained at the end of the day. In general, all the members behave similarly. It is not possible to identify a better performing group of members since all different BC groups show lowest values for certain points in time. However in the first half of the day, the individual BC group members are close within each group. But in the second half of the day, members 1, 6, 11, 16 (varied entrainment rate) perform best.

The scatter plot for this day (Figure 11b) gives more information. The mean values and the relative spread values are low in general. Like in in Figures 9b and 10b, the spread within the BC groups is lower than the spread within the PHY groups. Hence, the DAS also shows the dominance of the lateral boundary conditions on a forced-frontal day.

### 4.1.2 Extension of the analysis to four representative days: 07, 12, 17, 22 July

The 07, 12, 17 and 22 July have been chosen as typical days for the equilibrium regime. On 07 July all 20 members were available, while on the other three days only 15 members could be analysed.

Precipitation fell permanently during those days (cp. Figure 12). At the beginning of 12 July especially Northern Germany was influenced by a warm front. Later the model area was also influenced by a cold front which caught up to the warm front at the end of the day. Although the fronts were present, the area-averaged precipitation did not exhibit very high values since mainly Northern Germany was affected. On 17 July precipitation reached high values and peaks twice: At 00 UTC only one warm front occurred which caused light precipitation. Six hours later the model area became influenced additionally by a cold front. Around 12 UTC the influence of the cold front weakened. But it amplified again at about 18 UTC which explains the second peak in the graph. The first part of 22 July was influenced by a warm front over Northern Germany. This warm front left the model area. A subsequent cold front appeared during the second half of the day.

The time scale of convective adjustment is in accordance with the forced-frontal regime: $\tau_c$ is rarely higher than 6h. The very low values on 12 July (minimum slightly over 0.01h) are a result of the low CAPE values. On 22 July the maximum of $\tau_c$ is a result of high CAPE values (up to 700 J/kg) combined with low amounts of precipitation.

Figure 13 displays time series of FBI, ETS and DAS on four days (07, 12, 17 and 22 July) during the forced-frontal regime. All points in time are meaningful, since this type of convection does not depend on the time of day. The FBI values (Figure 13a) are close to 1. At many points in time precipitation is overestimated, i.e. FBI is higher than 1. The ETS (Figure 13b) shows high values (up to over 0.5). This implies a high forecast

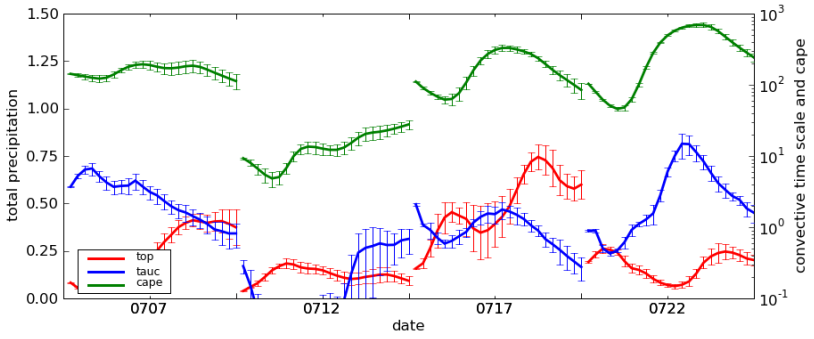


**Figure 12:** As Figure 7, but for the DE region on four days (07, 12, 17, 22 July 2009) during the forced-frontal regime.

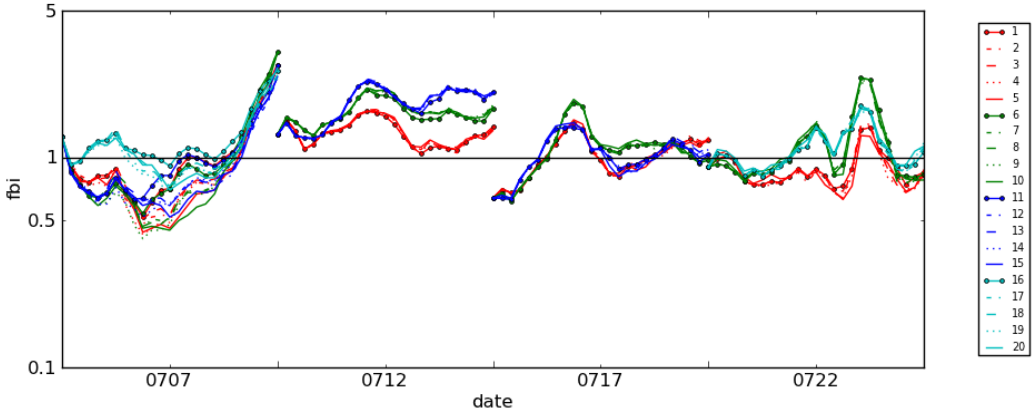


**(a)** FBI

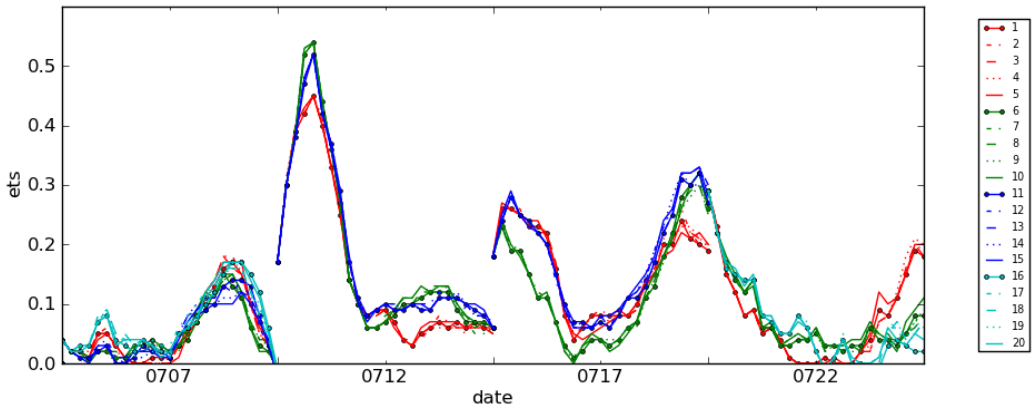


**(b)** ETS

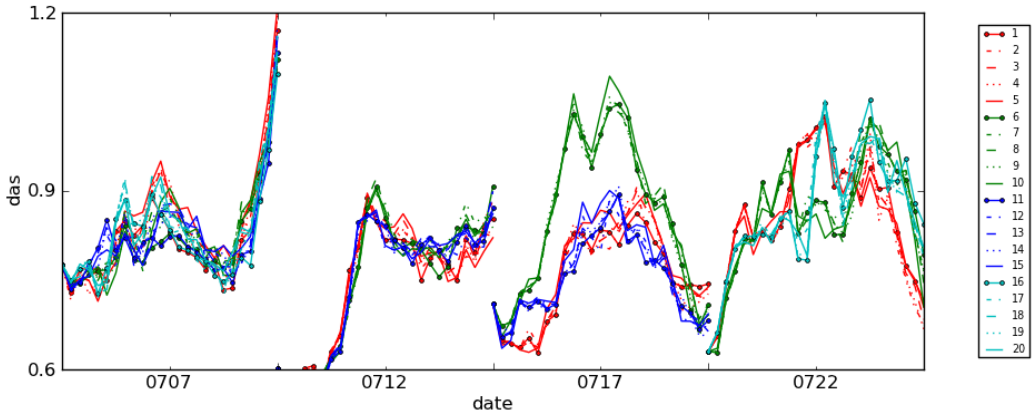


**(c)** DAS

**Figure 13:** Time series of FBI, ETS and DAS for the DE region on 07, 12, 17 and 22 July 2009, legend as in Figure 9a. Time series of each day separately can be found in the appendix: Figures A4, A5 and A6.

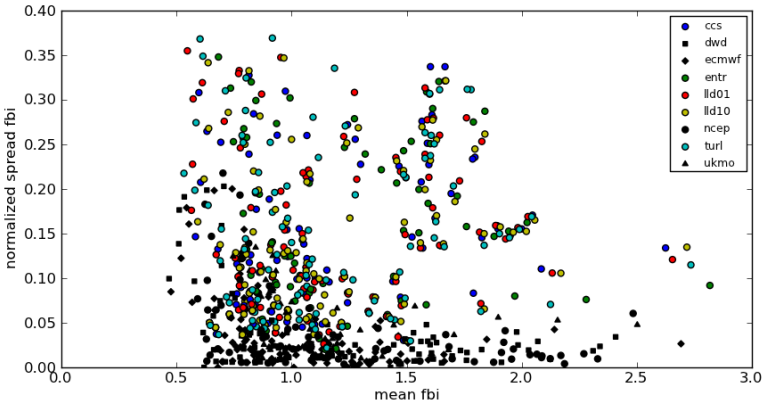


**(a)** FBI

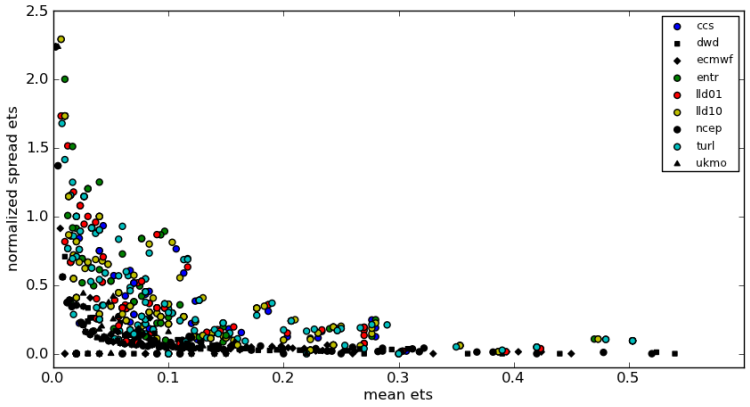


**(b)** ETS

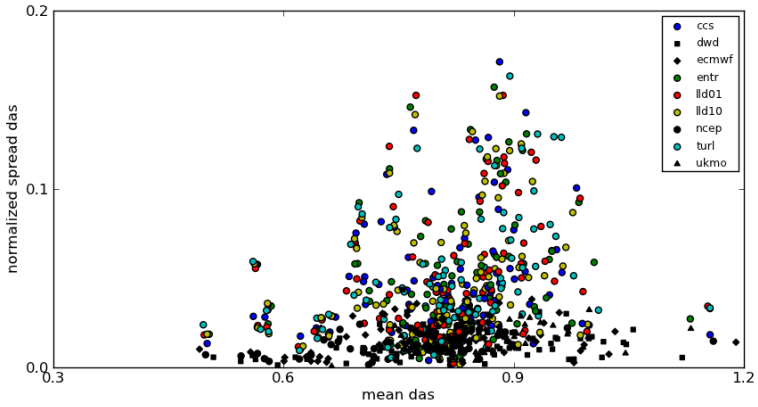


**(c)** DAS

**Figure 14:** Scatter plots of FBI, ETS and DAS for the DE region with values of 07, 12, 17, 22 July, legend as in Figure 9b.

skill. The DAS in Figure 13c ranges between 0.6 and 1.2 with its lowest values on 12 July. On the four analysed day the DAS has its highest forecast quality for short lead times. This is not pointed out so clearly by FBI and ETS. All three graphs of Figure 13 have in common that lines with the same colours (same boundary conditions) behave in a similar manner while the different PHY members differ from each other. In the DAS time series on 17 July the ECMWF members (6 - 10) are outstanding since they show higher values and thus a lower skill than the rest of the groups. In the other two graphs the ECMWF members do not stand out as clearly.

Scatter plots of the four days are shown in Figure 14. Most of the FBI (Figure 14a) mean values lie between 0.5 and 2.0. The ETS means (Figure 14b) are lower than 0.55. The lower the average of the ETS, the more scatter points can be noticed. With lower mean values higher spread values can be observed. In Figure 14c the majority of the DAS means are in the interval of 0.6 and 1. All three graphs are characterised by lower spreads within the BC groups and higher spreads within the PHY groups.

These examinations confirm the results of section 4.1.1: Forecast precipitation is sensitive to lateral boundary conditions if forced-frontal convection occurs.

## 4.2 Local-forced convection over the DE region

### 4.2.1 Case study: 30 June 2009

#### Synoptics and the convective time scale

First the synoptics are analysed as well: in Figure 15 weather charts and 24h radar precipitation are displayed. In the weather chart no influence by a front can be observed, apart from a cold front which maybe influences a small part of the northeast later on that day. The radar analysis is characterised by large areas of precipitation over Rhineland-Palatinate, Saarland, parts of Hesse and North Rhine-Westphalia, the south and west of Baden-Württemberg, the south and east of Bavaria and in general the whole eastern part of Germany. In these precipitation areas spotty precipitation maxima can be identified. Some spotty precipitation areas can also be found over the rest of Germany. This very spotty structure is typical for triggered convection. Analysing the weather chart a forecaster would assign this day to be in the non-equilibrium regime.

Figure 16 shows time series of the total precipitation, CAPE and $\tau_c$. Averaged over all members (Figure 16a), the CAPE ranges between $130\frac{J}{kg}$ and $550\frac{J}{kg}$. The total precipitation lies between $0.02\frac{mm}{h}$ and $0.15\frac{mm}{h}$. Hence, the CAPE values are higher and the precipitation values lower than in the equilibrium regime. The timescale of convective

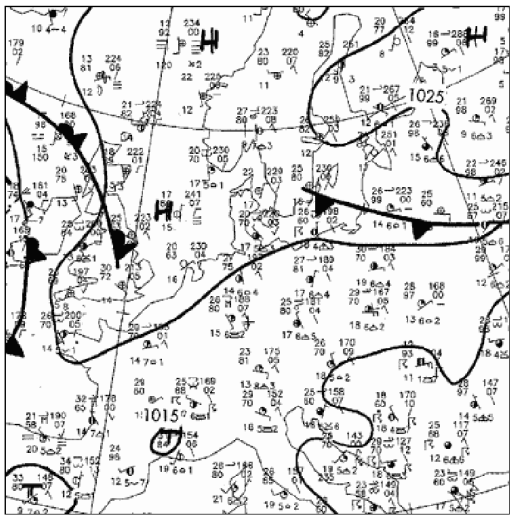


**(a)** Weather chart from 30 June 2009 12 UTC

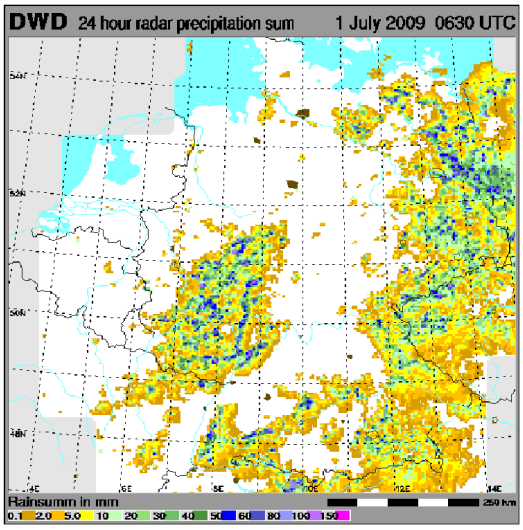


**(b)** 24 hour radar precipitation sum until 01 July 2009 06:30 UTC

**Figure 15:** As Figure 6, but for 30 June 2009.

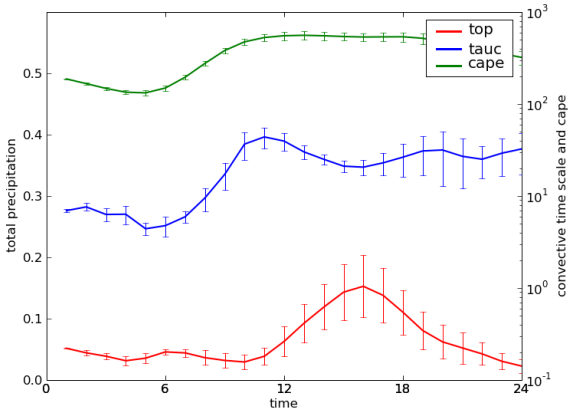


**(a)** All members

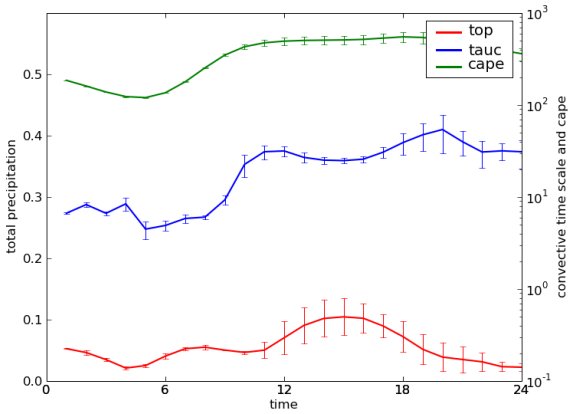


**(b)** ECMWF members

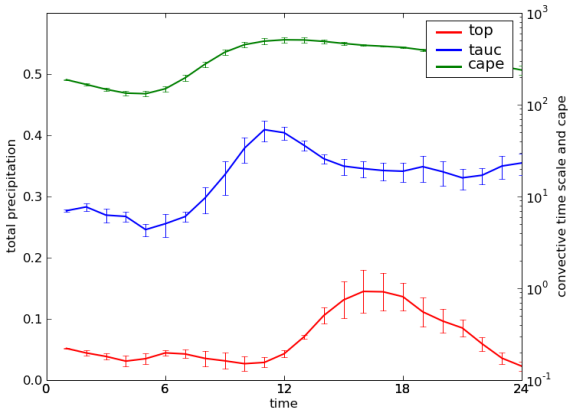


**(c)** Entrainment rate members

**Figure 16:** As Figure 7, but for 30 June 2009.

adjustment ranges between 4.4h and 40h. Most of its values are significantly higher than on 07 July, and thus higher than 6h. This is in agreement with 30 June being an example for the non-equilibrium regime.

The other two time series illustrate the differences if averages of a certain group of members are computed. Figures 16b and 16c respectively show averages of the ECMWF members and of members with varied entrainment rate. Again all three time series behave in a similar manner. However, there are some differences. The peak of the total precipitation in Figure 16b during the convective period (10 UTC - 17 UTC) cannot be identified as clearly as in the other two graphs. During the convective period the standard deviations of precipitation are highest if averaged over all members. The referring standard deviation of the entrainment rate members is slightly lower than the standard deviation of the ECMWF members. But it is just the opposite for $\tau_c$.

Figure 17 allows "eyeball" verification. Members with the same varied physical parameter show similar general structures. This is most evident comparing those members of members 1 - 10 which exhibit the same model physics with each other. However, the coarse structure with the minimum values of $\tau_c$ is rather governed by the different lateral boundary conditions. The minimum values of $\tau_c$ (in the range between 10h and 30h) occur in the border region of Italy and Austria.

#### Verification scores: Time series and spread-skill relationships

In this section time series and spread-skill relationships of FBI, ETS and DAS will be presented in order to analyse the quality of the performance of the COSMO-DE-EPS.

The time series of the FBI (Figure 18a) show an overestimation of the forecast precipitation before 10 UTC for all model members. Between 10 UTC and 20 UTC all members underestimate precipitation while after 20 UTC some members demonstrate overestimation, others underestimation. During the convective period, between 10 UTC and 17 UTC, the performance of members 5, 10, 15 and 20 evidently is worse than the performance of the other members. In general, during this period the FBI is rather governed by the model physics than by the lateral boundary conditions. In the scatter plot (Figure 18b) the BC groups with a high FBI (greater than 1) exhibit a lower spread than the corresponding PHY groups. By contrast, the PHY groups show lower spread values than the BC groups when the FBI is lower than 1. This part of the plot - when the FBI is smaller than 1 - represents the convective period between 10 UTC and 17 UTC from Figure 18a. The lower spread of the PHY members in this period is a sign for the domination of the EPS by the model physics.

A time series of the ETS is displayed in Figure 19a. On 30 June the accuracy of the calculated ETS is 4 decimal places in order to distinguish between the different lines more clearly. The accuracy for all the other parameters and for most of the other days is 2 decimal places. The values of the ETS are mostly positive but do not exceed 0.06. This is a very low value since a value of 0 means "no skill". The UKMO members (16

- 20) perform best (highest values during some periods). Another group can hardly be identified. However, between 10 UTC and 14 UTC (part of the convective period) the members with varied entrainment rate (1, 6, 11, 16) behave similarly: they exhibit lower ETS values than the rest of the EPS. Figure 19b confirms that neither the BC groups nor the PHY groups can be identified as having a lower relative spread. Hence, a certain group of members which control the behaviour of the EPS cannot be identified.

The DAS (Figure 20a) ranges between 0.7 and 1.1. During the convective period the members with varied entrainment rate (1, 6, 11, 16) and with varied turbulent length scale (5, 10, 15, 20) perform worst. The other members show slightly better performances. During the rest of the day the members of each BC group behave similarly while the best values are achieved by the UKMO group (members 15 - 20) at 09 UTC and 10 UTC. The DAS does not separate as clearly as the FBI (cp. Figure 18a) between underestimation and overestimation: the precipitation features are expanded by a divergent vector field in case of underestimation and compressed by a convergent vector field in case of overestimation. Therefore, the scatter plot (Figure 20b) shows no favouritism for the controlling of the EPS by either the BC groups or by the PHY group.

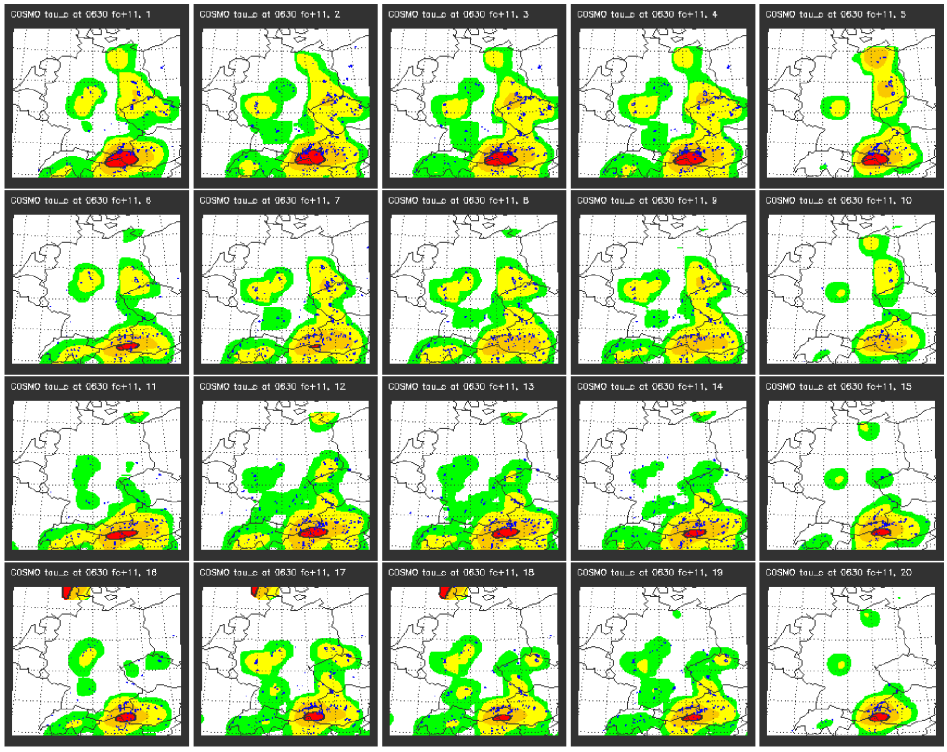

1

**Figure 17:** As Figure 8, but for 30 June 2009 11 UTC.

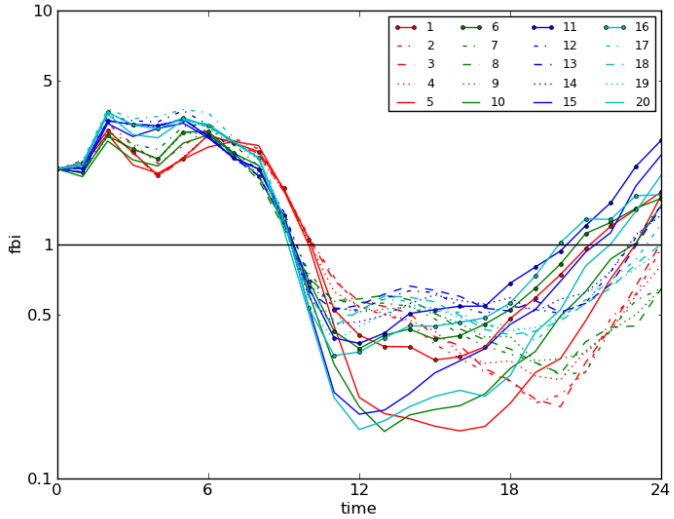


**(a)** Time series of the FBI.

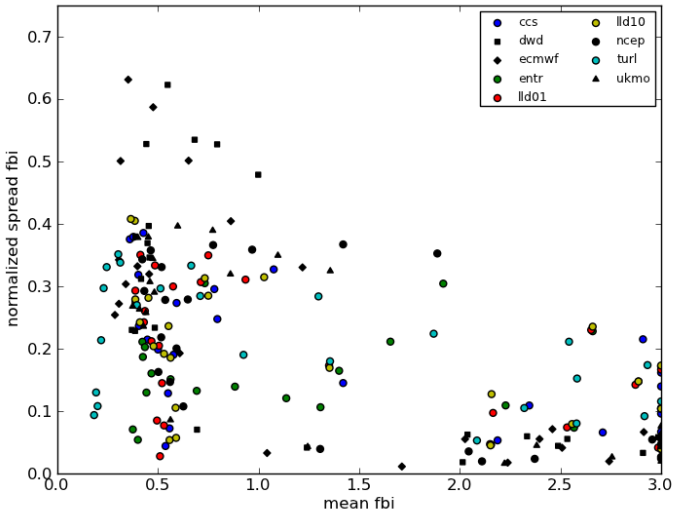


**(b)** Spread-skill relationship of the FBI.

**Figure 18:** As Figure 9, but for the frequency bias on 30 June.

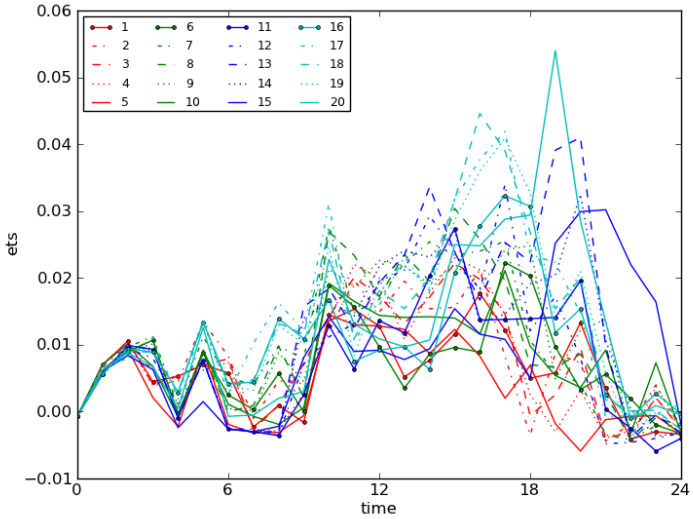


**(a)** Time series of the ETS.

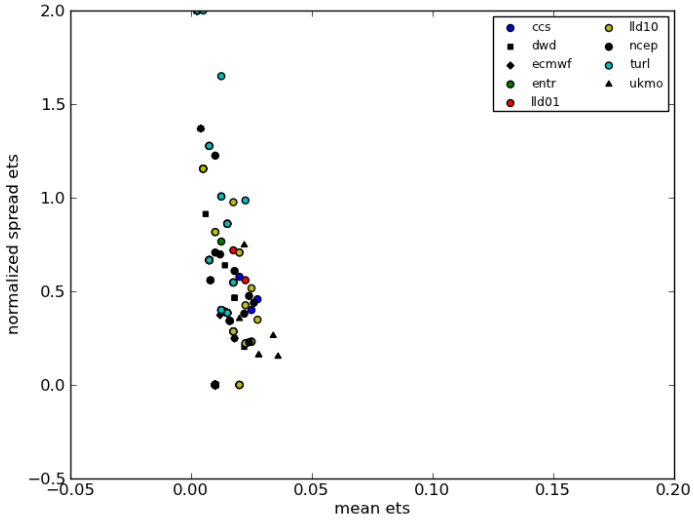


**(b)** Spread-skill relationship of the ETS.

**Figure 19:** As Figure 9, but for the equitable threat score on 30 June.

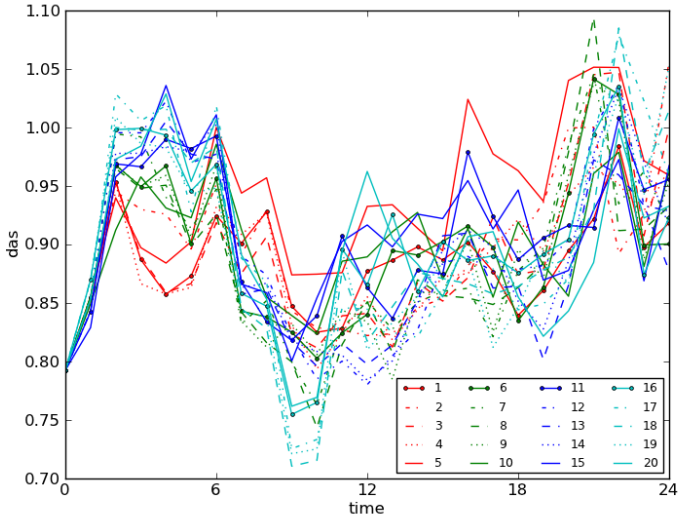


**(a)** Time series of the DAS.

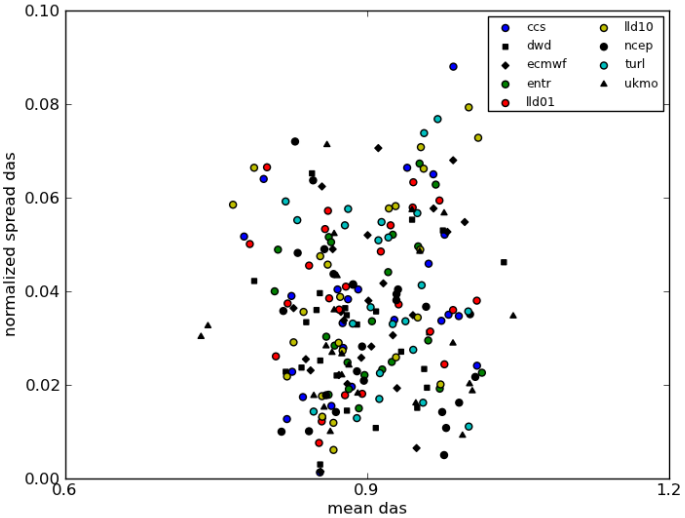


**(b)** Spread-skill relationship of the DAS.

**Figure 20:** As Figure 9, but for the displacement and amplitude score on 30 June.

### 4.2.2 Extension of the analysis to four representative days: 30 June - 03 July

Four days have been selected to extend the validity of the results from section 4.2.1. The period from 30 June to 03 July will exemplify the non-equilibrium regime. Weather charts of those day are characterised by a lack of fronts over the whole model area. On 30 June and 02 July all 20 members were available, on 01 July only 10 and on 03 July 15.

Between 30 June and 03 July the maximal precipitation can be observed in the afternoon (15 UTC till 16 UTC in Figure 21). Precipitation does not exceed 0.32 $\frac{mm}{h}$. The CAPE values of up to 700 $\frac{J}{kg}$ are higher than during the equilibrium regime. These are clear signs for local-forced convection. This is emphasised by the time scale of convective adjustment: The values of $\tau_c$ are higher than 6h during the whole period. They peak at 65h at the beginning of 02 July.

To obtain an idea of the performance of the EPS during this period Figure 22 is analysed. Before sunrise, in the early morning as well as in the late afternoon and after sunset the FBI, ETS and DAS values are mostly governed by the lateral boundary conditions of the EPS. This can be seen more or less clearly in the morning of 01 and 03 July (Figures 22a, 22b and 22c). But those times of day are not the most interesting ones, since triggered convection occurs mainly from the late morning to the late afternoon. Therefore, in this period the main focus was laid on the points in time between 10 UTC and 17 UTC.

All available members underestimate precipitation (FBI lower than 1) and a strong dependency on the model physics can be observed. The lowest FBI values are obtained by the members with varied asymptotic mixing length of the turbulence scheme (5, 10, 15, 20) while the other groups exhibit similar skills (higher FBI values). The ETS (Figure 22b) basically illustrates the same: Members 5, 10, 15, 20 and members 1,

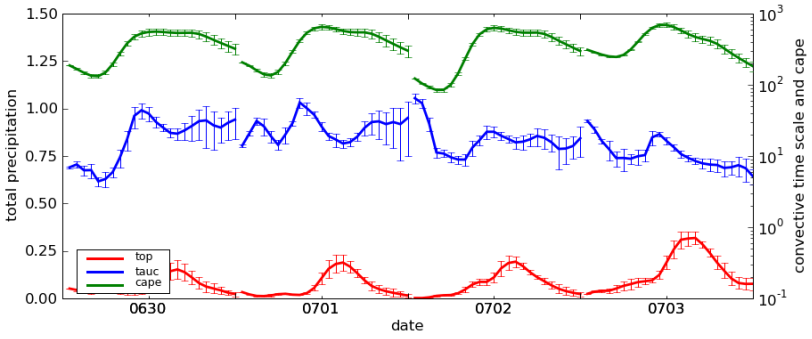


**Figure 21:** As Figure 7, but for the DE region on four days (30 June - 03 July 2009) during the local-forced regime.

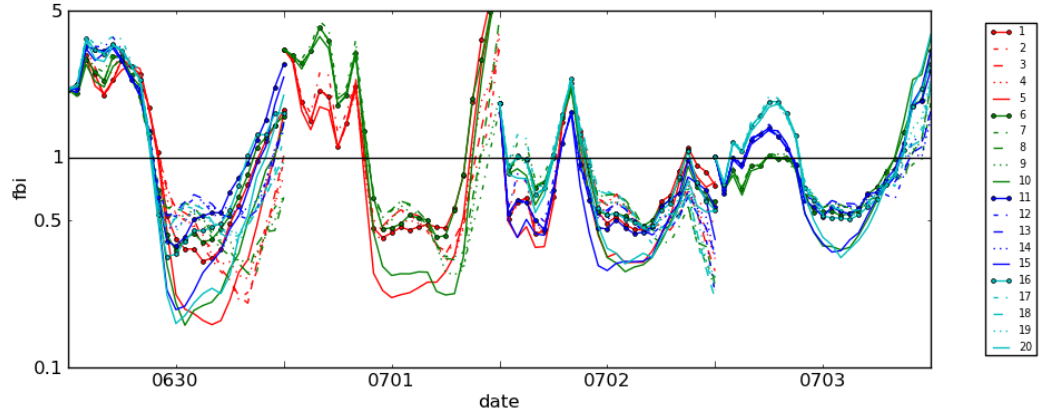


**(a)** FBI

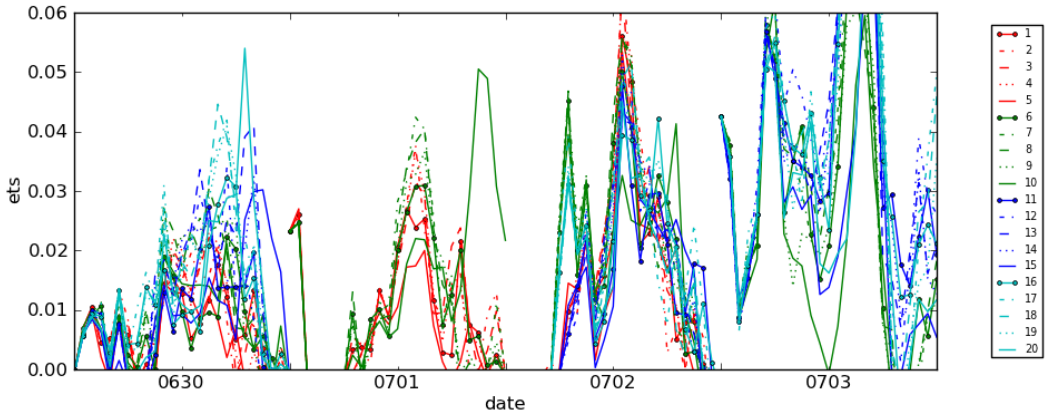


**(b)** ETS

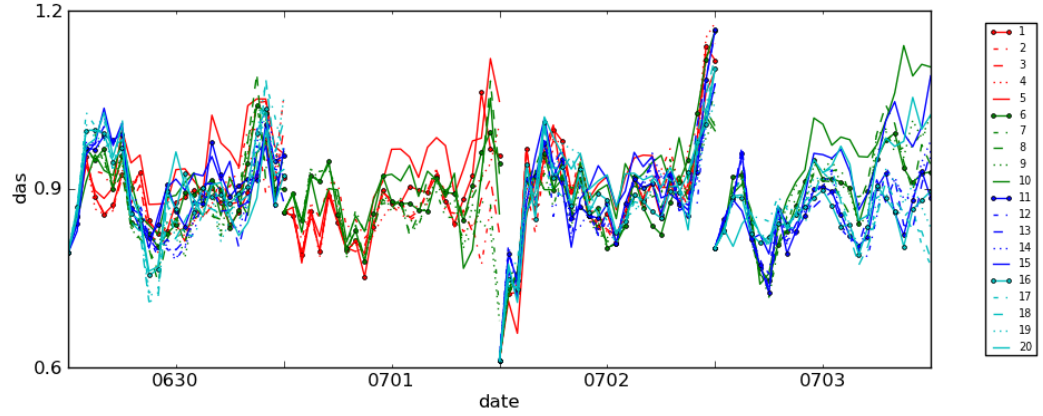


**(c)** DAS

**Figure 22:** Time series of FBI, ETS and DAS for the DE region from 30 June to 03 July 2009, legend as in Figure 9a. Time series of each day separately can be found in the appendix: Figures A1, A2 and A3.

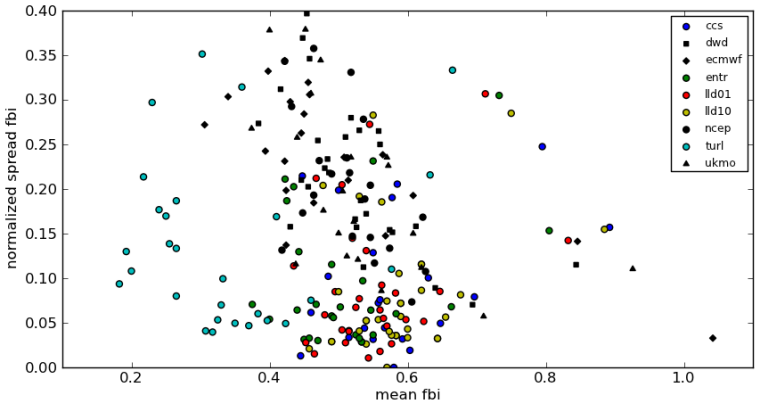


**(a)** FBI

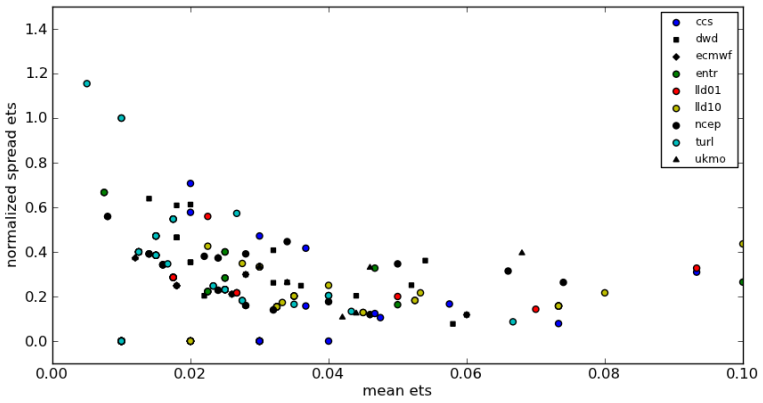


**(b)** ETS

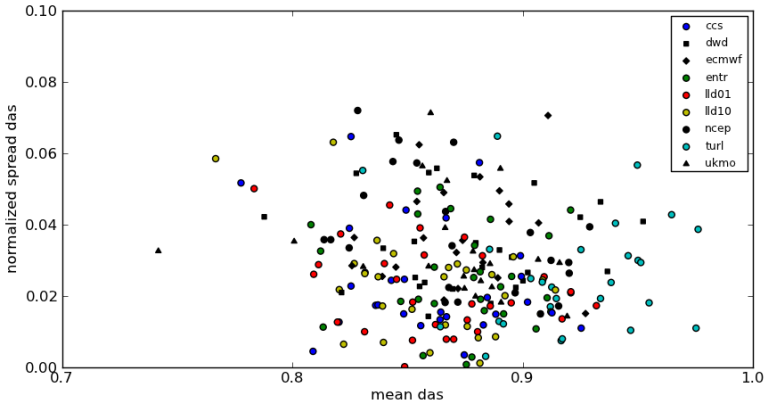


**(c)** DAS

**Figure 23:** Scatter plot for the DE region with values of the period from 30 June to 03 July 2009 (from 10 UTC to 17 UTC only), legend as in Figure 9b.

6, 11, 16 exhibit the lowest values. However, the ETS does not allow such a clear distinction between the different model physics due to its very low values. The merely small differences between the curves impede a more explicit distinction as well. The ETS graph was "cut" at a maximum value of 0.06 in order to show at least some differences between the curves. In this period, the maximum ETS value of 0.13 was obtained on 03 July. The DAS in Figure 22c, by contrast, allows a more clear distinction between the different perturbations of physical parameters: the highest values are obtained by the members with varied asymptotic mixing length, like the FBI suggested. Best values cannot be found unambiguously. All the other groups with varied model physics behave in a very similar manner.

The scatter plots in Figure 23 underline those findings. These scatter plots incorporate only averages and relative standard deviations from 10 UTC till 17 UTC. The mean values of the FBI (Figure 23a) are distributed around 0.5, hence the precipitation was generally underestimated by the EPS during this convective period. The PHY groups exhibit lower spread values than the BC groups. The scatter points with varied asymptotic mixing length of the turbulence scheme (light blue) show significantly lower mean values than the rest of the points while some of them also exhibit higher spread values. This confirms the impression from Figure 22a. The ETS (Figure 23b), by contrast, does not favour one of the groups to have a higher or lower spread. Thus, in this case the ETS cannot be used to identify the non-equilibrium regime. Most of the DAS means (Figure 23c) lie between 0.8 and 0.95. The spread values of the BC groups can be considered higher than the spread values of the PHY groups. The highest (i.e. worst) mean values of the DAS are those in light blue (varied maximal turbulent length scale). Consequently, local-forced convection can be identified by a statistical analysis of the FBI and the DAS.

In general, the forecast quality measured with the ETS is lower during the non-equilibrium regime than during the equilibrium regime. The non-equilibrium regime is also characterised by higher relative spread values.

## 4.3 Scatter plots of the DE region data over the entire period

In a further step the entire data set was examined to obtain a complete picture of the performance of the COSMO-DE-EPS. Figures 24a (FBI), 25a (ETS) and 26a (DAS) are scatter plots displaying hourly means versus relative spread. Figures 24b, 25b and 26b are basically diagrams with the same scatter points. But in these graphs the colours indicate if $\tau_c$ was lower or higher than the threshold value of 6h at the point in time referring to the scatter point. However, some points are missing in Figures 24b, 25b and 26b: at certain points in time $\tau_c$ could not be calculated. Hence, a separation was not possible either.

In Figure 24a the coloured points (PHY groups) exhibit a higher relative spread and a lower forecast quality than the black symbols (BC groups). The large amount of black symbols exhibiting a lower spread than the coloured points indicate that in summer 2009 the equilibrium regime predominates the behaviour of the EPS (cp. Figure 14). This is consistent with most of the days in summer 2009 belonging to the equilibrium regime (cp. Table 2). The scatter plot in Figure 24b shows a separation by $\tau_c$. In this graph two groups can be identified: the majority of the red squares ($\tau_c > 6$h) is characterised by low means and high spreads, the majority of the blue points ($\tau_c < 6$h) exhibits high mean values and low spread values.

The average value of the points of the local-forced regime is around 1.6, the average value of the forced-frontal regime around 2.4. The spread values are 0.35 and 0.18 respectively, i.e twice as high within the local-forced regime (cp. Table 4). Most of the points with low spread resulting from the BC groups (black symbols in Figure 24a) can be assigned to the equilibrium regime (blue points in Figure 24b). Hence, the forced-frontal regime is in particular governed by the lateral boundary conditions. The forecast quality is generally influenced by the type of convection.

The question may arise why some of the scatter points are arranged in parallel, straight lines. These lines stem from the logarithmic axes in combination with the normalisation of the spread. The mean and the spread are connected by the following equation:

$$relative\ spread = \frac{spread}{mean} = spread * mean^{-1} \tag{24}$$

where spread will be assumed as a constant in the following steps due to simplicity. Taking the logarithm of this equation leads to the following modifications:

$$\lg relative\ spread = \lg\left(spread * mean^{-1}\right) = \lg spread + \lg mean^{-1} = -\lg mean + \lg spread \tag{25}$$

This can be compared to a standard linear equation:

$$y = mx + t \tag{26}$$

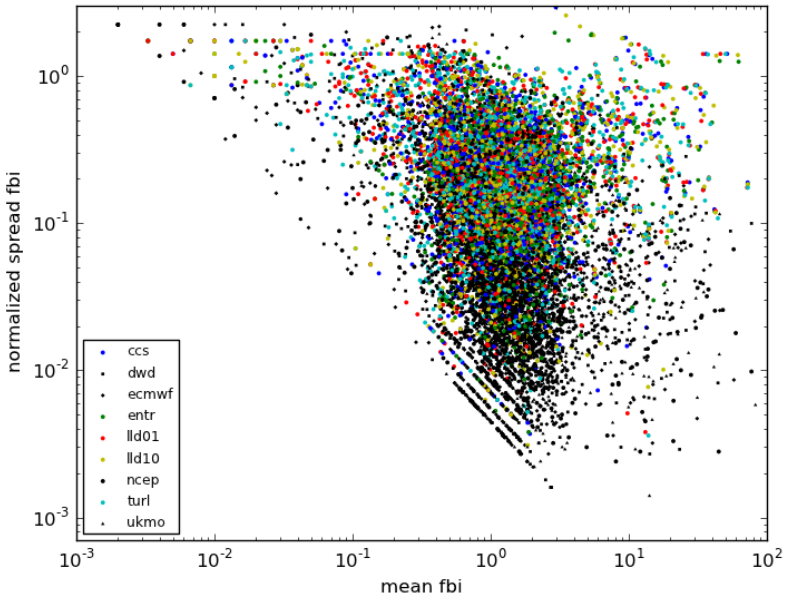


**(a)** Legend as in Figure 9b.

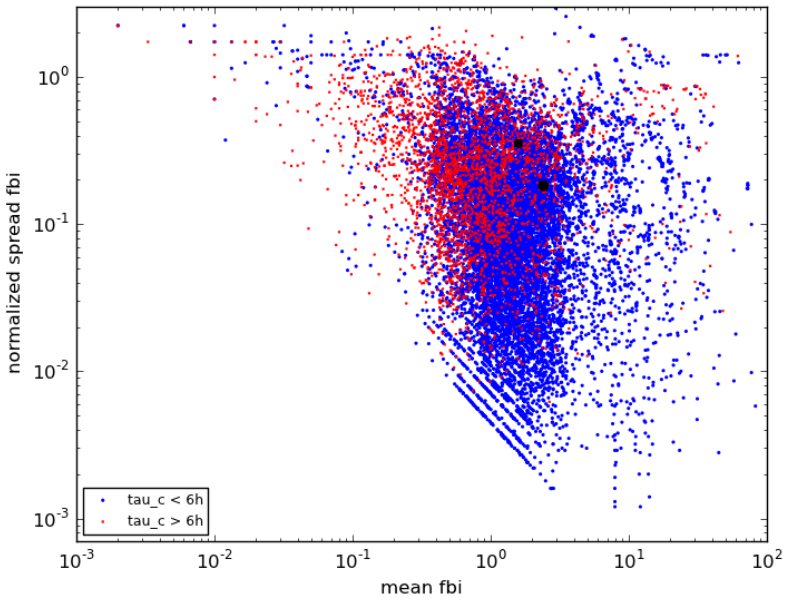


**(b)** Separation by the threshold value of $\tau_c$: the scatter points are blue when $\tau_c$ is higher than 6h, red when $\tau_c$ is lower than 6h. The black circle denotes the average over all points with $\tau_c$ lower than 6h (equilibrium regime), the black square the average over all points with $\tau_c$ higher than 6h (non-equilibrium regime).

**Figure 24:** Scatter plots of the FBI for the DE region with values from all available days and members. Both axes are logarithmic.

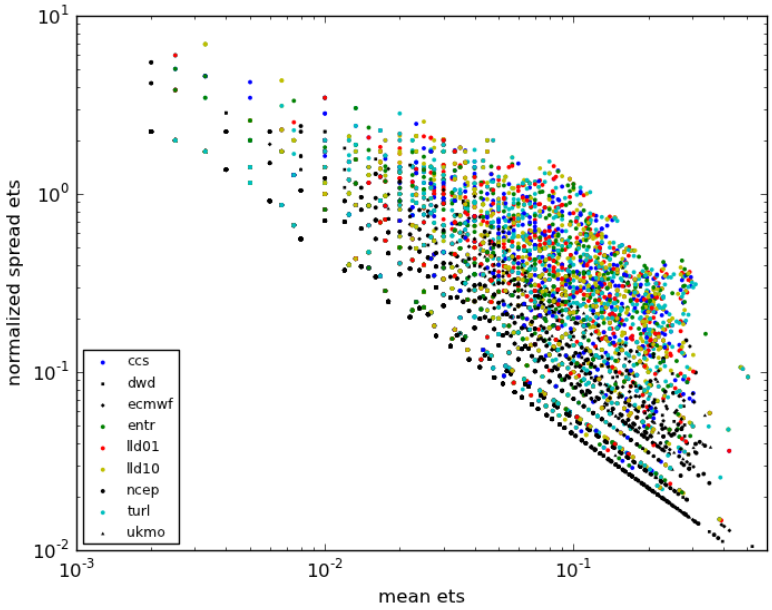


**(a)** Legend as in Figure 9b.

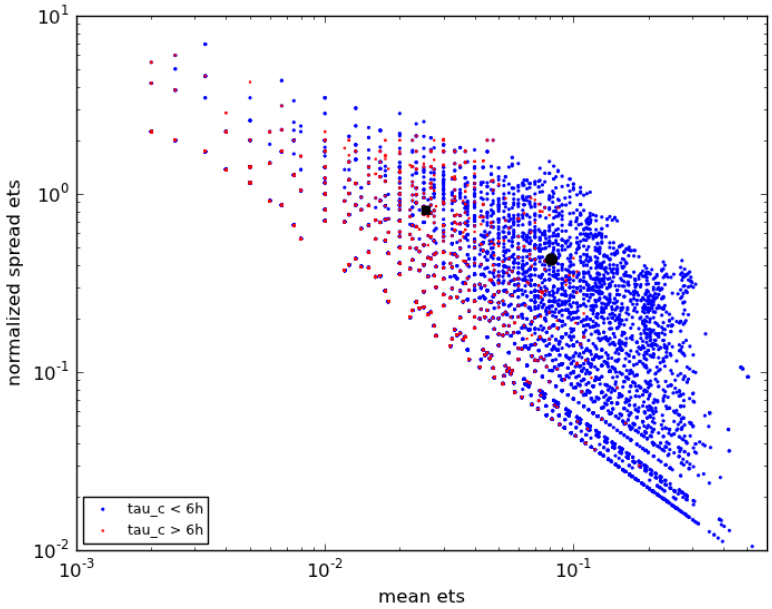


**(b)** Legend as in Figure 24b.

**Figure 25:** Scatter plots of the ETS for the DE region with values from all available days and members. Both axes are logarithmic.

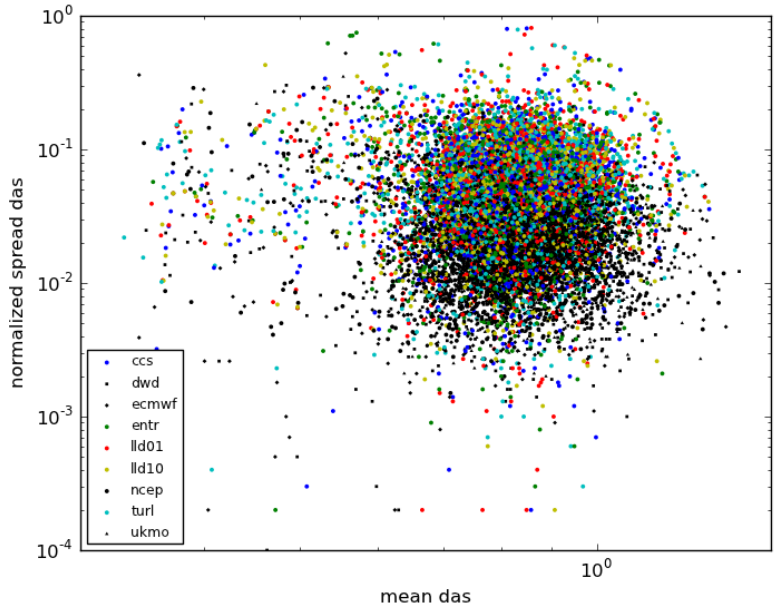


**(a)** Legend as in Figure 9b.

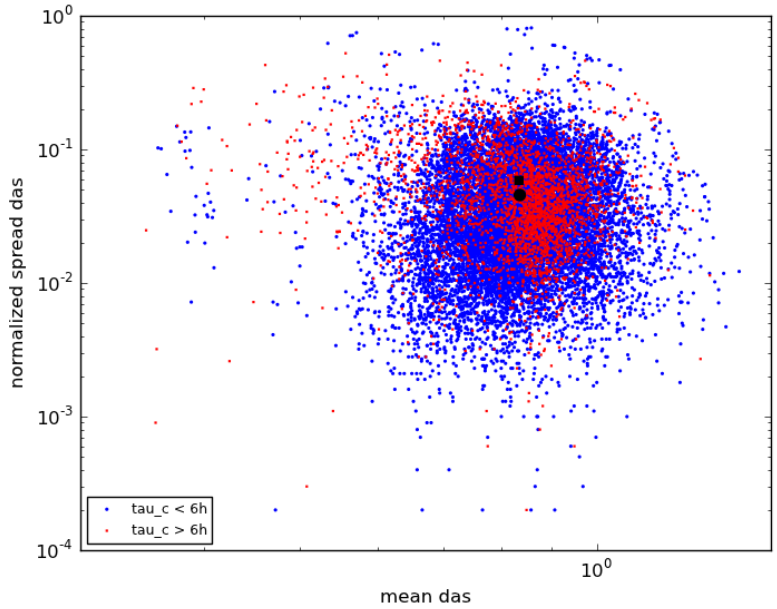


**(b)** Legend as in Figure 24b.

**Figure 26:** Scatter plots of the DAS for the DE region with values from all available days and members. Both axes are logarithmic.

| | FBI | ETS | DAS |
|---|---|---|---|
| mean frontal | 2.4130 | 0.0815 | 0.8354 |
| spread frontal | 0.1825 | 0.4284 | 0.0455 |
| mean local | 1.5882 | 0.0255 | 0.8337 |
| spread local | 0.3528 | 0.8093 | 0.0586 |

**Table 4:** Averages over the means and over the relative spreads of FBI, ETS and DAS for the DE region, separated by the local-forced and the forced-frontal regime.

where m is the gradient and t the section on the y-axis. In equation (25) $\lg spread$ can be compared to the section on the y-axis (spread = $e^t$). The gradient m would be -1 which is in agreement with the decreasing lines determined by the scatter points. $\lg relative\ spread$ and $\lg mean$ refer to y and x respectively.

The same parallel lines can be observed in both plots of Figure 25, the scatter plots for the ETS. In these plots additional vertical lines of points can be noticed. Those lines are neither present in the scatter plots of the FBI nor in the ones of the DAS. Therefore, the interval of the x-axis is taken into consideration: in Figure 24 (FBI) the x-axis displays the interval from 0.001 to 100 with most of the mean values being higher than 0.1. Most of the mean values of the DAS (Figure 26) lie between 0.6 and 1.2 while the x-axis displays the interval from 0.3 to 1.5. The interval of the x-axis in the ETS case (Figure 25) ranges from 0.001 to 0.4 which is the same lower bound as in the FBI case. But the ETS has a tendency to lower mean values in comparison to the FBI. Most of them exhibit values between 0.01 and 0.3. Since the accuracy for the calculations of each quality measure was two decimal places, and since for certain points in time not all BC groups were available, it is likely that especially averages over the PHY groups obtain discrete values of 0.01, 0.02,... 0.1. This becomes apparent above all in plots with logarithmic axes. There were no points in time when only members of one certain PHY group were available, i.e. five members always contribute to the averages over the BC groups. These considerations are confirmed by the fact that coloured points in particular, i.e. averages over the PHY groups, determine the vertical lines.

The ETS in Figure 25a shows the same behaviour than the FBI: lower spread within the BC members and higher spread within the PHY members. So the whole EPS is rather controlled by the lateral boundary conditions. However, the distinction between the groups cannot be made as clearly as for the FBI. Figure 25b displays the stratification by the convective time scale. Scatter points during the forced-frontal regime ($\tau_c$ lower than 6h) exhibit higher means and lower spreads than scatter points during the triggered regime ($\tau_c$ higher than 6h). The average values of all points of the different regimes are distinguishable fairly well: the mean ETS is about 0.082 in the forced-frontal regime and 0.026 in the local-forced regime. The spread values also exhibit a difference of about

factor 2: ca. 0.43 in the equilibrium regime and 0.81 in the non-equilibrium regime (see Table 4).

The scatter plot of the DAS (Figure 26) does not contain the diagonal lines that were observed in the other two plots. This may be due to the higher mean values within the DAS groups in general. Like the other two scores, the DAS is characterised by higher spread values within the PHY groups and lower spread values within the BC groups. However, there are also some points of the PHY groups with very low spread values and some points of the BC groups with high spreads.

But Figure 26b does not allow a clear distinction between the equilibrium and the non-equilibrium regime. The scatter points during periods with forced-frontal convection are distributed more broadly than the scatter points during periods with triggered convection. However, this may also be owed to the higher number of points which are assigned to the forced-frontal regime. The averaged mean values and relative spread values over all points of both regimes are approximately 0.84 and 0.05 in the equilibrium regime, and about 0.83 and 0.06 in the non-equilibrium regime. These values are very similar. Therefore, one can assume that the DAS allows the evaluation of an EPS which is independent from the regime.

Scatter plots of the convective time scale on the x-axis versus the relative spread on the y-axis are presented in Figures 27 and 28. Figures 27a and 28a depict all the scatter points. Figures 27b and 28b show daily averages of all the different groups. The connection between the two plots of each parameter is evident. All four graphs show lower spread values of the BC groups and higher relative spreads of the PHY groups.

Since it is possible to recognise a linear relation between $\tau_c$ and the relative spread, correlation coefficients of the daily-averaged data have been calculated. These coefficients have been computed for the BC groups, the PHY groups and for all groups together (cp. Table 5). FBI and DAS exhibit their highest correlation coefficients of over 0.4 for the PHY group. The correlation coefficient between the two variables is lower for the BC groups and for all members. The latter is not surprising since the correlation coefficient shows a tendency to lower values if more data is processed. All values from Table 5 are significant at 99.9% confidence except the ETS correlation coefficients for all members and for the PHY groups.

| | FBI | ETS | DAS |
|---|---|---|---|
| All members | **0.32** | 0.12 | **0.26** |
| BC groups | **0.28** | **0.50** | **0.35** |
| PHY groups | **0.42** | 0.19 | **0.43** |

**Table 5:** DE region correlation coefficients between $\tau_c$ and the relative spread for FBI, ETS and DAS. The correlation coefficients have been calculated for the BC groups, the PHY groups and for all members. Bold values are significant at 99.9% confidence.

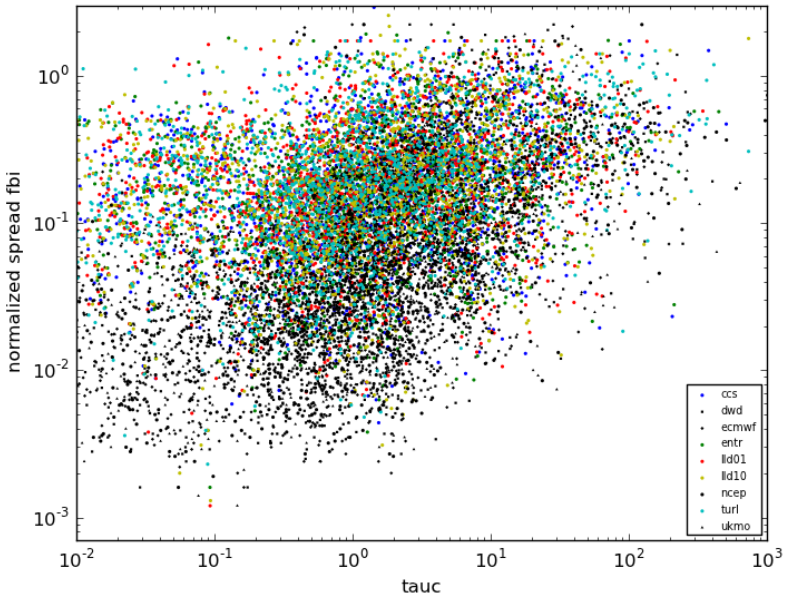


**(a)** FBI - all points in time

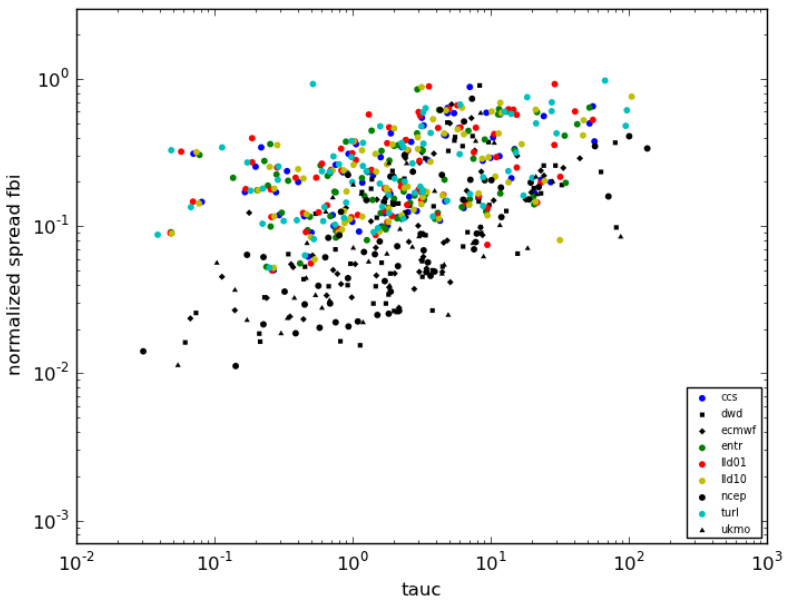


**(b)** FBI - daily averages

**Figure 27:** The convective time scale on the x-axis versus the relative spread of the FBI on the y-axis for the DE region, legend as in Figure 9b.

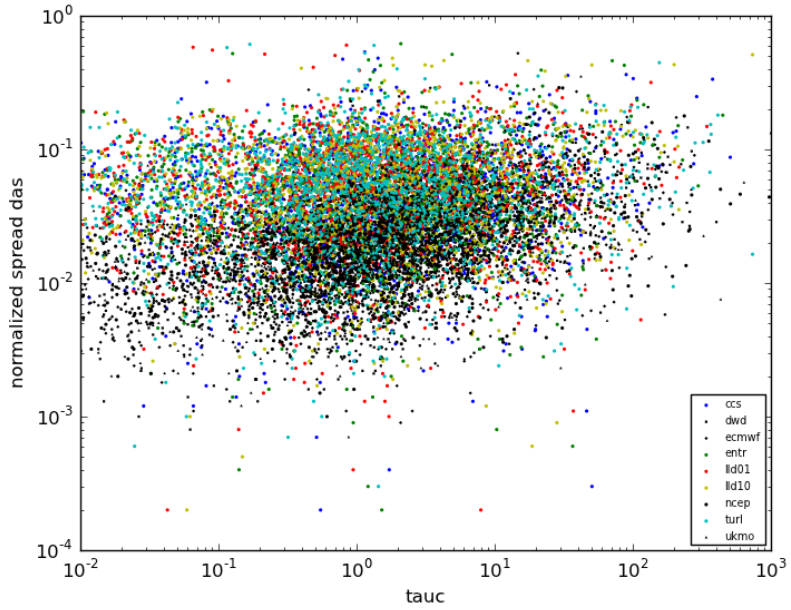


**(a)** DAS - all points in time

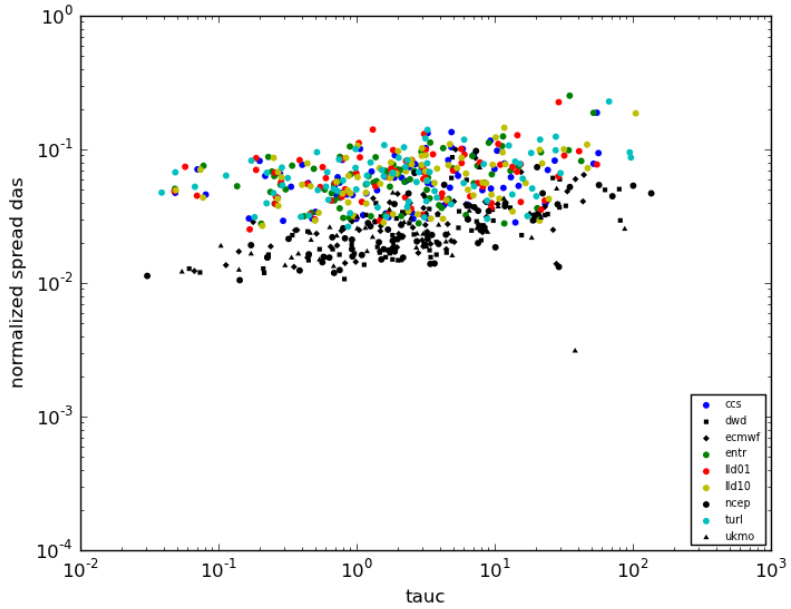


**(b)** DAS - daily averages

**Figure 28:** The convective time scale on the x-axis versus the relative spread of the DAS on the y-axis for the DE region, legend as in Figure 9b.

## 4.4 Sensitivities

### 4.4.1 Sensitivity of the model area: Analysis of the COPS region data

#### Forced-frontal convection

In Figure 29 time series of the total precipitation, CAPE and $\tau_c$ of four days during the forced-frontal regime, averaged over the COPS domain in southwest Germany, are shown. This regime is characterised by low CAPE values in combination with precipitation during all of the days. $\tau_c$ is low for most points in time. On 22 July the threshold value of 6h is exceeded due to the absence of precipitation in the afternoon while the CAPE is rising. The standard deviations of precipitation are high, while the standard deviations of the convective time scale are low.

Hence, the convective time scale can also be used in a smaller region to determine the equilibrirum regime. However, there are some differences between the time series of the DE region (Figure 12) and the time series of the COPS region (Figure 29). All the lines appear smoother in the DE region when compared to the COPS region: there are more precipitation maxima in the COPS region which sometimes are even significantly higher than in the DE region. The higher standard deviations of precipitation within the COPS region propagate to higher standard deviations of the convective time scale. The lower standard deviations of precipitation within the DE region are responsible for the lower standard deviations of $\tau_c$. These findings are basically due to precipitation features in the larger domain being present longer than in the smaller domain. A front can serve as an example: a cold front which moves at a speed of $50\frac{km}{h}$ from west to east would influence the COPS region for approximately 4h. But the whole model area would be influenced by this front for more than twice as long. The lower smoothness and the higher standard deviations within the COPS data can also be explained with

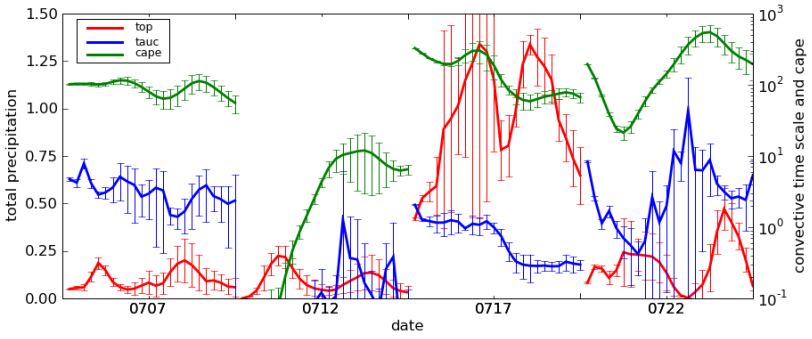


**Figure 29:** As Figure 7, but for the COPS region on four days (07, 12, 17, 22 July 2009) during the forced-frontal regime.

the occuring and dissapearing of precipitation features at different points in time for different model members.

Figure 30a displays the time series of the DAS. Its minimum value and its maximum value are slightly higher than 0.3 and 1.2 respectively. The BC groups (lines of the same colour) behaving similarly is a characteristic of this time series on 12, 17 and 22 July. On 07 July the BC groups exhibit the same behaviour if members 1, 6, 11 and 16 were excluded. Between 09 and 18 UTC these members exhibit lower DAS values than the rest of the other lines. As in in the DE region the DAS reveals its lowest values in the

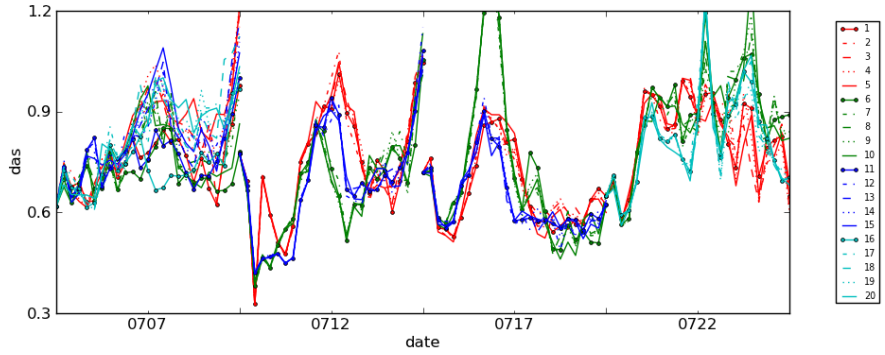


**(a)** Time series of the DAS.

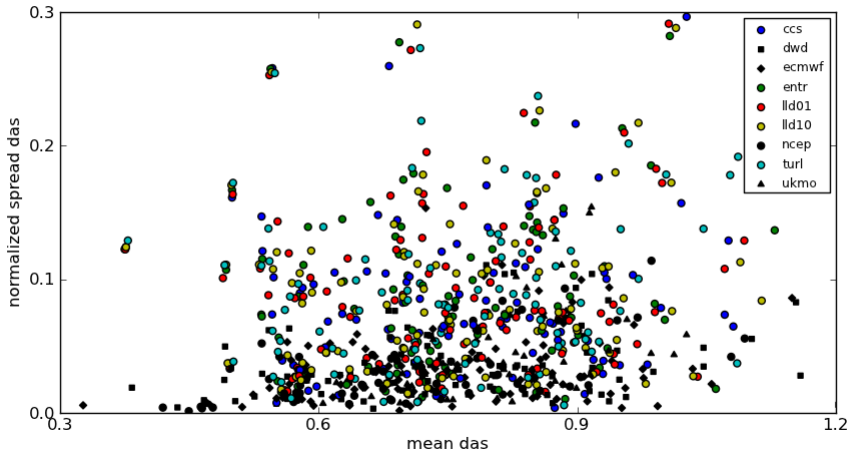


**(b)** Spread-skill relationship of the DAS.

**Figure 30:** As in Figure 9 but for the displacement and amplitude score of four days (07, 12, 17, 22 July 2009) during the forced-frontal regime in the COPS region. Time series of each day separately can be found in the appendix: Figures A11 and A12.

beginning of each day and increases with longer lead times: since initial conditions are not perturbed in the COSMO-DE-EPS all members are likely to behave similarly for short lead times. Another reason is the lower amount of precipitation at nighttime, i.e. during the first model hours, which leads to significantly lower DAS values. By contrast, FBI and ETS do not necessarily exhibit a higher forecast quality for short lead times.

Stamp maps of precipitation (members 1 - 15 and observation) at 12 July 03 UTC are depicted in Figure 31. This observation is characterised by the remnant of a front entering the COPS region. In general, the similarities within each BC group is striking. There are almost no differences at all within those groups. By contrast, the different members of the PHY groups deviate from each other a lot. Members 1 - 5 miss the front completely and forecast only some small precipitation features. Hence, the DAS of these members is highest, compared to members 6 - 15. Both BC groups (DWD and NCEP boundary conditions) are - as in the observation - characterised by an entrance of the front into the COPS region. Not all precipitation features are located correctly: some false alarms can be found as well as some misses. Additionally, the forecast precipitation

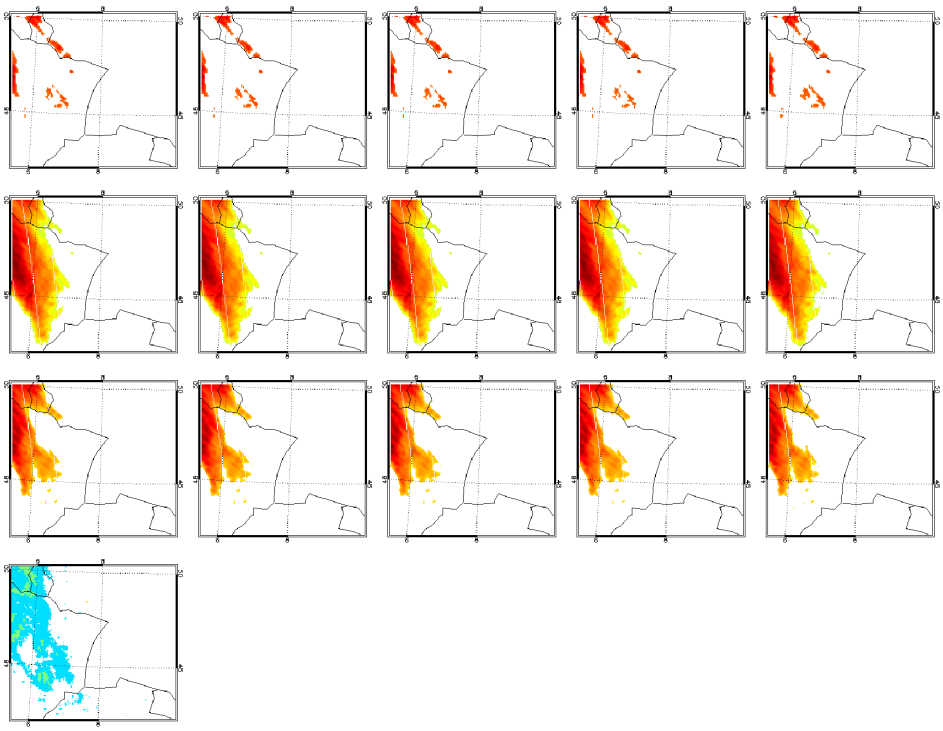

**Figure 31:** Stamp maps of the COPS region displaying forecast synthetic radar imagery on a forced-frontal day: 12 July 2009 - 03 UTC, members 1 - 15. The map in the fourth row displays the radar observation. Radar reflectivities 7, 19, 28, 37, 46 and 55 dBZ are colour-coded.

exhibits significantly higher values than the observation. This leads to an RMS error which contributes to the DAS. Members 6 - 15 exhibit DAS values of about 0.4 which is very low. Thus, the forecast of members 6 - 15 at this point in time is fairly promising.

The behaviour of the statistical scores is generally different in the two regions. But analysing the DAS, the similar behaviour of the BC groups can be observed in the DE region (Figure 13c) and in the COPS region (Figure 30a). At some points in time the values of the DAS are lower in the DE region. At other points in time they are lower in the COPS region (note the different scales of the y-axes here). However, a definitive conclusion whether one region favours better DAS values cannot be made during the period analysed.

The COPS scatter plot of the DAS (Figure 30b) is in general comparable to the referring scatter plot for the DE region (Figure 14c). Both plots exhibit lower spread values of the BC groups and higher spread values of the PHY groups, which is typical for the forced-frontal regime. Nevertheless, going into details, some differences can be noted. The minimum of the COPS means is slightly lower than the minimum of the DE means. More mean values below 0.6 and less mean values over 0.9 can be observed in this smaller region. But the plot of the COPS region also depicts higher relative spreads (up to 0.3) than the plot of the DE region (up to 0.18).

Due to the smaller amount of grid points in the COPS region the FBI and ETS datasets (not shown) exhibit more oscillations than in the DE region. These two verification measures also reveal lower forecast quality and higher relative spreads. Like in the DE region, the BC groups exhibit lower relative spread values than the PHY groups. The ETS is characterised by more negative values in the COPS region when compared to the DE region.

### Local-forced convection

The time series in Figure 32 are characterised by high CAPE values with daily maxima in the convective period. Most of the precipitation was also forecast in the convective period. An exception is 03 July: on this day there are two maxima of precipitation, one with a small amount of precipitation at 08 UTC and one with a very high amount of precipitation at 15 UTC.

These findings are reflected in the convective time scale. The values of $\tau_c$ are generally high due to the high values of CAPE and the low values of precipitation. Hence, this period can be assigned to the non-equilibrium regime. Only on 03 July the values of the convective time scale are lower than the threshold of 6h. This is above all a result of the high precipitation value. The graph is characterised by low standard deviations of precipitation and high standard deviations of $\tau_c$. The low standard deviations of precipitation can be explained with its generally low values. The high standard deviations of the convective timescale can be explicated with the small amount of precipitation: $\overline{P}$ is in the denominator in the calculation of $\tau_c$. Hence, only small differences between the values of $\overline{P}$ can lead to large differences between the values of $\tau_c$.

The convective time scale can also be used in a smaller region to identify the local-forced regimes. But there are some differences between the time series of the DE region (Figure 21) and the time series of the COPS region (Figure 32). The lack of smoothness of the lines displaying the COPS region data can also be observed during this regime: Assuming the model predicted some convective rain from 14 UTC till 16 UTC in the COPS region and from 13 UTC till 18 UTC in northeastern Germany, there would be a clear peak of precipitation around 15 UTC in the COPS region with sharp borders around this point in time. The result for the DE domain would not exhibit such sharp borders, but probably also show maximal precipitation around 15 UTC due to the addition of the precipitation from the two different areas.

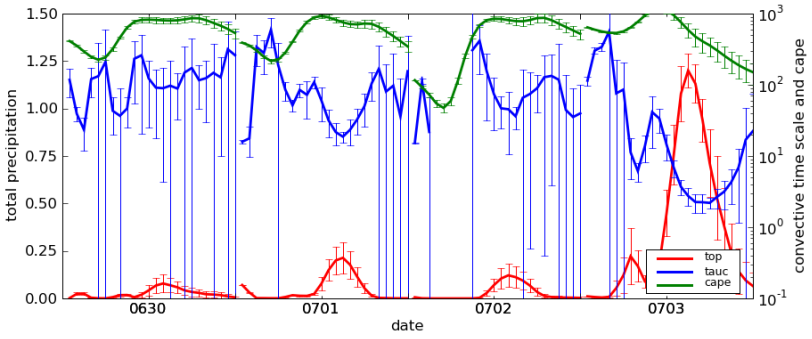


**Figure 32:** As Figure 7, but for the COPS region on four days (from 30 June to 03 July 2009) during the local-forced regime.

In this period the time scale of convective adjustment is significantly higher within the COPS region than it is within the DE region. Hence, the COPS region is very sensitive to local forcing due to its complex terrain with its two low mountain ranges. Especially in the period from 30 June to 03 July the COPS region was more influenced by this local forcing than the whole model area was.

The time series of the FBI from 30 June till 03 July (Figure 33a) is characterised by large amplitudes for the whole period: either the model underestimates or overestimates precipitation. Values around 1 are rare. However, lines with the same style (PHY groups) have similar values during the convective period of each day. The differences within each BC group (same line colour) are higher. Likewise the ETS from 30 June till 03 July (Figure 34a) shows the similarity of the PHY groups, however not as evidently as the FBI does. The distinction can be made most clearly in the convective period from 01 July to 03 July where members 5, 10, 15 and 20 (varied asymptotic mixing length of turbulent scheme) show the poorest values. The ETS ranges between -0.02 and 0.16.

Stamp maps of all available members with precipitation data from the COPS region at 03 July 15 UTC are presented in Figure 35. This point in time has been chosen since the model precipitation was highest during this local-forced period (cp. Figure 32). All members are characterised by very spotty precipitation features. The observation also shows spotty maxima of precipitation, but there are large areas with a small amount of precipitation as well. Thus, not all available members produce precipitation completely correctly, in particular members 10, 15 and 20 . They exhibit a similar structure and the smallest number of precipitation features. This also manifests by lower values of the FBI and the ETS in the time series. Members 11 - 20 miss large areas of strong precipitation over the Vosges mountains, Rhineland-Palatinate and Saarland. These members also incorrectly locate the precipitation features over Northern Switzerland to the west of Lake Constance. These features are to be located further in the west. In this area members 7 - 10 localise the precipitation features more correctly. Member 6 predicts precipitation further eastward, but not as far away as members 11 - 20. In general, all members slightly underestimate precipitation. This is reflected in the FBI being lower than 1 and in the ETS obtaining low values compared to a forced-frontal day. However, precipitation is not forecast too poorly at this point in time. Therefore, the ETS values exhibit almost the highest values on 03 July at 15 UTC compared to the rest of this four-day period.

The behaviour of the statistical scores differs in the two regions: the FBI in the COPS region oscillates more than it does in the DE region (cp. Figures 22a and 33a). The general structure is the same in both regions, but minima and maxima are more distinctive in the COPS region. The FBI in the DE region is closer to 1. Hence, the forecast for the whole model area performs better in the non-equilibrium regime if the FBI is taken into consideration. The ETS time series of the COPS region (34a) and of the DE region (22b) behave similarly in the convective periods concerning the importance of the PHY groups. However, the ETS values in the DE region are higher on 30 June

and 02 July and lower on 01 and 03 July, when compared to the COPS region (in the DE region the y-axis extends from 0 to 0.06 while it extends from -0.02 to 0.15 in the COPS region).

The referring scatter plots of Figures 33 and 34 confirm the impressions from the time series: the mean values of the FBI (Figure 33a) in the convective period constitute values between 0 and slightly more than 0.6. The relative spread is lower within the PHY groups and higher within the BC groups. The group of members with varied turbulent length scale (members 5, 10, 15, 20) stands out, since it exhibits lower means than all

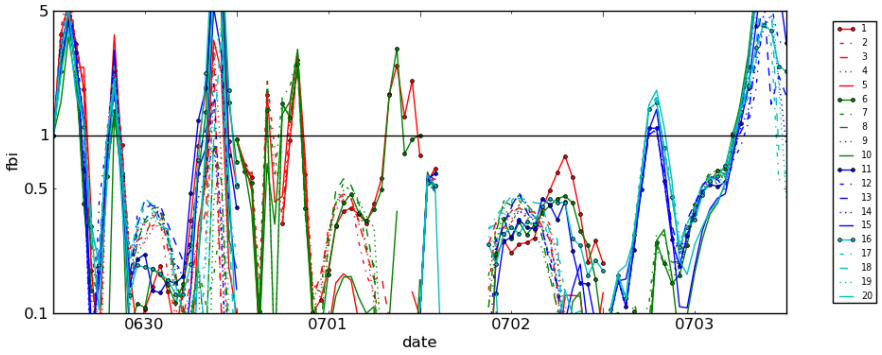


**(a)** Time series of the FBI.

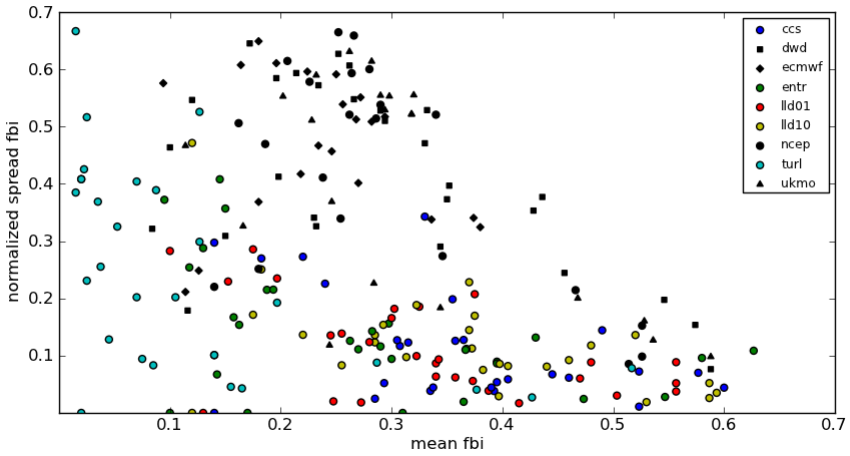


**(b)** Spread-skill relationship of the FBI (values from 10 UTC to 17 UTC only).

**Figure 33:** As Figure 9 but for the frequency bias of four days (from 30 June to 03 July 2009) during the local-forced regime. Time series of each day separately can be found in the appendix: Figures A7 and A8.

other groups. It also exhibits a higher variation of the spread values compared to the other PHY groups. The main discrepancy between the plot for the COPS region and for the DE region (Figure 23a) are the different mean and spread values: most of the mean values in the COPS region lie between 0.1 and 0.4 with minimum values only slightly over 0. By contrast, most of the mean values in the DE region are found between 0.4 and 0.6 with minimum values slightly under 0.2. The relative spread peaks at 0.7 in the COPS region and at 0.4 in the DE region. Hence, not only the forecast quality is

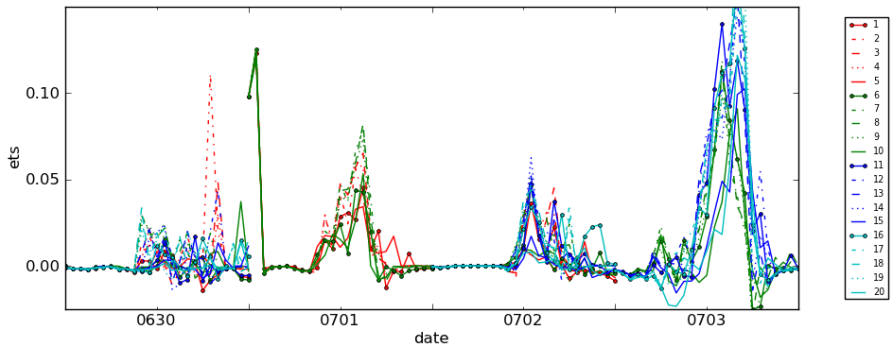


**(a)** Time series of the ETS.

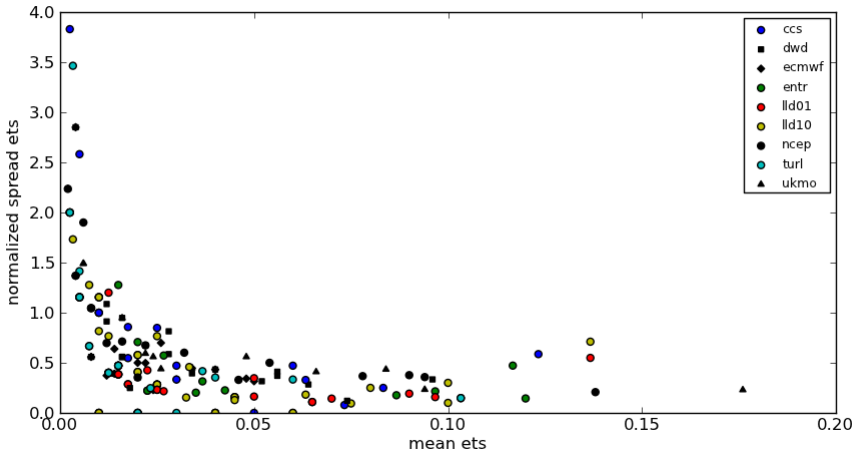


**(b)** Spread-skill relationship of the ETS (values from 10 UTC to 17 UTC only).

**Figure 34:** As Figure 9 but for the equitable threat score of four days (from 30 June to 03 July 2009) during the local-forced regime. Time series of each day separately can be found in the appendix: Figures A9 and A10.

superior for the DE region case, but the spread within all groups, i.e. also within all members, is also lower than it is for the COPS region.

The ETS scatter plot (Figure 34b) is characterised by the majority of the means between 0 and 0.1. Like in the DE region (Figure 23b) lower mean values indicate rising spread values. Hence, the whole plot can be compared to a hyperbolic function. In the COPS region more data could be plotted, especially more data with low mean values. However, there are some group means of the COPS region exceeding those from the DE region. Most of the spread values are situated between 0 and 0.5 in both graphs, but the COPS graph tends to higher relative spread values (up to almost 4) than the DE graph (up to 1.2). However, the most striking difference is that the PHY groups (lower spread values) and the BC groups (higher spread values) can be separated in the COPS region plot. This separation was not possible in the plot of the DE region. Thus, the ETS shows some sensitivity for the perturbations of the model physics in the non-equilibrium regime when the smaller COPS region is analysed.

The DAS data (not shown) behaves similarly in both regions. During the convective period members 5, 10, 15 and 20 exhibit the highest DAS values in both regions. In the COPS region the DAS values generally oscillate more than in the DE region. This

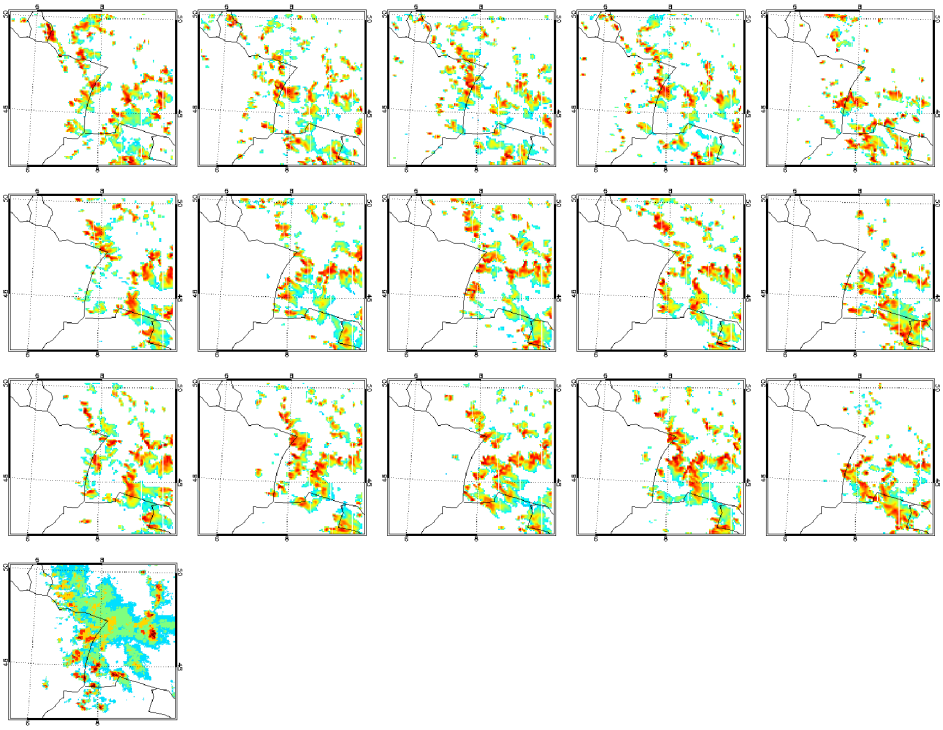

**Figure 35:** As Figure 31, but for 03 July 2009 - 15 UTC, members 6 - 20 and radar observation.

can also be identified within the group averaged data: the DE region is characterised by lower relative spread values.

Hence, in the smaller COPS region on these analysed days all three verification measures have a tendency to higher relative spread values within the groups. The time series show less smoothness than they do in the DE region, regardless of the regime. A reason for this is in the statistics: a smaller region deals with less grid points. In this study, this is equivalent to a much smaller analysed dataset. The variability between the different members of a smaller dataset is generally higher than it is when a larger dataset contributes to the evaluation of the members. This is because differences tend to average out in a larger dataset.

### Scatter plots with data of the entire period

In the spread-skill relationship of the FBI displaying the different groups of members (Figure 36) the BC groups tend to lower spreads and higher means than the PHY groups, just like in the plot for the DE region (Figure 24a). However, this separation cannot be observed as clearly as in the plot for the DE region. The COPS region plot shows a broader distribution of scatter points. It is also characterised by generally slightly higher spreads and lower means than the referring DE region plot.

These statements are valid in a similar manner for the respective ETS datasets. The data of the DAS, by contrast, hardly allows a separation of the groups. Instead a larger variability of the means and spreads can be found for the COPS region. In general, the data tends to lower (i.e. better) mean values, but higher spread values in comparison with the DE region.

In Figure 37 displays scatter plots of the ETS and DAS separated by the time scale of convective adjustment. In Table 6 the referring regime-averaged spread and mean values of FBI, ETS and DAS are presented. The ETS (Figure 37a) allows a clear separation between the two regimes: the equilibrium regime (blue circles) is characterised by higher spread values and lower mean values than the non-equilibrium regime (red squares) is.

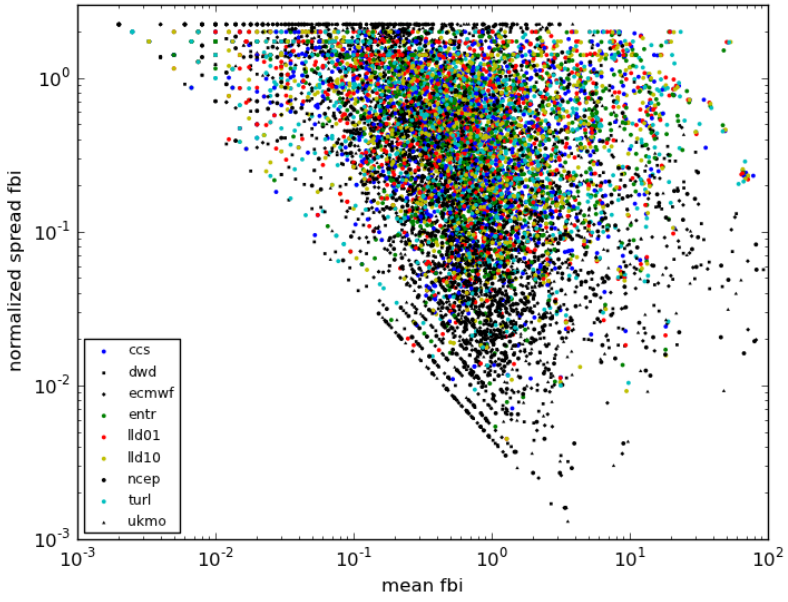


**Figure 36:** Scatter plot of the FBI for the COPS region with values from all available days and members. Both axes are logarithmic, legend as in Figure 9b.

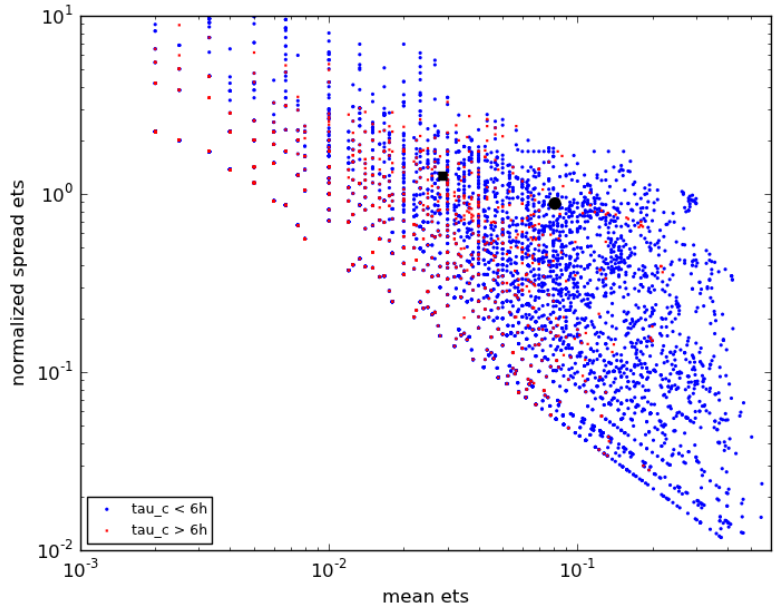


**(a)** ETS

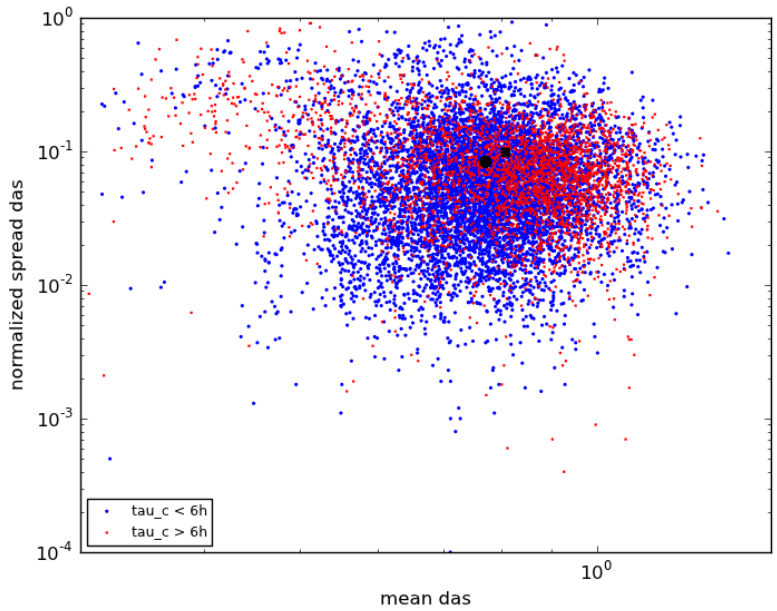


**(b)** DAS

**Figure 37:** As Figure 24b, but for the ETS and DAS in the COPS region.

| | FBI | ETS | DAS |
|---|---|---|---|
| mean frontal | 2.5277 | 0.0811 | 0.7711 |
| spread frontal | 0.4093 | 0.8832 | 0.0836 |
| mean local | 0.8546 | 0.0287 | 0.8084 |
| spread local | 0.6467 | 1.2586 | 0.0986 |

**Table 6:** Averages over the means and over the spreads of FBI, ETS and DAS for the COPS region, separated by the local-forced and the forced-frontal regime.

The averages of the mean values of the two regimes are 0.081 and 0.029. This means the average value of the equilibrium regime is three times higher than the average of the non-quilibirium regime. The referring spread values differ with a factor of about 1.5. In comparison to the values of the DE region the averaged means do not exhibit significant differences: the average of the forced-frontal means is slightly lower in the COPS region. The average of the local-forced means is slightly higher. Differences can be observed in particular within the spread values: the averaged spread during the equilibrium regime is twice as high in the COPS region. The averaged spread of the non-equilibrium regime is 50% higher in the COPS region.

As mentioned before, the DAS in the COPS region exhibits lower means and higher spreads than in the DE region (cp. Figures 37b and 26b). The scatter plot permits a separation between the two regimes. The majority of the red scatter points ($\tau_c$ higher than 6h) tends towards higher mean values than the majority of the blue scatter points ($\tau_c$ lower than 6h). This is confirmed by the black circle and square in Figure 37b and by the values of Table 6. The average of the mean values of the forced-frontal regime amounts to 0.77. It is slightly lower than the average of the mean values of the triggered regime which attains ca. 0.81. The spread averages exhibit a slightly more percentaged difference of about 20%: a forced-frontal averaged spread of 0.084 compared to a local-forced averaged spread of 0.099. In comparison to the DE region, the COPS region is characterised by slightly lower values of the regime-averaged means. The COPS region also exhibits values of the averaged spread that are twice as high.

Figures 38 and 39 consist of scatter plots of the convective time scale on the x-axis versus relative spread on the y-axis. Scatter plots of the FBI are shown in Figure 38a (all points in time) and 38b (daily averages). Both graphs are characterised by lower spread values of the BC groups and higher spread values of the PHY groups. But the separation is more evident in the DE region (Figure 27) which shows lower spread values than the referring COPS plots do. Figures 39a and 39b are also characterised by high spread values of the PHY groups and low spread values of the BC groups. The relative spread is relevantly higher in the COPS region. If regression lines were fitted in, the plots of the DE regions would exhibit increasing lines while some plots of the COPS region would then obtain decreasing regression lines, others increasing lines.

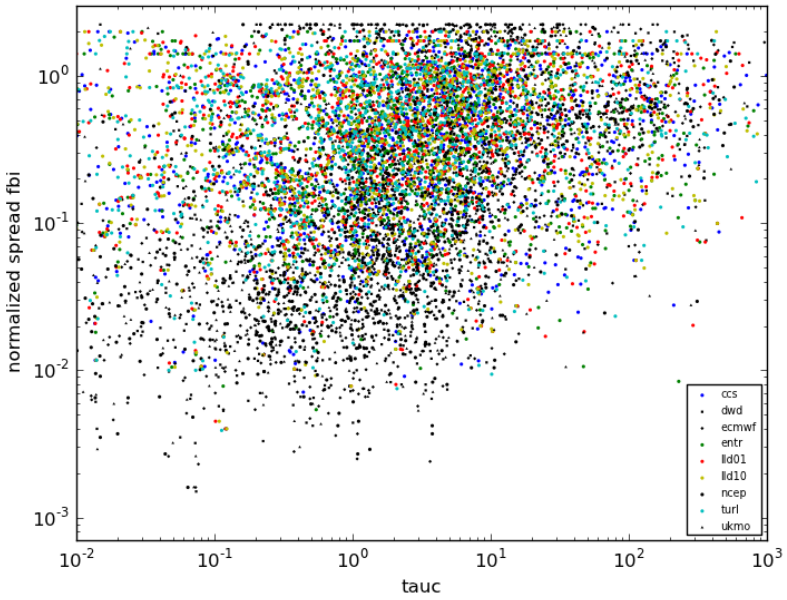


**(a)** FBI - all points in time

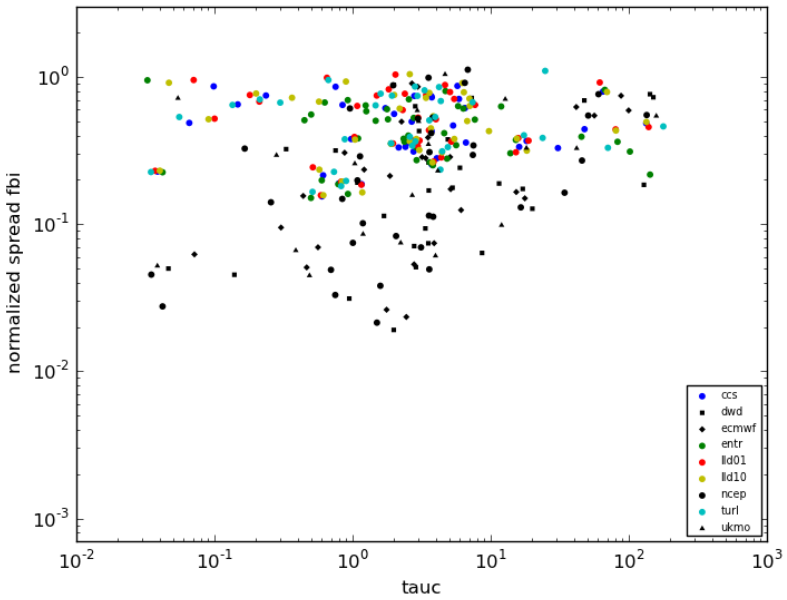


**(b)** FBI - daily averages

**Figure 38:** The convective time scale on the x-axis versus the relative spread of the FBI on the y-axis for the COPS region, legend as in Figure 9b.

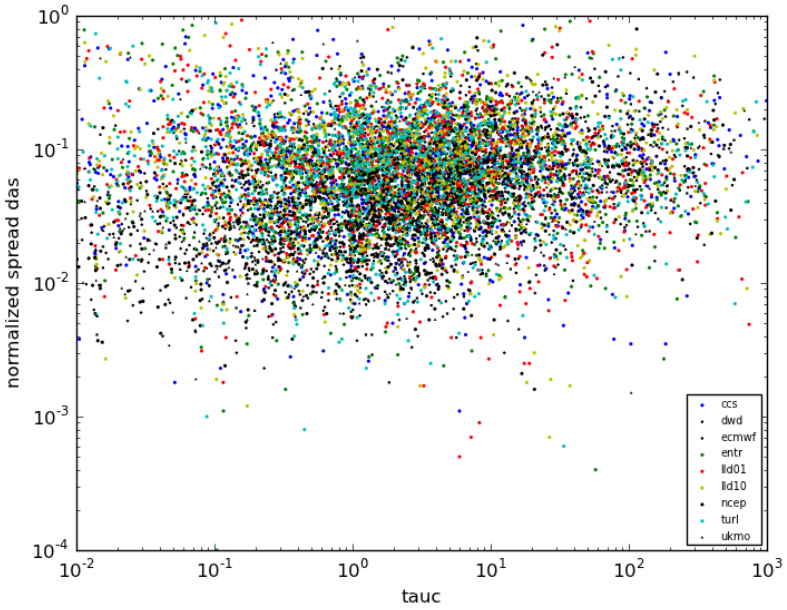


**(a)** DAS - all points in time

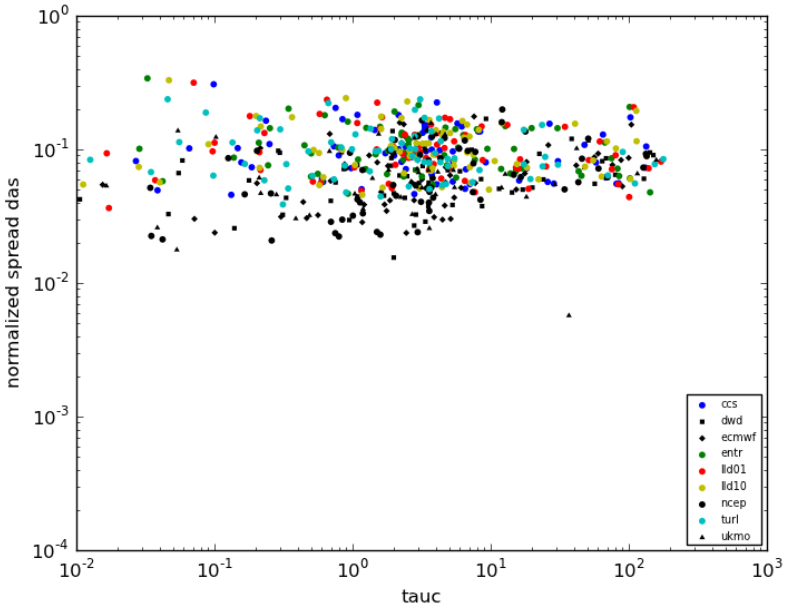


**(b)** DAS - daily averages

**Figure 39:** The convective time scale on the x-axis versus the relative spread of the DAS on the y-axis for the COPS region, legend as in Figure 9b.

| | FBI | ETS | DAS |
|---|---|---|---|
| All members | 0.100 | 0.317 | -0.015 |
| BC groups | **0.324** | 0.135 | **0.152** |
| PHY groups | -0.036 | 0.301 | -0.010 |

**Table 7:** COPS region correlation coefficients between $\tau_c$ and the relative spread for FBI, ETS and DAS. The correlation coefficients have been calculated for the BC groups, the PHY groups and for all members. Bold values exhibit significance of at least 95% confidence.

A connection between the displayed parameters, like in the DE region, is recognisable. Hence, correlation coefficients between daily-averaged $\tau_c$ and the three analysed scores have been calculated (cp. Table 7). The BC group of the FBI exhibits a correlation coefficient with $\tau_c$ of 0.32, while the BC group of the DAS obtains a correlation coefficient of 0.15. The FBI and DAS correlation coefficient are significant at 99.9% and 95% confidence, respectively. All other correlation coefficients in Table 7 are not significant at a confidence level of 95 %. Surprisingly the correlation coefficients of the ETS do not satisfy the confidence requirements. This is due to the small amount of contributing values: the relative spread value of the ETS is frequently infinity which propagates to the daily averages.

### 4.4.2 Sensitivity of the threshold value to compute the convective time scale

Some sensitivity tests were implemented in order to examine in detail if the threshold of $\overline{P} = 1\frac{mm}{h}$ is a reasonable value to compute $\tau_c$. The concept of a lower threshold was especially taken into consideration since the convective time scale could not be computed for every given point in time if the threshold value of $\overline{P} = 1\frac{mm}{h}$ was used: if no grid points with $\overline{P} > 1\frac{mm}{h}$ are found, then the area-averaged $\tau_c$ goes towards infinity (singularity problem).

Figure 40 displays time series of precipitation, CAPE and $\tau_c$ on 07 July 2009 (COPS region) averaged over the ECMWF members. Since the precipitation and CAPE are averaged over all grid points regardless of the threshold value, these curves are the same in Figures 40a and 40b. The CAPE attains moderate values between 40 $\frac{J}{kg}$ and 100 $\frac{J}{kg}$. Precipitation can be found during the whole day. It exhibits two peaks: 0.18 $\frac{mm}{h}$ at 05 UTC and 0.15 $\frac{mm}{h}$ at 17 UTC. The convective time scale in Figure 40a (threshold value of $1\frac{mm}{h}$) shows some oscillations and ranges between 1h and 6h.

In Figure 40b (threshold value of $0.1\frac{mm}{h}$) $\tau_c$ oscillates as well and exhibits values from 3h up to 17h. The convective timescale is higher for all points in time than it is in Figure 40a. Hence, a separation by the threshold value of 6h would assign the majority of this day to the local-forced regime and not to the forced-frontal regime. The largest differences between the two graphs can be found around 10 UTC and at the end of the day. During this period precipitation was low. Thus, with a lower threshold of $\overline{P}$ a larger relative amount of grid points with low precipitation contributes to the calculations of $\tau_c$.

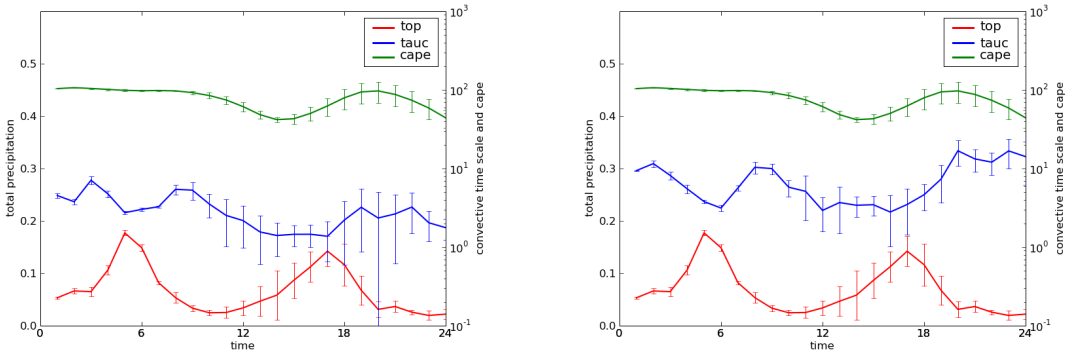


**(a)** COPS region ECMWF members with $\overline{P} > 1\frac{mm}{h}$

**(b)** COPS region ECMWF members with $\overline{P} > 0.1\frac{mm}{h}$

**Figure 40:** As Figure 7, but on 07 July and employing different threshold values of $\overline{P}$ to compute $\tau_c$.

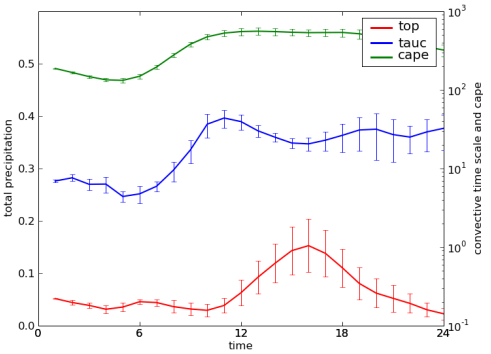


**(a)** DE region all members with $\overline{P} > 1 \frac{mm}{h}$

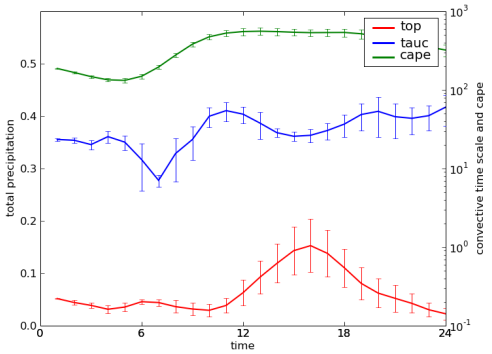


**(b)** DE region all members with $\overline{P} > 0.1 \frac{mm}{h}$

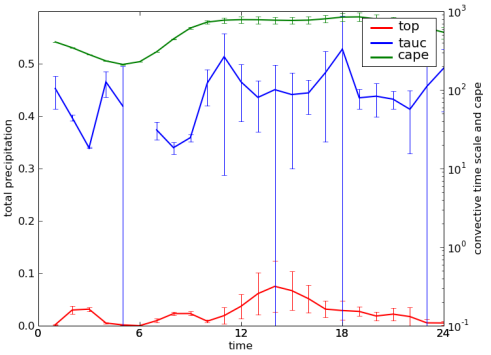


**(c)** COPS region ECMWF members with $\overline{P} > 1 \frac{mm}{h}$

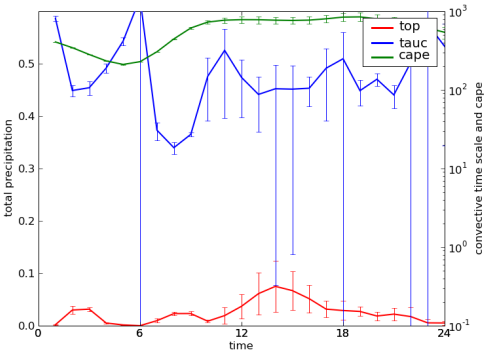


**(d)** COPS region ECMWF members with $\overline{P} > 0.1 \frac{mm}{h}$

**Figure 41:** As Figure 7, but on 30 June and employing different threshold values of $\overline{P}$ to compute $\tau_c$.

Some relative differences of the different results of $\tau_c$ ($\frac{\tau_{c,0.1} - \tau_{c,1}}{\tau_{c,1}}$) were also calculated. Hence, the impacts of the different threshold values become apparent. On 07 July the relative difference ranges between 0.04 and 9.28 in the COPS region. In the DE region the interval goes from 0.05 to 3.11. The lower difference in the DE region is due to the fact that the effect of a different threshold value depends on the size of the analysed region (as does the smoothness of the curves).

In Figure 41 examples from 30 June 2009 with different thresholds of $\overline{P}$ are presented: DE region with averages of all members (Figures 41a and 41b) and COPS region with averages of the ECMWF members (Figures 41c and 41d). The precipitation obtains values between 0.02 $\frac{mm}{h}$ and 0.15 $\frac{mm}{h}$ in the DE region. The CAPE varies between

$150\frac{J}{kg}$ and $400\frac{J}{kg}$. In the COPS region the precipitation peaks at 0.08 $\frac{mm}{h}$ and CAPE ranges between $200\frac{J}{kg}$ and $800\frac{J}{kg}$. None of the parameters demonstrate high standard deviations.

In Figure 41a $\tau_c$ ranges between 4.4h and 40h, in Figure 41b between 7h and 60h. In Figure 41c the values of $\tau_c$ lie between approximately 20h and 300h and in Figure 41d between 20h and over 1000h. However, on this day the classification with a threshold value of 6h mentioned in section 3.3.3 would be the same at most points in time. In the graphs of Figure 41 only two points in time would be classified differently: 05 UTC and 06 UTC of the DE region. In general, the convective time scale is higher, the lower the threshold value of $\overline{P}$.

The relative differences of this non-equilibrium day differ slightly from those of 07 July: in the COPS region the relative difference attains values of up to 40. In the DE region it is between 0.04 and 5. These higher values underline the effect of the threshold value of $\overline{P}$ during the triggered regime.

The singularity problem is noticeable at 06 UTC in Figure 41c where $\tau_c$ reaches infinity. By contrast in Figure 41d $\tau_c$ shows a continuous curve. Hence, a distinction between the two regimes could be made. But the value of over 1000h of $\tau_c$ at this point in time is a very high value. Since the singularity problem appeared infrequently, it is not implicitly necessary to change the threshold value of $\overline{P}$.

All the curves in the DE domain, especially the ones for precipitation and $\tau_c$, look smoother than those in the COPS region do. However, neither Figures 41a and 41b show significant differences concerning the smoothness in comparison to the average of the ECMWF members only, nor do Figures 41c and 41d compared to the average of all model members.

The smoothness of $\overline{P}$ depends on the size of the region (as previously discussed in section 4.4.1). This is not necessarily the case for $\tau_c$ where only grid points, at which $\overline{P}$ was over a certain threshold, were employed to calculate $\tau_c$. However, due to the larger amount of grid points in the DE domain, the precipitation value $\tau_c$ is calculated with is smoother. This propagates to $\tau_c$.

The larger the area analysed, the more likely to mix different precipitation features with each other. This is not a problem if the whole model area is dominated by the same form of convection (which is the case on most of the analysed days). But if the model area is dominated by different regimes, "intermediate values" of $\tau_c$ might be produced. This makes a classification more difficult

The standard deviations of $\tau_c$ (error bars) become higher in the smaller region. They also attain higher values when the lower threshold value of $\overline{P}$ is employed. If a lower threshold value of $\overline{P}$ was employed, then another threshold value of $\tau_c$ for the separation of the two regimes is to be considered (cp. different classification in Figure 40). The highly varying relative differences underline the different impacts of a lower threshold value of $\overline{P}$. These reasons favour the decision to keep the threshold of $\overline{P}$ at $1\frac{mm}{h}$.

# Chapter 5

# Summary and conclusions

A large dataset of the COSMO-DE-EPS with data from 104 days in the summer 2009 was analysed. The whole model area as well as the COPS subregion as an example for an area where orography and other boundary layer phenomena are important were examined. But before starting with the summary and final conclusions one should recall the two question which were posed in section 1: Can the time scale of convective adjustment be used to distinguish between frontal and local-forced convection? Are these different regimes rather governed by perturbations of the model physics or by lateral boundary conditions of different global models?

The time scale of convective adjustment which was calculated from model data was presented as a powerful method of classifying precipitation events. A threshold value of 6h was employed to distinguish between the equilibrium ($\tau_c$ lower than 6h) and the non-equilibrium ($\tau_c$ higher than 6h) regime. The examinations showed that this classification by means of the convective time scale is in agreement with an "eyeball" classification of the precipitation events on a large majority of the 104 days. The classification employing the time scale of convective adjustment failed in particular on days with very low amount of forecast rainfall while a traditional classification by a forecaster would suggest an assignment to the forced-frontal regime. A threshold value of 6h assigned 77% of points in time to the equilibrium regime. This is a significantly higher percentage than Zimmer et al. (2011) obtained: 55.8% for the period from May to October while the percentage for the summer months (June till August) amounts to 52.0%.

The model output was then compared to radar observations employing the traditional verification measures FBI and ETS as well as the recently developped DAS as a spatial method. Time series of one day and of several days were separately analysed for the two distinct meteorological regimes. All the statistical scores were characterised by a higher forecast quality during the forced-frontal regime. Spread-skill relationships showed that this regime reacts sensitively to the lateral boundary conditions, while the triggered regime was governed by the perturbations of the model physics during the convective period between 10 - 17 UTC.

Spread-skill relationships of all available data confirmed the general control of the model by the lateral boundary conditions. The separation employing a threshold value of $\tau_c$ lead to further findings: during the non-equilibrium regime group averages were

lower and spread values within the groups were higher than during the equilibrium regime. This was observed especially within the FBI and ETS dataset while the DAS did not allow a distinct separation. However, this generally confirmed the results of the detailed analysis of both typical 4-day periods.

These results could be obtained for the dataset of the COPS region and for the dataset of the whole model area, though the dataset of the COPS region was characterised by higher relative spreads and a slightly different forecast quality. The DAS and ETS within the COPS region exhibited a superior forecast quality than they did within the DE region due to the control of convection by local triggers like orography. The FBI had a tendency to produce a better forecast quality over the whole model area.

Scatter plots of the convective time scale versus the relative spread of the statistical scores demonstrated some significant correlations between the time scale of convective adjustment and each quality measure. Less correlations were noticed between $\tau_c$ and the ETS, and for the COPS region data sets. Most of the analysed data pairs of the DE region attained significance at a 99.9% confidence level.

WEUSTHOFF et al. (2011) employed data from the COSMO-DE-EPS and radar observations from the COPS campaign in August 2007. Their goal was was to identify the best members of a convection-permitting EPS. One of their approaches used the DAS to identify the ensemble members which are closest to the observations. As in in the investigations of WEUSTHOFF et al. this study revealed the lowest values of DAS for short lead times, while with increasing lead times the values of the DAS rose.

The scaling factor of the laminar sublayer was decreased (members 3, 8, 13, 18) and increased (members 4, 9, 14, 19) in the EPS employed by this thesis. But the time series of the FBI, ETS and DAS showed in general very low deviations between higher and lower scaling factor. Hence, the variation of the laminar sublayer has only a small effect. A decreased (increased) scaling factor did not essentially produce higher (lower) precipitation values. These findings were also shown by Figures 3 and 4 (case 1 - 8, i.e. Germany and Switzerland) of DIERER et al. (2009) who made sensitivity studies using the COSMO model in various regions of Europe. However, they showed that the variation of the scaling factor of the laminar sublayer becomes more important when precipitation features occur near the coastline.

Some results of this thesis are also in agreement with BALDAUF et al. (2011) who inter alia examined the role of the asymptotic mixing length of the turbulence scheme in the COSMO model: a lower value of the asymptotic mixing length led to superior forecast quality. In this study a higher perturbed value of this parameter was employed, and consequently these members attained the lowest forecast skill.

Although this analysis was based on an incomplete data set, this thesis coped with a huge data set and thus massively extended the analysis of KEIL and CRAIG (2011) whose results could be confirmed. Hence, this thesis is a further step towards the general validity of the convective adjustment time scale and the DAS.

The analysis of a dataset with all members available, the analysis of different regions, the analysis during other seasons and the employment of some other verification scores would be a suitable extension of this study. A separate analysis of displacement error (DIS) and amplitude error (AMP) of the DAS would provide further knowledge as well.

# Acknowledgements

First of all I would like to thank Deutscher Wetterdienst for providing the model data and the radar observations.

But of course, this thesis would not have been possible without the assistance of many people.

I owe my gratitude to my supervisor, Dr. Christian Keil, for his constant support whenever I needed assistance, for the many helpful discussions of my results and for the detailed revision to improve this thesis.

I would also like to thank Prof. Dr. Georg Craig for some good suggestions and questions during my progress report which helped me to make further progress.

I am also greatful to all of my friends for their support, in particular to Florian Schütz for helping me with some English expressions and for borrowing me his notebook when mine did not work, to Jörg Sawatzki for some tuition in Python coding and to Roxanne Phillips for carefully proofreading this thesis.

Furthermore I would like to thank my whole family, especially my parents Heidi and Hans Heinlein, my sister Daniela Heinlein and my grandmother Anna Heinlein, for constantly supporting me morally and also financially throughout my studies.

# Appendix: Additional graphs

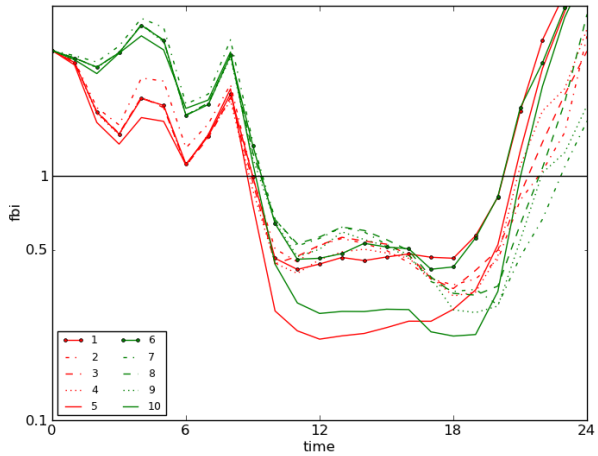


**(a)** FBI

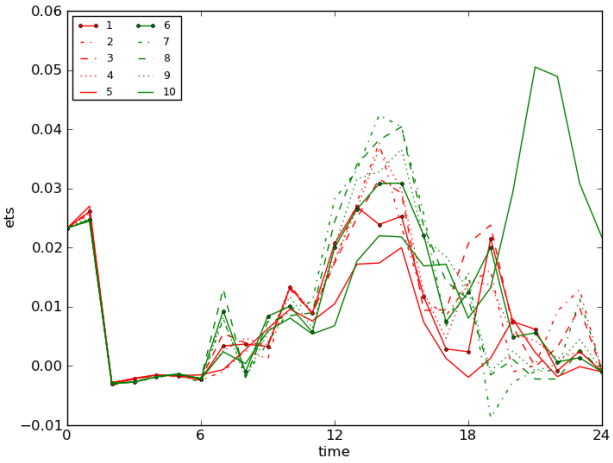


**(b)** ETS

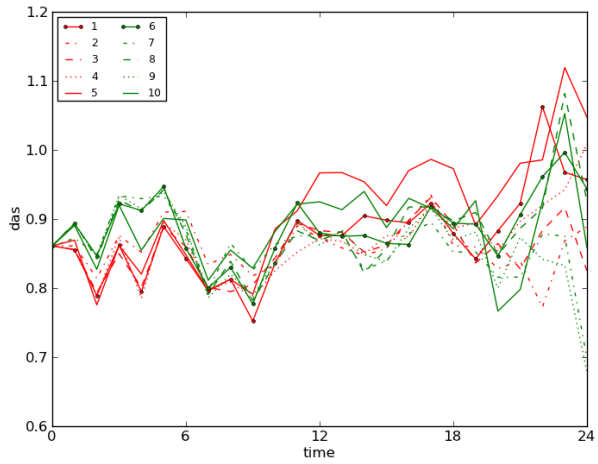


**(c)** DAS

**Figure A1:** Time series of FBI, ETS and DAS for the DE region on 01 July 2009, legend as in Figure 9a.

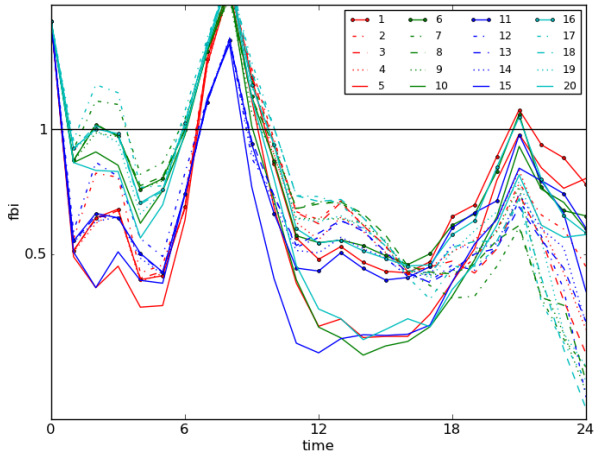


**(a)** FBI

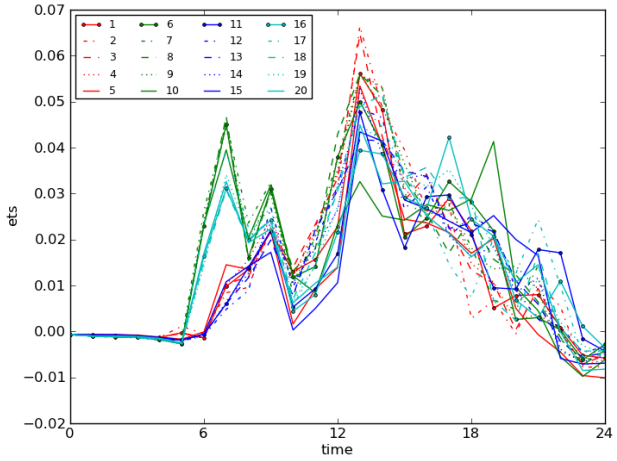


**(b)** ETS

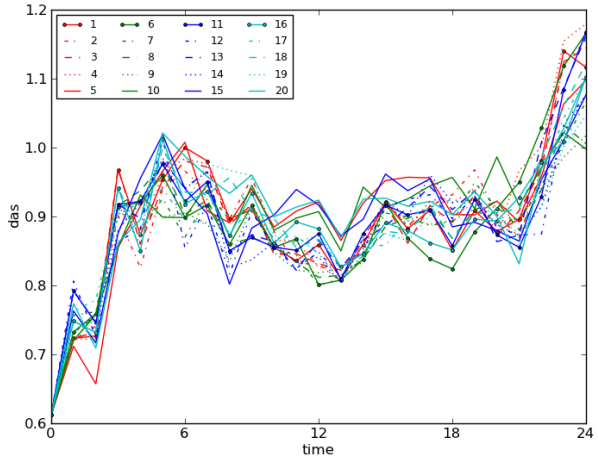


**(c)** DAS

**Figure A2:** Time series of FBI, ETS and DAS for the DE region on 02 July 2009, legend as in Figure 9a.

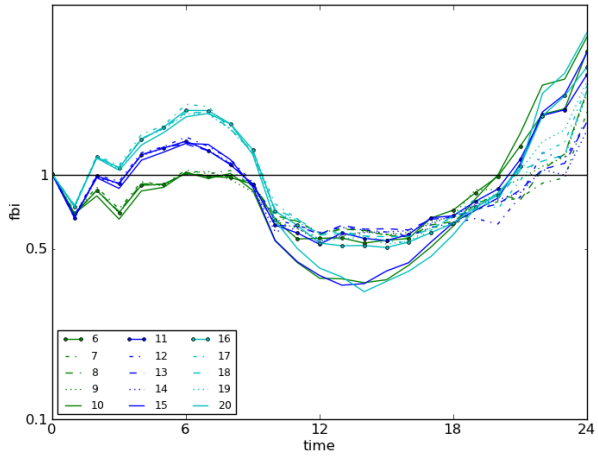


**(a)** FBI

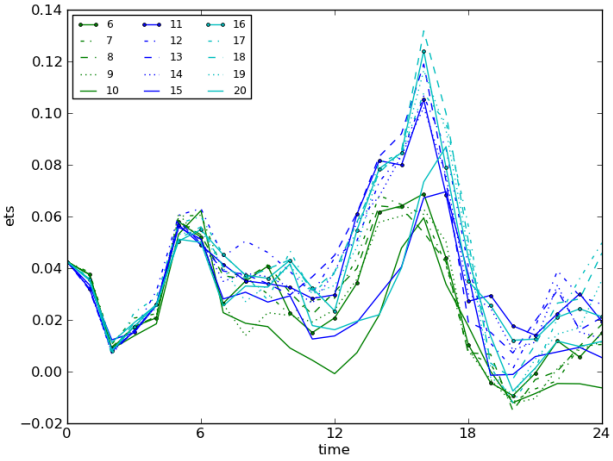


**(b)** ETS

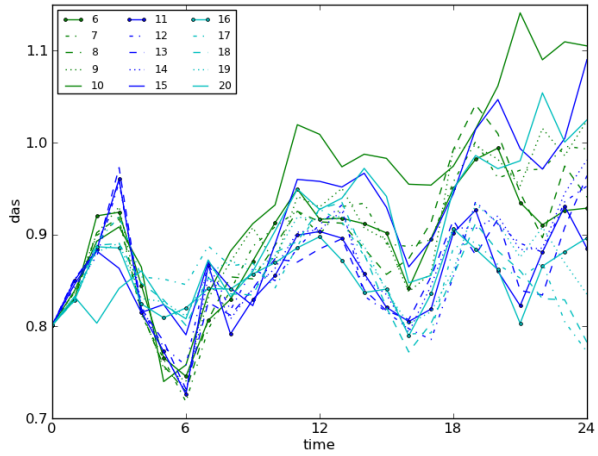


**(c)** DAS

**Figure A3:** Time series of FBI, ETS and DAS for the DE region on 03 July 2009, legend as in Figure 9a.

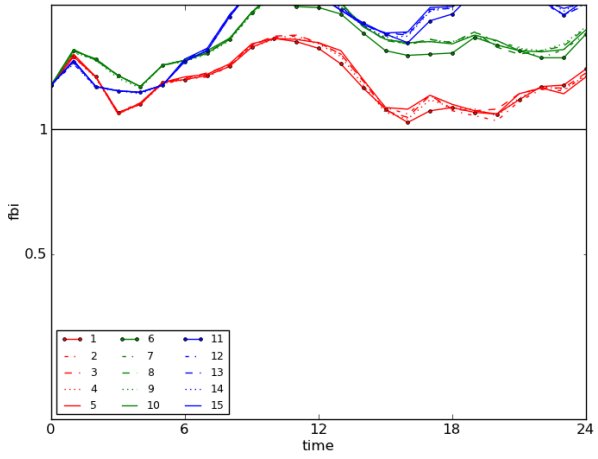


**(a)** FBI

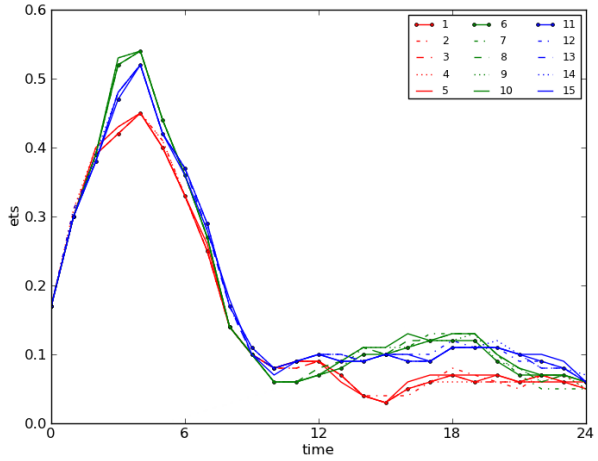


**(b)** ETS

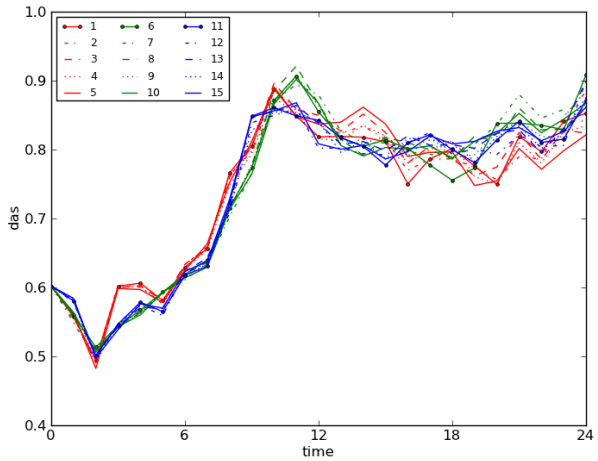


**(c)** DAS

**Figure A4:** Time series of FBI, ETS and DAS for the DE region on 12 July 2009, legend as in Figure 9a.

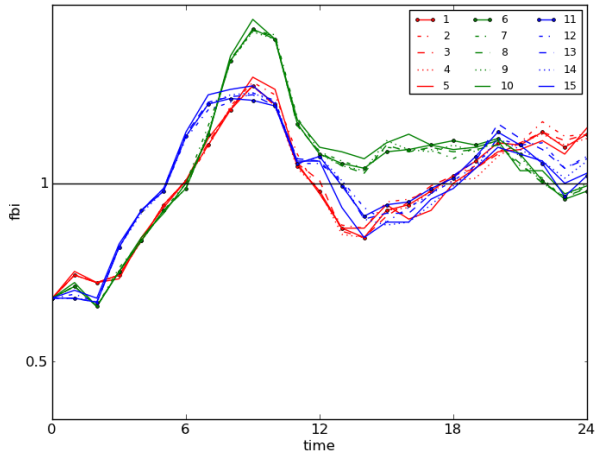


**(a)** FBI

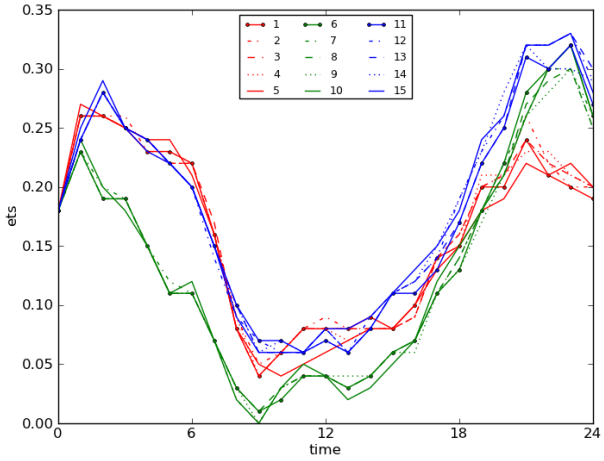


**(b)** ETS

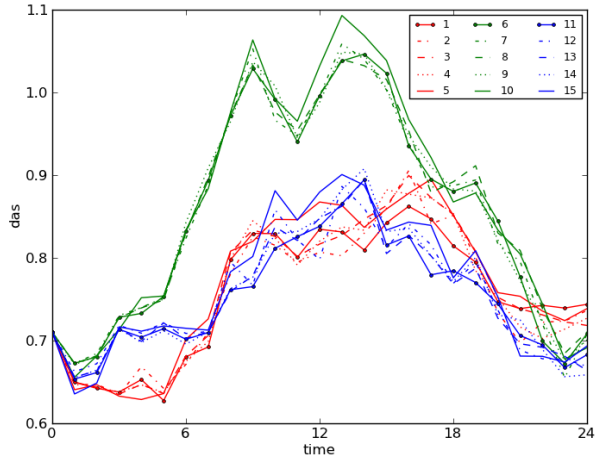


**(c)** DAS

**Figure A5:** Time series of FBI, ETS and DAS for the DE region on 17 July 2009, legend as in Figure 9a.

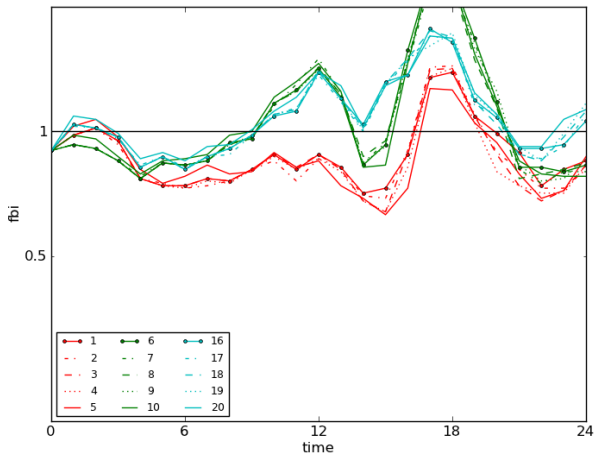


**(a)** FBI

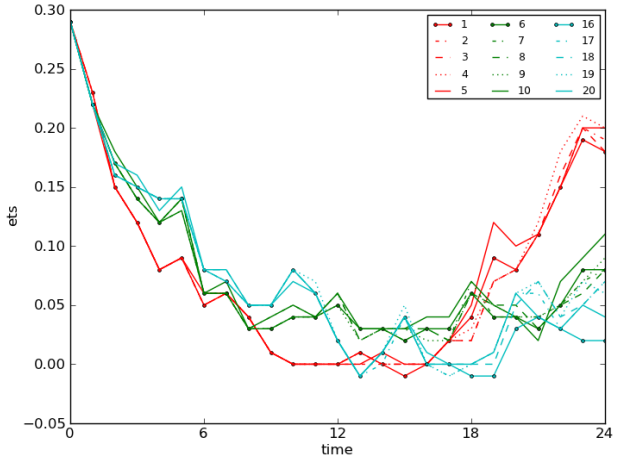


**(b)** ETS

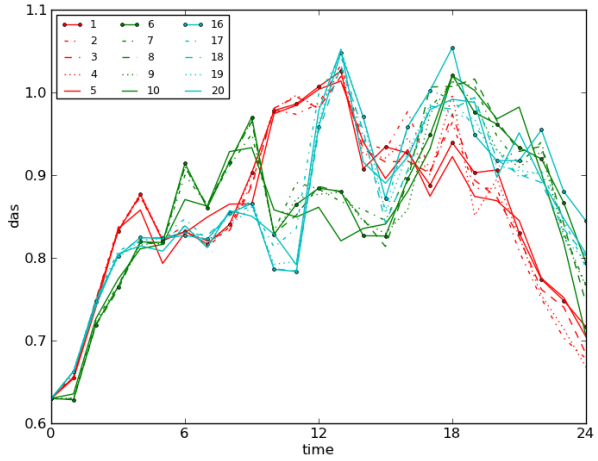


**(c)** DAS

**Figure A6:** Time series of FBI, ETS and DAS for the DE region on 22 July 2009, legend as in Figure 9a.

in

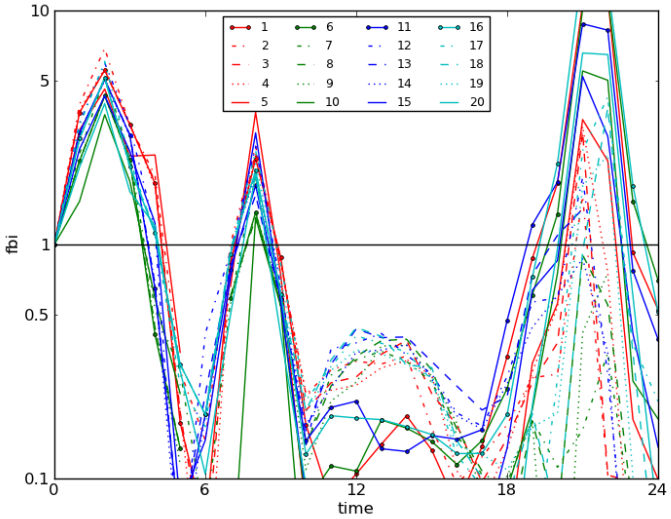


**(a)** 30 June

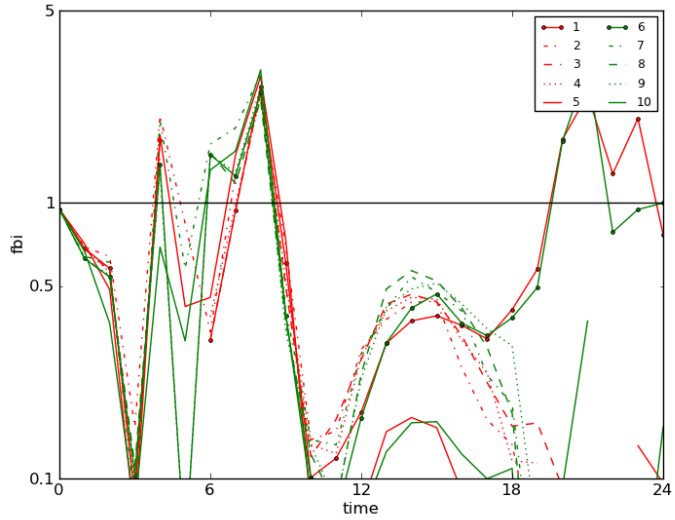


**(b)** 01 July

**Figure A7:** Time series of FBI for the COPS region on 30 June and 01 July 2009, legend as in Figure 9a.

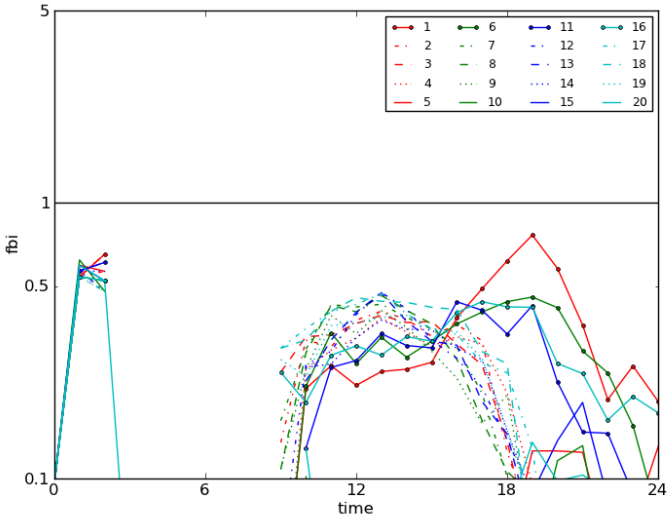


**(a)** 02 July

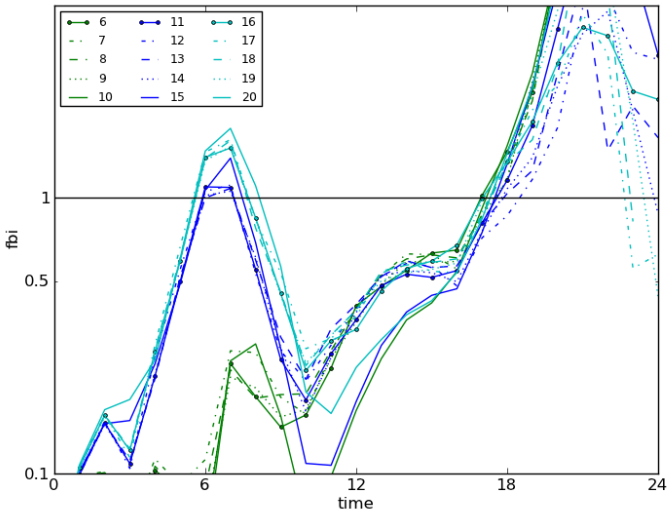


**(b)** 03 July

**Figure A8:** Time series of FBI for the COPS region on 02 and 03 July 2009, legend as in Figure 9a.

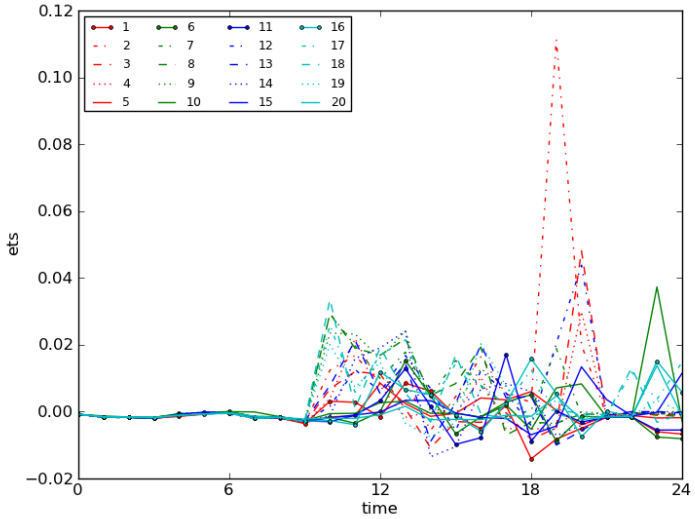


**(a)** 30 June

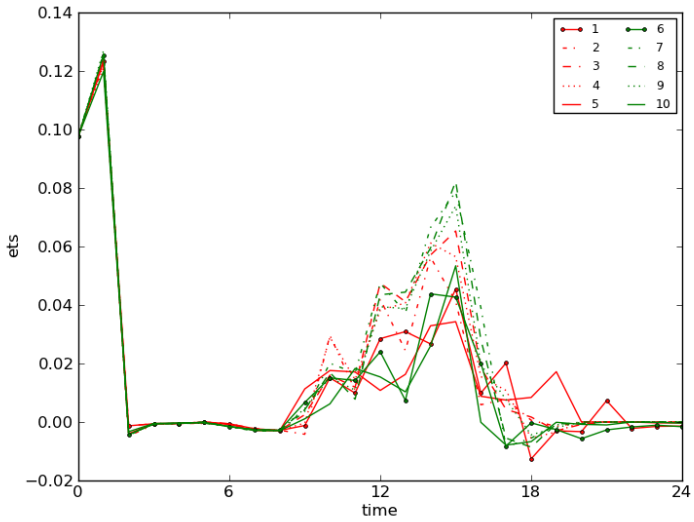


**(b)** 01 July

**Figure A9:** Time series of ETS for the COPS region on 30 June and 01 July 2009, legend as in Figure 9a.

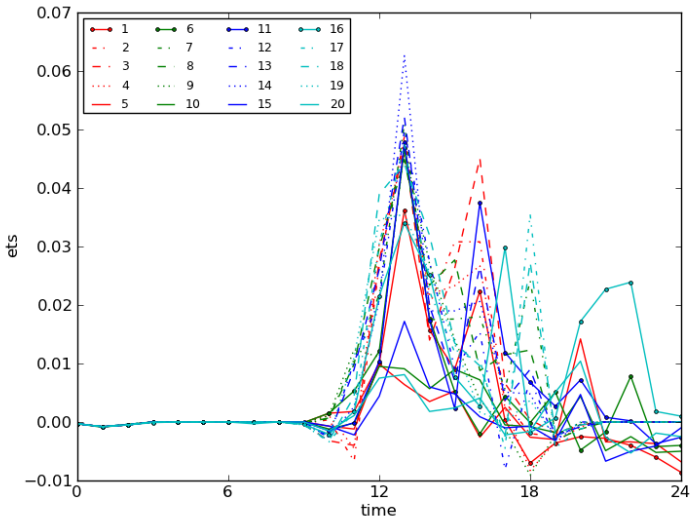


**(a)** 02 July

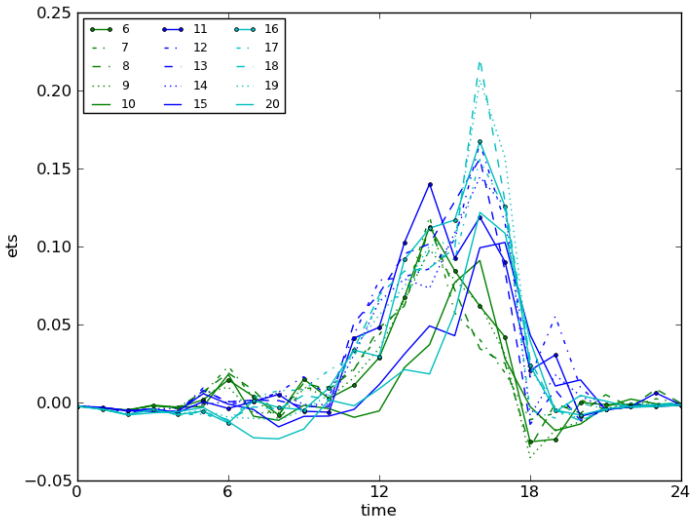


**(b)** 03 July

**Figure A10:** Time series of ETS for the COPS region on 02 and 03 July 2009, legend as in Figure 9a.

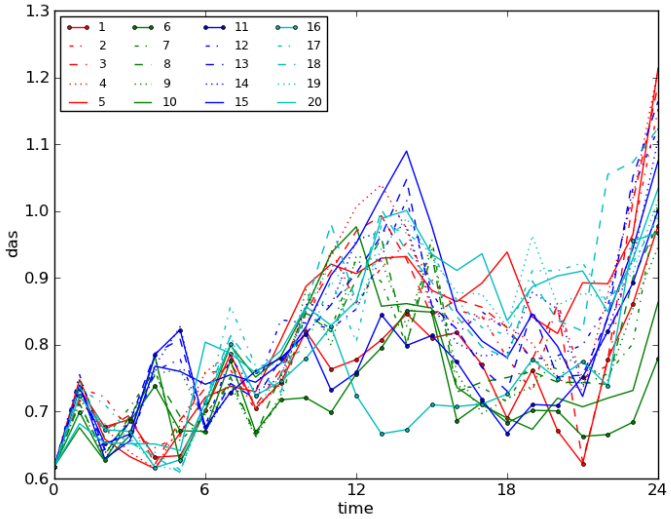


**(a)** 07 July

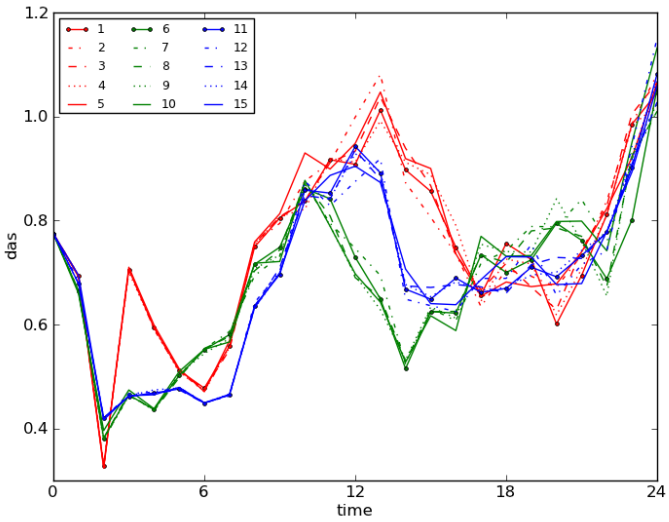


**(b)** 12 July

**Figure A11:** Time series of DAS for the COPS region on 07 and 12 July 2009, legend as in Figure 9a.

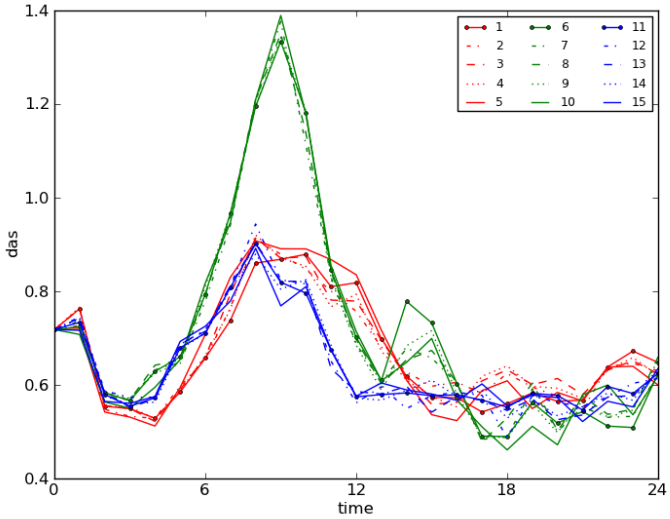


**(a)** 17 July

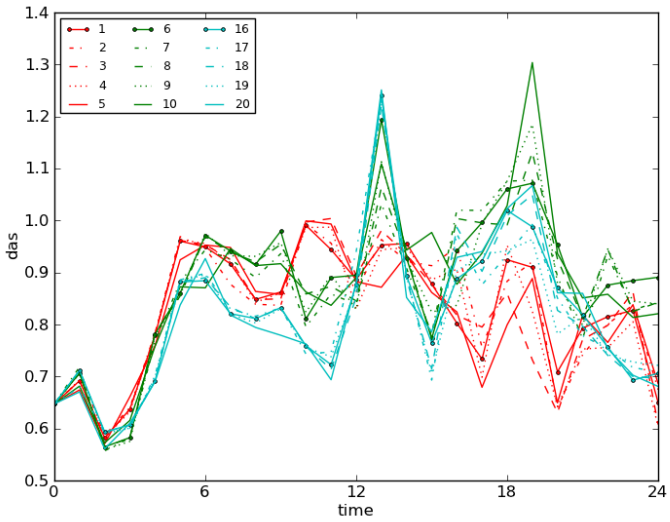


**(b)** 22 July

**Figure A12:** Time series of DAS for the COPS region on 17 and 22 July 2009, legend as in Figure 9a.

# List of Figures

# List of Tables

# Bibliography


[1] A. Arakawa and W.H. Schubert. Interaction of a cumulus cloud ensemble with the large-scale environment, part I. *Journal of the Atmospheric Sciences*, 31:674–701, April 1974.

[2] Aristotle. Meteorologica. `http://ebooks.adelaide.edu.au/a/aristotle/meteorology/`. translated by E.W. Webster, access date: 16 December 2011.

[3] M. Baldauf, J. Förstner, S. Klink, T. Reinhardt, C. Schraff, A. Seifert, and K. Stephan. *Kurze Beschreibung des Lokal-Modells Kürzestfrist COSMO-DE (LMK) und seiner Datenbanken auf dem Datenserver des DWD*. Deutscher Wetterdienst, Offenbach, May 2010.

[4] M. Baldauf, A. Seifert, J. Förstner, D. Majewski, M. Raschendorfer, and T. Reinhardt. Operational convective-scale numerical weather prediction with the COSMO model: Description and sensitivities. *Monthly Weather Review*, 139:3887–3905, December 2011.

[5] E. Binder. *Bauern- und Wetterregeln*. Ulmer, 191pp, 2000.

[6] V. Bjerknes. Das Problem der Wettervorhersage, betrachtet vom Standpunkt der Mechanik und der Physik. *Meteorologische Zeitschrift*, 21:1–7, 1904.

[7] K. Bosch. *Elementare Einführung in die angewandte Statistik*. Vieweg Verlag, 322pp, 8th edition, 2005.

[8] L. Cuo, T.C. Pagano, and Q.J. Wang. A review of quantitative precipitation forecasts and their use in short- to medium-range streamflow forecasting. *Journal of Hydrometeorology*, 12:713–728, October 2011.

[9] S. Dierer, M. Arpagaus, A. Seifert, E. Avgoustoglou, R. Dumitrache, F. Grazzini, P. Mercogliano, M. Milelli, and K. Starosta. Deficiencies in quantitative precipitation forecasts: sensitivity studies using the COSMO model. *Meteorologische Zeitschrift*, 18(6), December 2009.

[10] J.M. Done, G.C. Craig, S.L. Gray, P.A. Clark, and M.E.B. Gray. Mesoscale simulations of organized convection: Importance of convective equilibrium. *Quaterly Journal of the Royal Meteorological Society*, 132:737–756, 2006.

[11] DWD. Weather Charts of western Europe. `http://www.wetter3.de/Archiv/archiv_dwd.html`. access date: 16 December 2011.

[12] E.E. Ebert, U. Damrath, W. Wergen, and M.E. Baldwin. The WGNE assessment of short-term quantitative precipitation forecasts. *Bulletin of the American Meteorological Society*, pages 481–492, April 2003.

[13] K.A. Emanuel. *Atmospheric Convection.* Oxford University Press, New York, 592pp, 1994.

[14] C. Gebhardt, S.E. Theis, M. Paulat, and Z. Ben Bouallègue. Uncertainties in COSMO-DE precipitation forecasts introduced by model perturbations and variation of lateral boundaries. *Atmospheric Research*, 100:168–177, May 2011.

[15] M. Hagen. The EULINOX European radar composite, 2000. 8pp.

[16] M. Hagen. Einführung in die Radarmeteorologie - Manuskript zur Vorlesung, 2010. 100pp.

[17] C. Hohenegger and C. Schär. Atmospheric predictability at synoptic versus cloud-resolving scales. *Bulletin of the American Meteorological Society*, pages 1783–1793, November 2007.

[18] M.S. Jones, B.A. Colle, and J.S. Tongue. Evaluation of a mesoscale short-range ensemble forecast system over the northeast United States. *Weather and Forecasting*, 22:3525–3539, February 2007.

[19] E. Kalnay. *Atmospheric Modelling, Data Assimilation and Predictability.* Cambridge University Press, 341pp, 2003.

[20] C. Keil and G.C. Craig. A displacement-based error measure applied in a regional ensemble forecasting system. *Monthly Weather Review*, 135:3248–3259, September 2007.

[21] C. Keil and G.C. Craig. A displacement and amplitude score employing an optical flow technique. *Weather and Forecasting*, 24:1297–1308, October 2009.

[22] C. Keil and G.C. Craig. Regime-dependent forecast uncertainty of convective precipitation. *Meteorologische Zeitschrift*, 20(2):145–151, April 2011.

[23] F. Kong, K.K. Droegemeier, and N.L. Hickmon. Multiresolution ensemble forecasts of an observed tornadic thunderstorm system. part I: Comparison of coarse- and fine-grid experiments. *Monthly Weather Review*, 134:807–833, March 2006.

[24] D. Leuenberger, M. Stoll, and A. Roches. Description of some convective indices implemented in the COSMO model. Technical Report 17, Consortium for Small-Scale Modelling, 18pp, April 2010.

[25] M Leutbecher and T.N. Palmer. Ensemble forecasting. *Journal of Computational Physics*, 227:3515–3539, 2008.

[26] Lewis. Roots of ensemble forecasting. *Monthly Weather Review*, 133:1865–1885, July 2005.

[27] E. Lorenz. The statistical prediction of solutions of dynamic equations. *Proceedings of the International Symposium on Numerical Weather Prediction, Meteorological Society of Japan*, 1962.

[28] P. Lynch. The origins of computer weather prediction and climate modeling. *Journal of Computational Physics*, 227:3431–3444, 2008.

[29] C. Marsigli, A. Montani, and T. Paccagnella. The COSMO-SREPS ensemble for the short-range: system analysis and verification on the MAP D-PHASE DOP. Presentation at Conference: Challenges in hydrometeorological forecasting in complex terrain, 20pp, 2008.

[30] L. Molini, A. Parodi, N. Rebora, and G.C. Craig. Classifying severe rainfall events over Italy by hydrometeorological and dynamical criteria. *Quaterly Journal of the Royal Meteorological Society*, 137:148–154, January 2011.

[31] F. Molteni, R. Buizza, T.N. Palmer, and T. Petroliagis. The ECMWF ensemble prediction system: Methodology and validation. *Quaterly Journal of the Royal Meteorological Society*, 122:73–119, 1996.

[32] M. Paulat, S.E. Theis, Z. Ben Bouallègue, M. Buchhold, and R. Ohl. COSMO-DE-EPS – construction, diagnoses and verification of a limited-area ensemble prediction system on the convective scale. *EMS Annual Meeting Abstracts*, 6, 2009.

[33] C. Peralta and M. Buchhold. Initial condition perturbations for the COSMO-DE-EPS. *COSMO Newsletter*, 11:115–123, February 2011.

[34] D.J. Stensrud, J.-W. Bao, and T.T. Warner. Using initial conditions and model physics perturbations in short-range ensemble simulations of mesoscale convective systems. *Monthly Weather Review*, 128:2077–2107, July 2000.

[35] K. Stephan, S. Klink, and C. Schraff. Assimilation of radar-derived rain rates into the convective-scale model COSMO-DE at DWD. *Quaterly Journal of the Royal Meteorological Society*, 134:1315–1326, 2008.

[36] Theophrastus. De signis. `http://penelope.uchicago.edu/Thayer/E/Roman/Texts/Theophrastus/De_signis*.html`. access date: 16 December 2011.

[37] T. Weusthoff, D. Leuenberger, C. Keil, and G.C. Craig. Best member selection for convective-scale ensembles. *Meteorologische Zeitschrift*, 20(2), April 2011.

[38] D.S. Wilks. *Statistical Methods in the atmospheric sciences.* Academic Press, New York, 628pp, 2006.

[39] V. Wulfmeyer, A. Behrendt, H.-S. Bauer, C. Kottmeier, U. Corsmeier, A. Blyth, G.C. Craig, U. Schumann, M. Hagen, S. Crewell, P. Di Girolamo, C. Flamant, M. Miller, A. Montani, S. Mobbs, E. Richard, M.W. Rotach, M. Arpagaus, H. Russchenberg, P. Schlüssel, M. König, V. Gärtner, R. Steinacker, M. Dorninger, D.D. Turner, T. Weckwerth, A. Hense, and C. Simmer. The convective and orographically induced precipitation study. *Bulletin of the American Meteorological Society*, 89(10):1477–1486, October 2008.

[40] M. Zimmer, G.C. Craig, C. Keil, and H. Wernli. Classification of precipitation events with a convective response timescale and their forecasting characteristics. *Geophysical Research Letters*, 38(L05802, doi:10.1029/2010GL046199), 2011.

[41] M. Zimmer and H. Wernli. Verification of quantitative precipitation forecasts on short time-scales: A fuzzy approach to handle timing errors with SAL. *Meteorologische Zeitschrift*, 20:95–105, 2011.

# Eidesstattliche Erklärung

Hiermit erkläre ich, die vorliegende Arbeit selbständig verfasst zu haben und keine anderen als die in der Arbeit angegebenen Quellen und Hilfsmittel benutzt zu haben.

München, 22. Dezember 2011